Ragab Elsayed Rabeiy

Spatial Modeling of Heavy Metal Pollution of Forest Soils in a Historical Mining Area Using Geostatistical Methods and Air Dispersion Modeling

TU Clausthal

Spatial Modeling of Heavy Metal Pollution of Forest Soils in a Historical Mining Area Using Geostatistical Methods and Air Dispersion Modeling

Dissertation

Zur Erlangung des Doktorgrades
der Ingenieurwissenschaften
(Dr.-Ing.)

vorgelegt von
M. Sc. Ragab Elsayed Rabeiy
aus Sohag/Ägypten

genehmigt von der
Fakultät für Energie-und Wirtschaftswissenschaften

an der
Technischen Universität Clausthal

Tag der mündlichen Prüfung
05.10.2010

Vorsitzender der Promotionskommission:	**Univ.-Prof. Dr.-Ing. N. Meyer**
Hauptberichterstatter:	**Univ.-Prof. Dr.-Ing. Wolfgang Busch**
Berichterstatter:	**Dr. Walter Schmotz**

TU Clausthal

Spatial Modeling of Heavy Metal Pollution of Forest Soils in a Historical Mining Area Using Geostatistical Methods and Air Dispersion Modeling

Doctoral Thesis
(Dissertation)

To be awarded the degree
Doctor of Engineering
(Dr.-Ing.)

Submitted by
M. Sc. Ragab Elsayed Rabeiy
From Sohag/Egypt

Approved by
Faculty of Energy and Management Science

at
Clausthal University of Technology
Germany

Date of Oral Examination
05.10.2010

Abstract

Mining and smelting activities have an extreme effect on the environment. They affect soil, air, materials, and people that exist neighbored them. Goslar county in Lower-Saxony, Germany, was one of the most important mining and metal production areas in the world. The long time of mining, mineral processing, and smelting activities in the area have enriched the forest soil with many heavy metals. Spatial distributions of Lead, Zinc, Mercury, Arsenic, Cadmium, Antimony and Copper were investigated in forest soils using geostatistical methods integrated in a Geographic Information System (GIS). Geostatistical methods were used to explore the raw data, get distribution closer to normality, and calculate the experimental semivariograms and their fitted models. Ordinary Kriging was applied to predict the spatial distribution of soil heavy metal concentrations at unsampled locations. A GIS based model was developed to improve the accuracy of the predicted values. The model selects new sites of soil samples based on the estimated maximum values of Standard Prediction Errors (SPE). The distribution maps of the mentioned heavy metals in the forest soils were generated by geostatistical methods after taking the new soil samples. These predicted concentrations are generated for the whole Goslar county area and named as Global prediction maps. A comparison of the predicted values before with after taking the new soil samples was made. Because of the local activities of mining and smelting in some sites, soils around these locations are intensively contaminated by heavy metals. Investigation of these locations was done to determine their specific geostatistical properties. The predicted values of small areas based on these specific geostatistical parameters were merged into the Global prediction map of the same soil heavy metal.

Soil pollution by heavy metals was caused by many sources. The most effective source in Goslar county was smelter chimneys. The pollutants emitted from the smelters had dispersed in the air and had travelled along wind directions to several hundreds of meters or kilometers from the sources. Therefore a *Dispersion Plume Model* was generated to estimate the emission rate of pollutants into the atmosphere from a single point source. The approach is based on the Gaussian plume type solution for the advection–diffusion equation. The model was applied to estimate the amount of particulate matters emitted from the historical Clausthal-Zellerfeld smelter. Atmospheric stability, mixing height and deposition velocity are essential parameters in modeling the transporting of pollutants. These parameters in addition to the emission source parameters are used as feeding data into the Dispersion Plume Model. Therefore another model was developed *(Auxiliary Meteorological Model*) to compute these meteorological variables. The model was designed to estimate hourly meteorological variables from routinely measured

weather data from 2004 to 2009 in Clausthal-Zellerfeld. The Auxiliary Meteorological Model determines Pasquill–Gifford atmospheric stability categories based on surface observations of wind speed, incoming solar radiation and daytime. According to each atmospheric stability, the model estimates friction velocity, Monin–Obukhov length, convective velocity, mixing height, and deposition velocity. The hourly pattern of stability classification was obtained and the results showed that the atmosphere in summer is about 25%, 26%, 49%, at unstable, neutral, and stable conditions respectively. While it is 2% unstable, 41% neutral, and 57% stable in the winter. The temporal variation of mixing height was modeled and its relationship with the atmospheric stability, incoming solar radiation, and wind speed was analyzed. The results indicated that the estimated mixing heights in summer and spring are greater than that of winter and fall during day-hours. While during night-hours, heights of the mixing layer for winter and fall are greater. The Dispersion Plume Model computes Lead concentrations at several selected locations around Clausthal-Zellerfeld smelter. The results of air dispersion modeling indicated that extreme values for forest soil contamination in the surroundings of Clausthal-Zellerfeld are caused by the smelter. The modeled Lead pollution was compared with the measured values from soil samples at the same sites. The results of the comparison showed that the modeled Lead concentrations from the smelter are smaller than Lead values of today soil samples.

Keywords: Soil Pollution; Soil Heavy Metals; Mining and Smelting Impacts; Geostatistical Methods; Air Dispersion Modeling; Atmospheric stability; Mixing Height; Dry Deposition

Acknowledgment

This work has been carried out at the Institute of Geotechnical Engineering and Mine Surveying (IGMC) at Clausthal University of Technology, Germany, under supervision of *Professor Dr.-Ing. Wolfgang Busch*. First of all, I would like to express my deep gratitude to my supervisor *Prof. Dr.-Ing. Wolfgang Busch* for giving me an opportunity to implement this work under his supervision. I am very grateful for his unlimited support, and his invaluable guidance.

I would like to thank Goslar district authority. They provide this work with the data of soil heavy metals, inclusively taking and analyzing the new soil samples. Sincere thanks I give to my co-supervisor *Dr. Walter Schmotz*, department of Building & Environment, Goslar county for sharing his knowledge, his ideas and his support.

I am sincerely grateful to my beloved country Egypt for awarding me the scholarship and supporting of all necessities to implement this study.

I am greatly appreciating the effort of *Professor Dr.-Ing. Klaus Maas*, (University of Applied Science Ostwestfalen-Lippe, Department of Environmental Information) for his support in the project start-up as he was a member of IGMC. I thank him also for his participation in the selection of some new soil sample sites based on GIS techniques.

I would like to express my appreciation to my colleagues and all the members in IGMC for their helpful and family atmosphere. Also I would like to give particular thanks to *Dr. rer. nat. Steffen Knospe* (IGMC), I am grateful for his advices and his help on the geostatistical methods.

I gratefully acknowledge the Institute of Electrical Information Technology, Clausthal University of Technology and thank *Mr. Joachim Wittwer* for supplying this work with the measured weather data from 2004 to 2009.

I am deeply indebted to my wife, for her spiritual support, her encouragement and her patience. Special thanks to my Children, *Kareem* and *Hamada*, who lost much happiness because of this study and I have received motivation and positive energy from them. My deepest thanks to my mother and my mother in law for all their prayers, care and love. Once more, I would like to express my gratitude to my brother in law *Dr.-med. Tallat Abo-Elwafa* for taking care of my mother in Egypt and all my matters there.

Ragab Rabeiy

October, 2010

Clausthal-Zellerfeld/Germany

Table of Contents

Chapter (1) Introduction and Objectives

1.1Mining and Smelting Impacts on Soil

Mining and smelting activities have usually impacts on the environment (Gäbler & Schneider, 2000). Soil pollution at and near the historical mining and smelting sites may present immediate danger to people and animals that are living in the neighborhood of them, and they threaten the proper functioning of soil (Steiger et al., 1996). Soil heavy metals are an important group of anthropogenic contamination sources (Einax & Soldt, 1995). Soil pollutions by heavy metals are serious problem and understanding the spatial distribution of pollutants and levels of contamination is critical for understanding environment and decision-making (Liu et al., 2006). Studying the affected areas will help to understand the size of the contaminated locations, level of soil heavy metals and their spatial distribution. Such data assists in evaluating the risk of soil heavy metals on the environment and human health (McGrath et al., 2004). Heavy metals are chemical elements with a specific gravity greater than 5 g/cm^3 (Duffus, 2002). Some well-known toxic heavy metals with a specific gravity that is more than 5 g/cm^3 are As, 5.7 g/cm^3; Cd, 8.65 g/cm^3; Zn, 7.13 g/cm^3; Pb, 11.36 g/cm^3; Hg, 13.55 g/cm^3; and Sb, 6.66 g/cm^3 (Lide, 1992). Small amounts of heavy metals are exist in the environment and our food and they are actually necessary for our health, but large amounts of these metals cause acute or chronic poisoning (www.lef.org/). Heavy metal toxicity can damage or reduce mental and central nervous function, lower energy levels, and damage to blood composition, lungs, kidneys, liver, and other vital organs. The main risk of heavy metals to human health is the exposure of Pb, Cd, Hg, and As (Järup, 2003).

1.1.1 History of Mining on the Study Area

This study was applied on Goslar county which located on Lower Saxony, Germany as presented in Figure (1-1). The study area is located on the northwestern slopes of the Upper Harz Mountains. Harz Mountains are the northernmost low mountain range in Germany having strong gradients of topography at the northern edge of the mountains and a mean altitude of 700 m (Schulze et al., 1994). Goslar county has an area of 965 km^2 and the number of population is 145,000 (on June, 2009). Goslar city (the administrative centre of the county) and the Rammelsberg Mine are UNESCO World Heritage Sites (www.landkreis-goslar.de). Mining and mineral processing activities in Goslar county have been carried out for centuries (Gäbler, 1997). Mining operations are believed to have started in the Harz Mountains during the Bronze Age (Matschullat et al., 1997). Smelting and mining from the 3rd to the 10th century were observed at several places. At that time, mining processes were carried out using simple

technologies and pits were dug into the ground to a maximum depth of about 40 m (Monna et al., 2000). Mining researchers indicated that, at least since 3rd century, Rammelsberg and Upper Harz ores were transported to long distances and smelted the minerals on the border of the Harz. Until the usage of fossil fuel in the 19th century, wood was the only heat supply (Kaufhold, 1992). During Bronze Age, mining and smelting activities in the Harz Mountains demanded a lot of wood and brought about the first disturbance of the area forest, which was intensified during the middle Ages with the modernization of mining, especially at the Rammelsberg sites (Schroeder & Reuss, 1883). Roasting sulfidic ores had demanded 1.3 t wood per ton Pb and Cu ore, smelting of the ores required a further 0.7 t wood. It was cheaper to transport the ores to wood sites than vice versa (Ernst et al., 2004). Before the Middle Age, mining activities were limited to smaller-opencast mining in concentrated deposits with easy entries. The preparation was made by hand and the smelting was on opened stoves near the deposit sites. The highlight of the Middle Age industry and mining was the 12th/13th century, whereat it was estimated that the metal demand per household (without silver and iron) increased 20-100 times from the 12th till the 14th century (Kaufhold, 1992).

With the deployment of waterpower on middle Ages (12th/13th century) and the switch to heavy engineering, a new period for the technical and environmental history begun. The increased demand to the wood and the damages which made by smelter emissions and heavy metal dusts led to an extended degradation of the forest vegetation in many regions. Since the change in 15th/16th century the technical development led to deep changes in the area of using waterpower and to a general rising of the European mining. Many of the mines that were closed during the recession were operated again and new deposits were explored. The extreme activities of mining and smelting happened about 1650 by using explosives (Kaufhold, 1992). The polymetallic sulphide deposit of Rammelsberg was the basis of mining activity for nearly 1000 y before finally closing in 1988 (Large & Walcher, 1999). In view of its long history of mining, as well as the variability of the metal concentrations within the ore, the combined tonnage and grade of the Rammelsberg ore bodies can be estimated at 27-30 Mt with an average grade of 14% Zn, 6% Pb, 2% Cu, 1 g/t Au, 140 g/t Ag and 20% barite. During the final years of mining, the daily production capacity was 1200 t ore grading at 12% Zn, 6% Pb, 1% Cu, <1 g/t Au, 150 g/t Ag and 20% barite (Muchez & Stassen 2006).

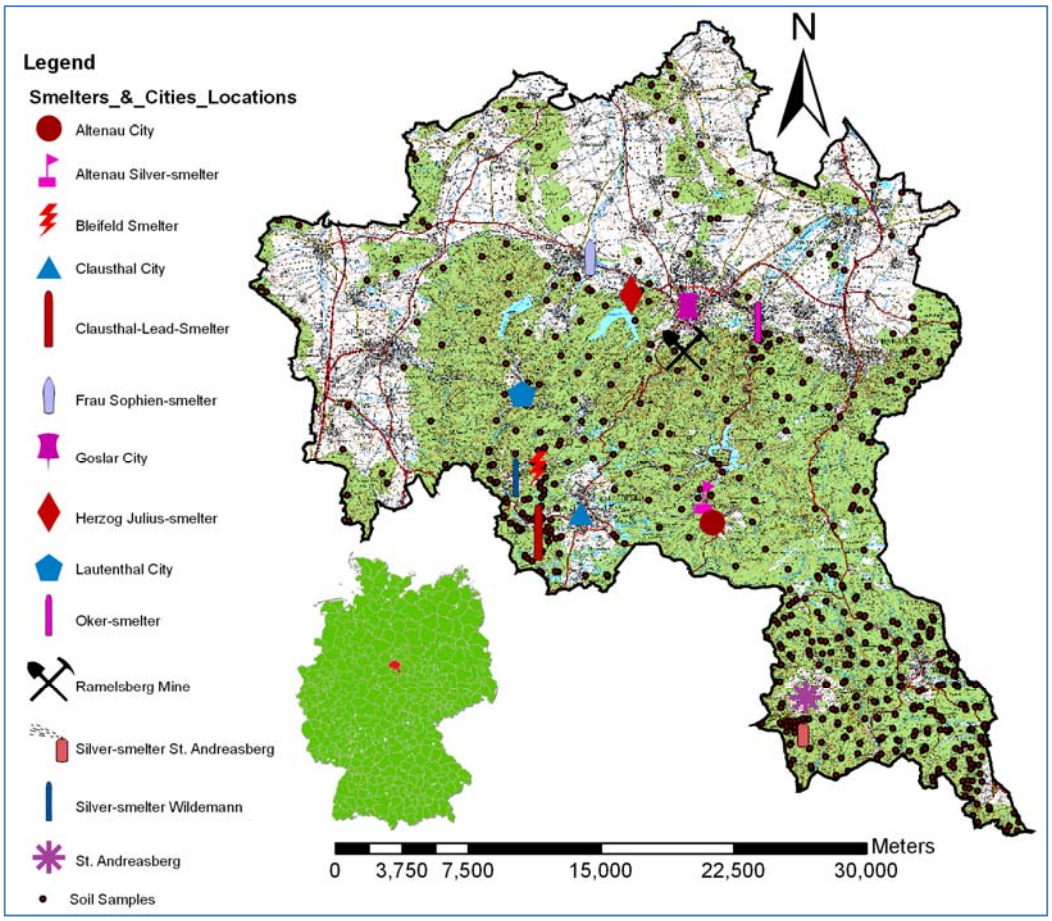

Figure (1-1) Location of the study area

The mineral ore veins of St. Andreasberg was containing the economically important Pb, Zn and Cu sulphide ores as well as native As, Sb and Ag. The Samson silver mine in St. Andreasberg was operated from 1521 to 1910. The deepest level of the mine is 810 m below surface. On this site, silver was found in very high concentrations, sometimes even solid. Accompanying ores contained among others high concentrations of arsenic minerals (Mertz et al., 1989). Remarkable technology features of the mining operations were the generations of the huge waterwheels (12 m diameter), which powered transport of ores and men, pumping of water and processing of ores. The Harz region is also the birthplace of the wire-rope. In the Samson mine is the last original and fully functional "Fahrkunst" of the world. It is wire rope elevator was installed in 1837 and allowed the miners to drive down into the mine within 45 minutes, which was twice as fast as before (Ernst et al., 2004).

1.1.2 Soil Contamination within the Study Area

As a consequence of mining and smelting processes, increasing the soil pollution by heavy metals is the logic effect of these long activities in the area of Goslar County. The direct and indirect harm, which was done by smelters is not

limited to forests, it also affected farmland, meadows, gardens, animals and humans (Schroeder & Reuss, 1883). Four different types of man-made have enriched soils with heavy metals, can be summarized as follow: (a) transporting the minerals from mining sites to smelter locations; (b) Slags and other remnants and smelting process were heaped up as slag tailings near the smelters at numerous sites in the Harz Mountains; (c) Up to the 19th century, the metal separated by washing. Due to this procedure, rivers received metal-contaminated sediments which were transported to the lowland and were deposited on river banks; (d) Metal smelters and refineries were constructed at many locations within the Goslar County (e.g. at Clausthal-Zellerfeld, Wildemann, St. Andreasberg, Oker, Altenau, and Lautenthal among others) Figure (2-1). Due to the lack of filters, metals and air pollutants were emitted and affected soil in the forest areas up to several km distances (Ernst et al., 2004). The normal values of the heavy metals that are available in soils in Lower Saxony are 20-40 mg/kg (Pb), 50-70 mg/kg (Zn), 1.0-15 mg/kg (As), 0.2-0.4 mg/kg (Cd), 10-20 mg/kg (Cu), and around 0.1 mg/kg (Hg). Some researchers studied the soil heavy metals in the area and found contaminated sites in the district of Goslar County as follow: 338 in Goslar city, 115 in Bad-Harzburg, 44 in Braunlage, 117 in Langelsheim, 102 in Seesen, 40 in St. Andreasberg and 156 sites in Upper Harz (Hennighausen & Höfert, 2005). Gäbler and Schneider (2000) studied the floodplain soils of the Harz Mountains and the area around the northwest of the region. They investigated the soils to characterise the heavy-metal contamination over large areas and to evaluate the hazard to the environment due to heavy metal mobility. A 12.5 km^2 study area was assessed with respect to its heavy metal load. They found that, the heavy metal loads of the soils in the study area have ranges of < 0.2-200 mg/kg for Cd, < 10-30,000 mg/kg for Pb, 7-10,000 mg/kg for Cu and 50-55,000 mg/kg for Zn.

1.1.3 Soil Samples and Analysis

Soil samples were collected at different locations within Goslar County. The samples were taken from the sites without specific grid. Most of soil samples are gathered from the top surface (0-30 cm) to differentiate between natural and anthropogenic sources of pollutants. Normally, industrial pollutants contaminate the upper layer of the soil. In case of natural pollutants, the entire soil shows high metal enrichment at all depths. At each sample location, nine sample places were selected at a circle of 10 m diameter. Eight samples were taken at the periphery of the circle with 450 degree and the last one is taken at the circle center. The final value of the soil sample at a particular location is the average of these nine samples. Three soil layers were sampled at each location; these are Organic-Layer, Top-Layer and Sub-Layer. The top layer is the most important layer for plants and building activities, therefore the Top-Layer is considered only in this study. Some

locations have no Organic-layer and the Top-layer begins from zero depth. Analysis of soil samples were made by three different methods, Aqua Regia (mixture of HCl, HNO_3 and $H2O_2$); Nitric acid, also known as Aqua Fortis (HNO_3) and HF (Hydrofluoric acid) (Jonušaitė et al., 2004; Sabienė et al., 2007). The samples were gathered by different organizations at different time and analysis by various methods. Therefore many locations have more than one value for the same soil heavy metal. Calculations in this study were developed for the average value in these locations. Some implausible values for As at sites St. Andreasberg city are excluded after careful analysis. The study concerned with the transportation of pollutants by wind, therefore soil samples located within the floodplains of the rivers are excluded.

1.2 Smelters in the Study Area

In Goslar County there were seven main smelters, from which four located in Harz and called Upper Harz smelters and three were on the north border of the Harz and called Under Harz smelters, as shown in Figure (1-1). These smelters were constructed in the following years: Clausthal-Zellerfeld smelter in 1554, Altenau smelters in 1615, Lautenthal-smelter in 1638, Andreasberg smelter in 1521, Julius-smelter in 1561, Sophien smelter in 1564, and Oker smelter in 1580 (Schroeder & Reuss, 1883). Clausthal-Zellerfeld smelter was the most important smelter, relating to smoke damage in the forest; Altenau was in second most important one and Lautenthal the last one. From the Under Harz smelters, Julius-smelter was the most important; Oker came second place and Sophien smelter wasn't really taken into account at all. Most of these smelters were closed before 1950 except Clausthal-Zellerfeld smelter closed in 1967 and Oker smelter which was closed in 1970 (Kaufhold, 1992; Hanusch, 2005). Because these smelters are very old, information about dust emissions are rare to be found. The air dispersion model is applied on Pb particulate matters emitted from Clausthal-Zellerfeld smelter because it is considered as the most important and its data is available too. In 1958 Peucker presented a report as his diploma thesis from Technical University of Hanover. His report studied the negative effect of Clausthal-Zellerfeld smelter on the environment. The following details of Clausthal-Zellerfeld Pb smelter is extracted from his study.

1.2.1 Technical Procedures of Clausthal-Zellerfeld Smelter

The ores were given from the mines to the preparation facilities. In early times the ores were separated and crushed to fine size. The crushed product called "Schliech" was the input into Clausthal-Zellerfeld smelter. Until 1767 the Pb-shine Schliech was roasted in flame furnaces, which means that the Pb sulfide was

overtaken in oxidic form and melted in curved furnaces. In this process, a lot of wood and coal was used for roasting and melting and there was also a remarkable Pb, and Ag loss. After that metallic Pb and sulfur iron was produced through melting Pb-shine and iron together, according to the reaction PbS + Fe = Pb + FeS. This chemical process isn't done completely. The products were: (1) Werkblei (Work-Pb), which has to be processed on silver and Weichblei (Soft-Pb), (2) Pb stone, consisted of sulfur Fe and sulfur Pb and got the whole copper of the Schliech, and (3) Schliech-slag or Ore-slag, which was added to the melting process, partially there were slag stones separated and the rest were dropped on the pile.

In 1850 there were five 6 to 7 meters high furnaces in Clausthal-Zellerfeld smelter. They were supported by dust chambers, in which hard contaminations of the smoke settled down. The condensation of the dust was very poor. The Pb contents of the Pb stone fluctuated between 40 to 70%, the major portion of the sulfur was here, and just a little part was sent into the air through the melting of Schliech. Before continuing the process of the Pb stone, it was necessary to decrease the sulfur content, which was accomplished by roasting in bunches in the free atmosphere or in roasting sheds. In the roasting process the Pb stone was put as layers and set on fire. The burned sulfur was releases into the air as SO_2. In the stone melting process more sulfur got into air. So nearly the whole sulfur content of the Schliech in the smelter process got into air. With the initiation of the roast reduction process, it wasn't possible at first to use the roast gases containing small amount of SO_2 for the sulfuric acid production. Earlier the oxidation of the sulfide ores, the roasting, in which the main mass of the SO_2 emission is produced, was done in roast furnaces. The emission contained maximum 4% sulfur dioxide, which was emitted completely into the air (over the new chimney). Since 1920 roasting is done in Clausthal-Zellerfeld only on sinter machines. In the first process the rich gases with SO_2 content of 2-2.5 Vol. % are produced, which could be processed in the 1923 built sulfuric acid facility. With the roasting process, the SO_2 content of the gases decreases rapidly, and the produced gases (with less SO_2) are useless for the sulfuric acid fabrication. From 1950, Clausthal-Zellerfeld smelter processed around 2500 t of Pb ores in a month. The ores were crushed to fine size and mixed with additions which are necessary to melt the Pb at special temperatures. The ore and the additions get into a round sinter machine, on which the roasting is done. The sulfide ore is oxidized after pressure-sintering. Under these circumstances the SO_2 concentrations were higher and could be used for the sulfuric acid production. Emissions (i.e. contaminations) were getting through a new filter device, where the hard matter is hold down. The sintered production had Pb content around 50% and sulfur content around 1%. This sintered melted with some additions in the shaft furnace. The emissions of the shaft furnace were cleaned from hard matters in an electric filter device. The collected dusts from shaft furnace and from roast gases

were used in the smelter process. The smelter was 10 months operated on average each year. A long operation pause (some weeks), was mostly in July, for the maintenance of the sinter device and the shaft furnace and also for deploying innovations.

1.2.2 Sources and Amount of Emission from Clausthal-Zellerfeld Smelter

There is no detail available about the amounts of emission and contents of contaminations, just some representative measurements and calculations of the sulfur emission in which the monthly processed ore amount is given. In the emission in form of gas, which is important to the vegetation damage, only SO_2 is remarked. It overweighs all other smelter gases so strong that they are not taken into account in the analysis. Chlorine gases can't be recognized, Fluorite traces can be found in some special ores, but they are not considered because of its small amount. The smelter processed 2500 t of ores in a month, with a sulfur content of 15% in the Pb-shine, which means 375 t of sulfur, from which a little part (ca. 25 t-30 t) gone into slag and the rest emitted as SO_2 into the air. In the dust, Pb is the main part. Arsenic was never found in analysis. Otherwise everything that is found in ores may be also found in the dust. As emission sources from Clausthal-Zellerfeld Pb smelter, there are only two places considered. They are the roasting device and the shaft furnace.

At the roast furnace there were 650000 m³ per day = 27000 m³ per hour with a SO_2 content about 4%. The dust portion is large. The roast furnace gases were filtered comprehensively from dust, through the new filters (after 1950). The dust concentration behind the device was 0.005 g/m³. The Pb content in this concentration was 50-70%, so that total dust outburst was 3.2 kg per day, 1.6-2.2 kg Pb can't be stopped by the filter. The temperature of the roast gases behind the filter was decreased to 72°C. At the shaft furnace there were 700,000 m³ of emissions per day = 29200 m³/h. The SO_2 content was low here, but the dust share was extremely high. The values of dust here aren't available. The electric filter worked remarkably worse than the other tube filter. The remains was 0.02 g/m³ of hard contaminations after going through the electric filter device in the emission which was 14 kg of dust with 7- 9 kg of Pb per day. The temperature of the shaft furnace gases was 45 °C after the gas cleaning. Shaft furnace gases and roast furnace gases got together into the smoke channel, which straightens itself up the mountain. There is a total of 1.35 Mm³ per day or 56200 m³ per hour of emissions. The SO_2 concentration is 0.7% here. At the chimney way the same amount of air is added through the holes in the channel wall. The SO_2 concentration decreases to about 0.35%. Finally the dissipater shall do a two-three times extenuation at the chimney head. So the emissions still have a concentration about 0.15% of SO_2, when leaving the chimney to the air. The dust content of the emission decreases to

three times, so that finally 11.5 kg of dust with 5-7 kg of Pb per day get into air. The temperature of the emissions is at the chimney head about 32 °C. Before the dissipater and the device of the fake air holes were taken into operation, according to the concession limit data, the SO_2 emissions were double that much; which means 11.4 g of SO_2 per m³. The chimney of Clausthal-Zellerfeld Pb smelter was nearly 50 m over the smelter complex, on the smelter mountain. To decrease the harm of the smoke in the atmosphere, the chimney was made 20 m higher, from which the upper 15 m was constructed as the dissipater; although it is hard to tell if this extension had decreased the pollution. From the information mentioned in this section the emission proprieties of Clausthal-Zellerfeld smelter required to the air dispersion model can be summarized as presented in Table (1-1).

Table (1-1) Clausthal-Zellerfeld smelter parameters and data feeding to the air dispersion model

Parameters	Values and units
Q (amount of emissions)	= 6 kg/d =250 g/h (of Pb particles)
d_s (Chimney inside diameter)	= 2 m (Hoppe, 1883)
T_s(Exit Temperature)	= 32 0C =305 ^{0}K
v_s (Exit velocity)	Total of emissions $Q_t = 1.35 * 2$ Mm^3/d = 31.25 m^3/s The cross section area of chimney $(A) = \frac{\pi D^2}{4} = 3.14\ m^2$ $Vs = \frac{Q_t}{A} = 9.95\ m/s$
Chimney(stack) Height	$h_s = 70\ m$
Density of Pb	11.36 g/cm^3=11360 kg/m^3 (Lide, 1992)

1.3 Assumptions for Necessary Conditions

Clausthal-Zellerfeld smelter had been working for a long time with different technical procedures. The smelter was active from 1554 to 1967 (Schroeder & Reuss, 1883; Kaufhold, 1992). There is no accurate data about the dust emissions from the smelter before 1920 (Peucker, 1958). During early years the smelter had no filters; therefore the expected emission was huge before 1920. Perhaps the stack height was not more than 10 m above the surface ground. The processing and roasting in the smelter plant were separated, which means that several contamination sources had existed in the same place. The measured meteorological data are from 2004 to 2009. The available meteorological measurements by the weather station are wind speed, wind direction, temperature, pressure, relative humidity, precipitation and incoming solar radiation. Cloud cover information is not available during this period. The estimated distance between a source and a receptor is a function of time. As the time changes, the wind direction also changes which affects the calculated downwind distances. The wind speed also is varying with time which influences the estimated value of pollutants at the

receptor. Wind speed and its direction perhaps change every minute. According to the discussion in this section, spatial distribution of soil contamination was studied based on some assumptions as follow:

- The amount of emissions from Clausthal-Zellerfeld smelter is fixed along the period of smelter working-time, as given in Table (1-1).
- The properties of smelter stack are also not changed during the modeled times (stack height, and stack diameter) as indicated in Table (1-1).
- The measured weather data at a specific hour is the same every year along the modeled period of times.
- The generated Gaussian plume model assumes the averaging time to be one hour, during any modeled hour wind speed and wind direction are constant.
- All the deposited contaminations on the forest soils had been caused by atmospheric dispersion of pollutants that emitted from smelter chimneys.
- Deposition of particles from the atmosphere to the ground surface is considered only by dry deposition, wet deposition by rain and snow are not modeled in this study.
- The amount of contaminations of 3 m height on the atmosphere had settled down vertically into the corresponding area of the forest soil.
- The deposited Pb particulate matters had penetrated the soil to a maximum 20 cm depth and all the settled values had been collected within only the top layer of the soils.
- The deposited heavy metals had mixed homogenously in the soil.
- The density of the soil is constant in the investigated area.
- The heavy metals deposited in the soil are not transported to another place by water or wind erosion and not changed by chemical reactions.

1.4 Objectives of the study

This study is focused on the effect of old Mining and Smelting activities on the soil pollution by heavy metals. The study investigate forest soil pollution by heavy metals within Goslar County which is located within the Harz region, middle Germany. The study area has a long history of mining and smelting activities (Gäbler & Schneider, 2000). Soil heavy metals that are concerned in this study are Lead, Zinc, Mercury, Arsenic, Cadmium, Antimony, and Copper. The study includes two parts which have a reasonable relation between them. The first part is studying the spatial distribution of soil heavy metals using geostatistical methods based on measured soil samples in some locations. The second is using the air dispersion modeling to simulate the transportation of particulate matters from smelter chimneys. This work was completed in cooperation between Institute of

Geotechnical Engineering and Mine Surveying at Clausthal University of Technology and the Department of Building & Environment of the Goslar county administration. In this study, the spatial distributions of soil pollutants are analyzed using geostatistical methods. The objectives of this study part were (1) to select new sites for soil samples to improve the accuracy of the predicted values at unsampled locations; (2) to analyze the spatial dependency to explain variation mechanism of soil heavy metals; (3) to predict the spatial distribution of each studied metal to create its contamination maps, (4) to investigate the locations which are intensively contaminated with heavy metals, and (5) to examine the effect of 2D and 3D dimensions between sample sites on the predicted values.

The main sources of these pollutants on forest soils are the smelters which had emitted solid particles from their chimneys to long distances for long periods of time. In the second part of this study a Gaussian dispersion model is generated using Matlab software. The aims of this study part were (1) to generate an Auxiliary Meteorological Model to estimate the parameters of boundary layers such as friction velocity, convective velocity, mixing height and deposition velocity, (2) to examine a new approach to determine the amount of insolation strength using the measured incoming solar radiation during day-hours, (3) to determine Pasquill–Gifford atmospheric stability categories using observations of wind speed, the suggested range of incoming solar radiation and day time, (4) to develop a Dispersion Plume Model based on a Gaussian plume approach, (5) to examine the amount of plume rise emitted from smelter stack at different meteorological conditions, (6) to estimate the concentration of Pb particles emitted from smelter chimneys on the soil, and to (7) compare the results of geostatistical analysis with that of dispersion modeling. The generated model is able to compute the concentration of gases or particles emitted from a point source. Also, the model can estimate the concentrations above surfaces of different roughness (rural or urban).

1.5 Chapters Description

Chapter (1) gives an introduction about the study, definition of soil heavy metals, mining and smelting impacts, Geostatistics, Kriging, Geographical Information Systems (GIS), Air dispersion modeling and presents the objectives of this work. Chapter (2) describes the theory behind the geostatistical methods. It explains in detail the principles of geostatistical and kriging methods. Also the chapter makes a description of the study area, the history of mining and smelting activities on it and the measured samples of soil heavy metals. Finally the chapter explains the geostatistical analyst tool extension in ESRI's ArcGIS software which is used in this study. Chapter (3) presents the theory of air dispersion modeling. It explains the Gaussian dispersion model and its parameters, plume rise, calculations

of mixing height and dry deposition. Chapter (4) discusses the results of geostatistical analysis of soil heavy metals. It presents some statistical information of the soil samples, the predicted surfaces of spatial distribution of each heavy metal and how we can select new soil samples to improve the predicted values. Also the chapter gives in detail the investigation of the heavily contaminated areas with soil heavy metals. Chapter (5) gives the results of the air dispersion model that is generated in this study using Matlab software. It gives the results of hourly atmospheric stability and mixing height. It, also discusses the relation between mixing height, plume rise and pollutant concentrations under different meteorological conditions. The chapter finally presents the estimated concentration of Pb emitted from the Clausthal-Zellerfeld smelter. The chapter gives a relation between geostatistical analysis and air dispersion modeling and compares the results of them. Chapter (6) presents the most important conclusions and the useful of this study.

Chapter (2) Principles of Geostatistics

2.1 Definitions of Geostatistics

Geostatistics is a branch of science that applies statistical methods which facilitates quantification of the spatial autocorrelation of soil parameters and enables spatial interpolation. It was proposed by a South African engineering geologist D.G. Krige in 1951 and developed by French geologist G. Matheron in 1962 (Rendu, 1978). Modern geostatistics is a rapidly developing branch of applied statistics with a huge set of methods and models for the analysis, processing, and representation of spatially distributed data (Goovaerts, 2001). The use of geostatistical methods make it possible to improve the reliability and quality of decisions based on spatially distributed data. Geostatistical methods in soil science are applied to study the spatial distribution of soils (Atteia, et al., 1994; Einax & Soldt, 1995; Goovaerts, 1999; Markus & McBratney 2001; Navas & Machin, 2002). The concept of geostatistics considers the soil variable as a single realization of a random function (Journel & Huijbregts, 1978; Meshalkina, 2007). The spatial variability of soil properties can be separated into component, one of which depends on the distance between the sampling points and does not depend on their specific location. The description of spatial variability with the help of semivariogram or covariance is helpful for obtaining information on the relationships between the soil properties and the environment (Krasilnikov, 2008). An important stage in any geostatistical analysis is the choice of an adequate model for the semivariogram or covariance. A model describing the spatial variability in the studied property makes it possible to predict its value at points that have not been sampled and are found at different distances from the sampling points (Rendu, 1978). An important advantage of Kriging in comparison with other interpolation methods (e.g., inverse distances) is that it identifies the error of predictions. Another advantage of the Kriging procedure is that it takes into account the specificity of the spatial variability (i.e., the correlation radius and the anisotropy) reflected in the semivariogram model (Goovaerts, 2001).

Geostatistics and Geographic Information Systems (GIS) have become useful tools to study spatial distribution, spatial uncertainty and hazard assessment of soil properties (Korre, et al., 2002; Shi, et al., 2007). The Geostatistical Analyst, an extension to ESRI's ArcGIS, has two main components, namely, the Exploratory Spatial Data Analysis toolbox and the Interpolation and Statistical Modeling Wizard. The Exploratory Spatial Data Analysis tools are interactive with the other tools provided with ArcGIS. The Geostatistical Analyst in ArcGIS provides a number of interpolation techniques that use sample points to produce a surface of the interesting phenomena. The interpolation techniques are divided into two main

types: deterministic and geostatistical methods. Deterministic interpolation techniques create surfaces from measured points, based on either the extent of similarity (e.g., Inverse Distance Weighted) or the degree of smoothing (e.g., Radial Basis Functions). Geostatistical methods are associated with the Kriging family. Ordinary, simple, universal, probability, indicator, and disjunctive Kriging, along with their counterparts in Cokriging are Kriging types. Geostatistics is divided into two distinct tasks: quantifying the spatial structure of the data and producing a prediction. Quantifying the structure, known as variography, is where we fit a spatial dependence model to our data. To make a prediction for an unknown value for a specific location, Kriging will use the fitted model from variography, and the values of the measured sample points around the prediction location. The Geostatistical Analyst creates geostatistical layer that interacts with other GIS features and options, such as projection change, clipping, querying, and exporting, among others. The generated geostatistical surfaces can subsequently be used in GIS models and in visualization using other ArcGIS extensions such as the ArcGIS Spatial Analyst and 3D Analyst (ESRI, 2001; Kumar, et al., 2007).

2.2 Geostatistical Methods

Geostatistics is the generic name for a family of techniques which are used for estimation of values at unsampled locations from limited sample data. Because Geostatistics is based on statistics, these techniques produce not only prediction surfaces but also prediction values of errors, giving us an indication of how good the predictions are. Geostatistics has been popularly applied in investigation and mapping soil properties (Webster & Oliver 2007).

2.2.1 Experimental and Theoretical Semivariogram

We can use the technique of semivariogram to measure the spatial variability of the variable representing our measured quantity. The semivariogram is based on the theory of regionalized variable which is distributed in the space and shows spatial correlation such that samples close together in space are more alike than those that are further apart. The semivariogram $\gamma(h)$ is expressed by Equation (2-1).

$$\gamma(h) = \frac{1}{2n(h)} \sum_{i=1}^{n(h)} [z(x_i) - z(x_i + h)]^2 \qquad (2\text{-}1)$$

Where $n(h)$ is the number of pairs at each step width (h), and $z(x_i)$ and $z(x_i + h)$ are the values of the variable x at locations i and $i + h$, respectively. Usage of semivariogram as an estimator of the theory variogram is based on stationarity. Intrinsic stationarity is the assumption that the variance of the

increments is the same between any two points that are at the same lag distance (h) and direction no matter which two points are chosen (David, 1977). The estimated semivariogram from known samples named as experimental or empirical semivariogram. There are many models which fit the empirical semivariogram data to get the modeled semivariogram. The main models are Spherical model (Equation (2-2)), exponential model (Equation (2-3)), and Gaussian model (Equation (2-4) among others (Rendu, 1978). The actual process of fitting a model to an empirical semivariogram is much more of an art than a science. The selected model influences the prediction of unknown values and; it represents the true spatial distribution of the variable. Figure (2-1) illustrates the structures of the spherical semivariogram model. We notice that at a certain distance the model levels out. The distance where the model first flattens out is known as the range. Sample locations separated by distance closer than the range are spatially autocorrelated, whereas locations farther apart than the range are not. The value that the semivariogram model attains at the range is called the sill. The partial sill is the sill minus the nugget. Theoretically, at zero separation distance the semivariogram value is zero. However, at a small separation distances, the deference between measurements often does not tend to zero. This is called the nugget effect. The nugget effect can be attributed to measurement error or microstructures (Webster & Oliver 2007).

$$\gamma(h) = \begin{cases} C_0 + C_1\left[\frac{3h}{2a} - \frac{1}{2}\left(\frac{h}{a}\right)^3\right] & h \le a \\ C_0 + C_1 & h \ge a \end{cases} \quad \text{Spherical model} \qquad (2\text{-}2)$$

$$\gamma(h) = C_0 + C_1\left[1 - \exp\left(\frac{h^2}{a^2}\right)\right] \quad \text{Exponential model} \qquad (2\text{-}3)$$

$$\gamma(h) = C_0 + C_1\left[1 - \exp\left(\frac{h}{a}\right)\right] \quad \text{Gaussian model} \qquad (2\text{-}4)$$

Where C_0 is the nugget variance, (h) is lag distance, and (a) is the range. The spherical model actually reaches the specified sill value C, at the specified range (a). While the exponential and Gaussian approach the sill asymptotically, with a representing practical range; the distance at which the semivariance reaches 95% of the sill value. These three models are illustrated in Figure (2-2). The Gaussian model, with its parabolic behavior at the origin, represents very smoothly varying properties. The spherical and exponential models exhibit linear behavior near the origin, appropriate for representing properties with a higher level of short-range variability (Rendu, 1978).

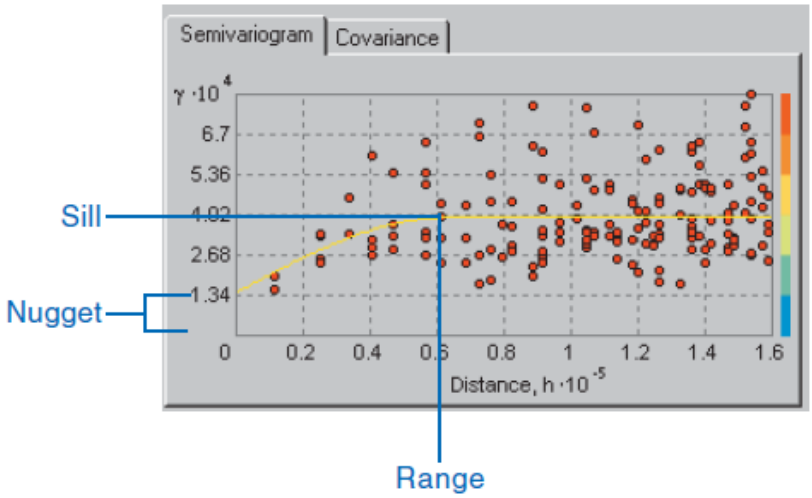

Figure (2-1) Semivariogram depicting range, sill, and nugget effect (Esri, 2001)

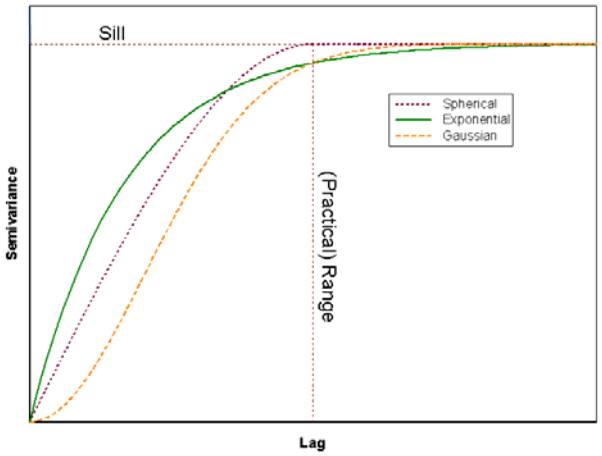

Figure (2-2) Spherical, exponential and Gaussian semivariogram models (Bohling, 2005)

2.2.1.1 Nugget Effect

The nugget effect refers to the situation when sample locations are close to each other, but the difference between measurements is not zero. There are two sources for the discontinuity at the origin for the semivariogram model. The primary one is the microstructure and the second is the sampling and measurement errors (Rendu, 1978). The total nugget effect is composed of two parts $\varepsilon(x) = \gamma_\eta\ (0) + \sigma^2$. Where $\gamma_\eta\ (0)$ is the semivariogram with a range so close to zero that it is shorter than all practical distances between data and prediction locations and σ^2 is the measurements error. Measurement errors can be attributed to error in measurement device, human recording error, changes in measurement conditions and data integration, this error can be estimated differentially by Geostatistical Analyst extension of ArcGIS using Equation (2-5) (Krivoruchko, 2001).

$$\widehat{\sigma}^2_{ME} = \frac{\sum_{xi \in D} \sum_{j=1}^{n_{xi}} \left(Z_j(x_i) - \bar{Z}(x_i)\right)^2}{N - n_D} \quad (2\text{-}5)$$

Where D is the set of all data locations that have more than one measurement, $Z_j(x_i)$ is the j^{th} measurement at location x_i, $\bar{Z}(x_i)$ is mean value at location x_i, n_i is number of observations at location $x_i \in D$, $N = \sum_i n_i$ for all x_i in D, and n_D is number of spatial locations in D.

2.2.1.2 Anisotropy

When dealing with regionalized variables in two dimensions, it is important to calculate the semivariogram in different directions to see whether its properties change or not. If the spatial correlation structure is the same in all directions, the semivariogram has isotropic properties. In this case the semivariogram depend only on the magnitude of the lag distance (h), and not the direction. In this case, the empirical semivariogram can be computed by pooling data pairs separated by the appropriate distances, regardless of direction. In many cases, however, a property shows different autocorrelation structures in different directions, and an anisotropic semivariogram model should be developed to reflect these differences. The most commonly employed model for anisotropy is geometric anisotropy, with the semivariogram reaching the same sill in all directions, but at different ranges. In geological settings, the most prominent form of anisotropy is a strong contrast in ranges in the vertical and horizontal directions, with the vertical semivariogram reaching the sill in a much shorter distance than the horizontal semivariogram (Journel & Huijbregts, 1978). To check for directional dependence in an empirical semivariogram, we have to compute semivariance values for data pairs falling within certain directional bands as well as falling within the prescribed lag limits. The directional bands are specified by a given direction, angular tolerance, and bandwidth as illustrated in Figure (2-3). In this figure, the angle of tolerance will determine the angle in which close points will be included or excluded until it reaches the bandwidth. The band width specifies how wide the search should be when determining pairs of points which will be plotted in the semivariogram.

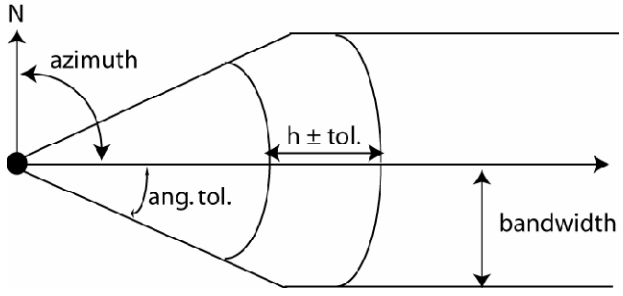

Figure (2-3) Semivariogram directional bands (Bohling, 2005)

2.2.2 Kriging as Estimator

Kriging is a method of interpolation named after a South African mining engineer named D. G. Krige who developed the technique in an attempt to more accurately predict ore reserves. Kriging is a special regression method for interpolation of spatially correlated data under variance minimization. The kriging Interpolator is best linear unbiased prediction to determine the intensity of a phenomenon at unsampled locations. Kriging minimizes the prediction variance. Since that estimation errors can be mapped to assist in the decision-making process. The prediction standard error maps show a distribution of the square root of prediction variance. The prediction standard error maps quantify the uncertainly of the prediction. Kriging relies on stationarity assumptions. Intrinsic stationarity required that the random errors have zero mean and the variogram between any two random errors depends only on the distance and direction that separates them, not their exact locations. The distribution of heavy metals in the soil can be represented by a general Equation (2-6) as illustrated in Figure (2-4) (Atteia, 1994; Webster & Oliver 2007).

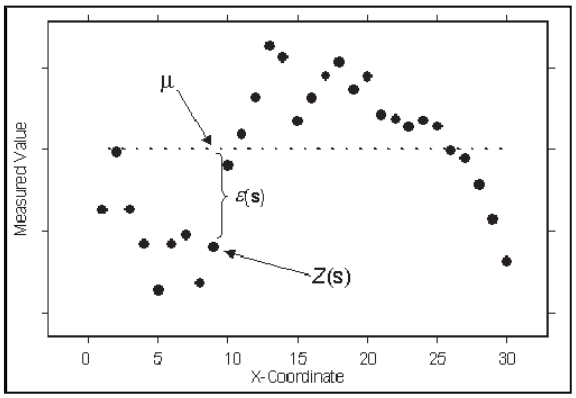

Figure (2-4) General model of Kriging (ESRI, 2001)

$$Z(x) = \mu + \varepsilon(x) \qquad (2\text{-}6)$$

Where $Z(x)$ is the value of the samples at the location x which has (X, Y) coordinates values. μ is the constant mean of the data, and ε(x) is a random error. The Kriging predictor is formed as a weighted sum of the data as given in Equation (2-7).

$$\hat{Z}(x_0) = \sum_{i=1}^{N} \lambda_i Z(x_i) \qquad (2\text{-}7)$$

Where $Z(x_i)$ is the measured value at the i^{th} location; λ_i is unknown weight for the measured value at the i^{th} location and x_0 is the prediction location or unsampled location. The unknown weight λ_i depends on the semivariogram, the

distance to prediction location and the spatial relationships among the measured values around the prediction location. When making predictions for several locations, it is expected that some of the predictions to be above the actual values and some below. On average, the difference between the predictions and the actual values should be zero. This is referred to as making the prediction unbiased. To ensure the predictor is unbiased for the unknown measurement, the sum of the weight λ_i must equal one. Using this constraint, make sure the difference between the true value and the predictor is as small as possible. That is minimizing the statistical expectation of the following Equation (2-8).

$$\left(\hat{Z}(x_0) - \sum_{i=1}^{N} \lambda_i Z(x_i)\right)^2 \tag{2-8}$$

From which the kriging equations were obtained. By minimizing its expectation, on average, the kriging predictor is as close as possible to the unknown value. The solution to the minimization, constrained by unbiased, gives the kriging Equation (2-9).

$$\Gamma \quad * \quad \lambda \quad = \quad g$$

$$\begin{pmatrix} \gamma_{11} & \cdots & \gamma_{1n} & 1 \\ \vdots & \ddots & \vdots & \vdots \\ \vdots & \ddots & \vdots & \vdots \\ \gamma_{n1} & \cdots & \gamma_{nn} & 1 \\ 1 & \cdots & 1 & 0 \end{pmatrix} * \begin{pmatrix} \gamma_1 \\ \vdots \\ \vdots \\ \gamma_n \\ m \end{pmatrix} = \begin{pmatrix} \gamma_{10} \\ \vdots \\ \vdots \\ \gamma_{n0} \\ 1 \end{pmatrix} \tag{2-9}$$

Most of the element can be filled in if we know the semivariogram. The gamma matrix Γ contains the modeled semivariogram values between all pairs of sample locations, where γ_{ij} denotes the modeled semivariogram values based on the distance between the two samples identified by i^{th} and j^{th} locations. The vector (g) contains the modeled semivariogram values γ_{i0} based on the distance between the i^{th} sample location and the prediction location (unknown value). The unknown (m) in the vector (λ) is also estimated and it arises because of the unbiasedness constraint. After calculated the modeled semivariogram the unknown weighted (λ) can be calculated by Equation (2-10).

$$\lambda = \Gamma^{-1} * g \tag{2-10}$$

One of the strengths of using kriging is that it is possible to measure the uncertainty of the prediction which named kriging variance (Equation (2-11)) that is

calculated by multiplying the vector (λ) time the vector (g). The square root of the kriging variance is called the kriging standard error as given by Equation (2-12).

$$\text{kriging variance} = {\sigma_k}^2 = \lambda \ * g \tag{2-11}$$

$$\text{kriging standard error} = \sqrt{{\sigma_k}^2} \tag{2-12}$$

2.2.3 Statistics and Lognormal-Transformation

Skewness characterizes the degree of symmetry of a distribution around its mean. Positive skewness indicates a long right tail, and the negative one indicates a long left tail, while zero skewness indicates symmetry around the mean. Kurtosis is a measure of whether the data are peaked or flat relative to a normal distribution. That is, data sets with high kurtosis tend to have a distinct peak near the mean value and low kurtosis tends to have a flat top near the mean rather than a sharp peak. Data sets with low kurtosis tend to have a flat top near the mean rather than a sharp peak. A uniform distribution would be the extreme case. The normal distribution has a skewness nearly of zero value and kurtosis of 3. The histogram is an effective graphical technique for showing both the skewness and kurtosis of data set. For univariate data $x_1, x_2, \ldots, x_N$, the formulas for skewness and kurtosis are given by Equation (2-13) and Equation (2-14), respectively (Webster & Oliver 2007).

$$\text{skewnwss} = \frac{\sum_{i=1}^{N}(x_i - \bar{x})^3}{(N-1)(\text{std})^3} \tag{2-13}$$

$$\text{kurtosis} = \frac{\sum_{i=1}^{N}(x_i - \bar{x})^4}{(N-1)(\text{std})^4} \tag{2-14}$$

Where $\bar{x}$ is the mean, std is the standard deviation, and N is the number of data set. Standard deviation measures how widely the values are dispersed from the mean. Standard deviation calculated by the square root of the sample variance of a set of N values, Equation (2-15).

$$\text{Std} = \sqrt{\frac{1}{N-1}\sum_{i=1}^{N}(x_i - \bar{x})^2} \tag{2-15}$$

Formation of Kriging estimation does not depend on any particular sample density distribution. However, high skewness and outliers of data can impair the variogram structure and the Kriging results. It is often observed that, environmental variables are positively skewed and data transformation is necessary to normalize such data set. If the data are clearly lognormal the logarithm of the observations,

$y(x_i)$ can be estimated with a lower estimation variance than the raw data $z(x_i)$, Equation (2-16) (Rendu, 1978).

$$y(x_i) = \ln\left[\left(z(x_i)\right)\right] \quad (2\text{-}16)$$

Logarithmic transformation is widely applied in order to normalize positively skewed data sets. However, it is observed that data sets in environmental sciences do not always follow lognormal distribution. In such cases, a power transformation is needed, and Box–Cox transformation is one of the most frequently used of these, Equation (2-17) (Zhang & Selinus, 1997).

$$y(x_i) = \begin{cases} \frac{x^{\beta}-1}{\beta} & \beta \neq 0 \\ \ln(x_i) & \beta = 0 \end{cases} \quad (2\text{-}17)$$

Where y is the transformed value; and x is the value to be transformed. For a given data set$(x_1, x_2, \ldots, x_n)$, the parameter β is estimated based on the assumption that the transformed values $(x_1, x_2, \ldots, x_{n1})$ are normally distributed. When $\beta = 0$, the transformation becomes the Logarithmic transformation.

2.3 Geographic Information System (GIS)

Geographic information systems (GIS), in the sense of computer tools for handling spatial data, have been used since 1960s. Their initials development was mainly in North America, simulated by the need to map, plan and manage large areas of terrain, but major contributions came also from Britain and other European countries (Burrough, 2001). A GIS is an organized collection of computer hardware, software, geographic data, and personnel designed to efficiently enter, manage, store, update, manipulate, edit, and display all forms of geographically referenced information (Busch, 2007). A geographic information system (GIS) is an information system that is designed to work with data referenced by spatial or geographic coordinates. In other words, a GIS is both a database system with specific capabilities for spatially-reference data, as well as a set of operations for working with data. Today, most commercial GIS provide facilitates for working with raster and vector data. They also provide data base facilities for storing retrieving, modifying the attributes of the spatial entities that have been recognized for the given application (Longley et al., 2005). ArcGIS Geostatistical Analyst is an extension to ArcGIS desktop that provides a powerful suite of tools for spatial data exploration and surface generation. It effectively bridges the gap between geostatistics and GIS analysis by enabling to model spatial phenomena, interpolate and predict values within the study area. With ArcGIS Geostatistical Analyst, we can

create surfaces from data measurements taken over areas where collecting information for every location would be impossible or cost prohibitive. We can examine sample data, evaluate uncertainties, and create customized interpolation surfaces for more informed decision making (ESRI (white papers), 2001).

2.3.1 Data Exploration

Exploratory Spatial Data Analysis (ESDA) allows examining the raw data in different ways. Before creating a prediction surface, ESDA enables a deeper understanding of the phenomena which are investigated so that it can make better decisions on issues relating to the data. Exploring the distribution of the data, looking for global and local outliers, looking for global trends, examining spatial autocorrelation, and understanding the variation among multiple datasets are all useful tasks to perform on raw data. The ESDA tools can assist with these tasks to take decisions in transforming the data to lognormal or any another power transformation and in fitting the theoretical semivariogram. The ESDA environment is composed of a series of tools, such as Histogram, trend analysis and semivariogram/covariance cloud among others. The histogram tool provides univariate description of the raw data. It displays the frequency distribution and gives summery statistics such as Min, Max, Mean, and Kurtosis among others as presented in Figure (2-5). The semivariogram/covariance cloud shows the empirical semivariogram for the pairs of locations within a dataset and plots them as a function of the distance between the two locations. This tool used to examine the local characteristics of spatial autocorrelation within a dataset. The semivariogram cloud is illustrated in Figure (2-6), where each red dot is a semivariogram between a pair of the data. The semivariogram should be small value for small lag distance (h) and increases with increasing the lag distance. This characteristic can be examined be select any red dot and show the distance between this pair. In Figure (2-6) some semivariogram value are selected beside the X-Y axes corner and the lag distance is illustrated in Figure (2-7) as a small distances. Also three semivariogram dot are selected in north-west of X-Y axes and illustrated as long distances in Figure (2-7). Semivariogram cloud tool can be used also to examine the semivariogram value in different directions (ESRI, 2001).

2.3.2 Geostatistical Wizard of ArcGIS

The Geostatistical Wizard is a dynamic set of pages that are designed to guide through the process of constructing and evaluating the performance of an interpolation model. Choices made on one page determine which options will be available on the following pages and how the interact with the data to develop a suitable model. During construction of an interpolation model, the wizard allows changes in parameter values, suggests or provides optimized parameter values,

and allows moving forward or backward in the process to assess the cross-validation results to see if the current model is satisfactory or if some of the parameter values should be modified. This flexibility, in addition to dynamic data and surface previews, make the wizard a powerful environment to build interpolation models.

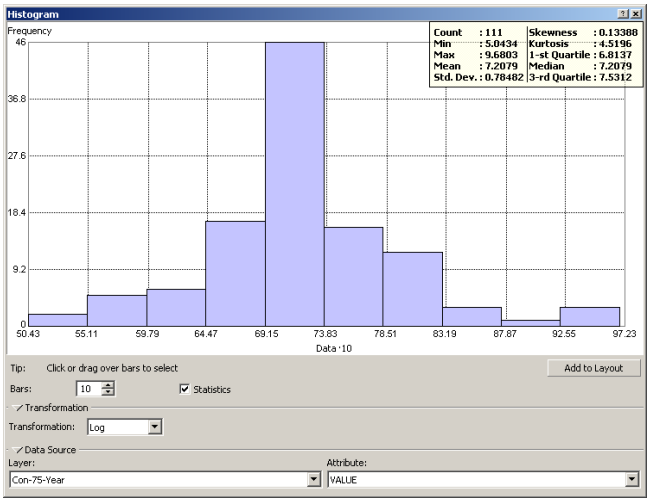

Figure (2-5) Histogram analysis in ESDA environment

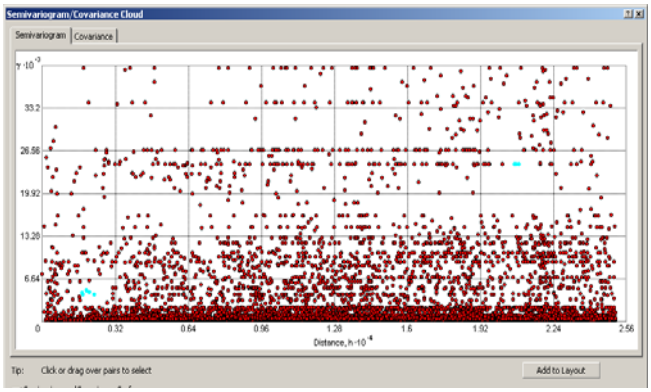

Figure (2-6) Semivariogram/covariance cloud tool in ESDA

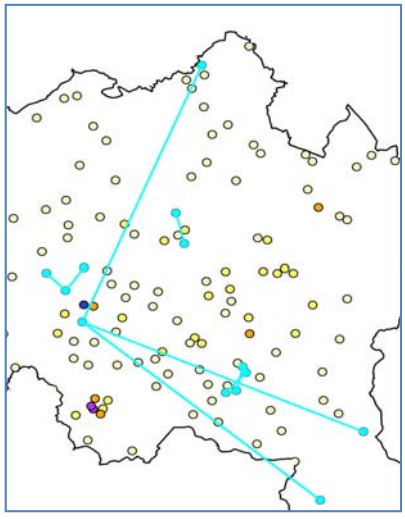

Figure (2-7) Lag distances for selected semivariogram from Figure (2-6)

A simple version of this workflow is represented graphically through Figure (2-8) to Figure (2-11) (ESRI, 2001). The first dialog box in the Geostatistical wizard is method selection as presented in Figure (2-8). There are six types of kriging available and each type of kriging has two to four types of maps. Ordinary Kriging assumes a constant but unknown mean in the dataset, simple kriging assumes a constant known mean, and Universal Kriging assumes a varying mean over space. The other three types of kriging are more specialized to analyze the risk of pollutants or using cutoff value for specific reasons. The Semivariogram/Covariance Modeling dialog box examines spatial relationships between measured points; Figure (2-9). The semivariogram explore the assumption that things that are close together are more alike. Each pixel represents the average of all pairs within a given distance/direction bin. The width of each pixel and the number of bins is determined by the Lag Size and Number of bins boxes on the lower right corner. There is a Show Anisotropy box, which allows restricting the view to a certain direction. Each dot represents one bin of the semivariogram surface. The process of fitting a semivariogram model is known as variography. The fitted variogram model is shown by a blue line. Searching Neighborhood illustrated in Figure (2-10) shows the size of the local neighborhood within which each kriging system is solved. Much geostatistical structure can be defined in this step like sector type and number of points used in prediction, among others. On the left hand side is a map of the data locations and the weight of each included point. The Cross Validation dialog box Figure (2-11) gives some idea of how well the model predicts the values at the unknown locations.

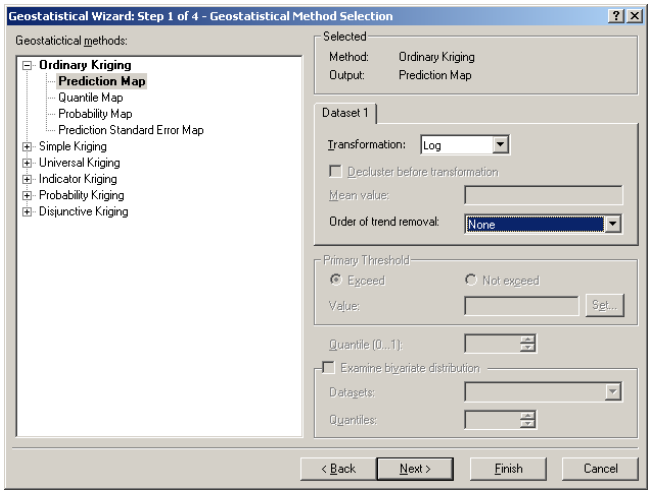

Figure (2-8) Selection dialog box in Geostatistical Wizard

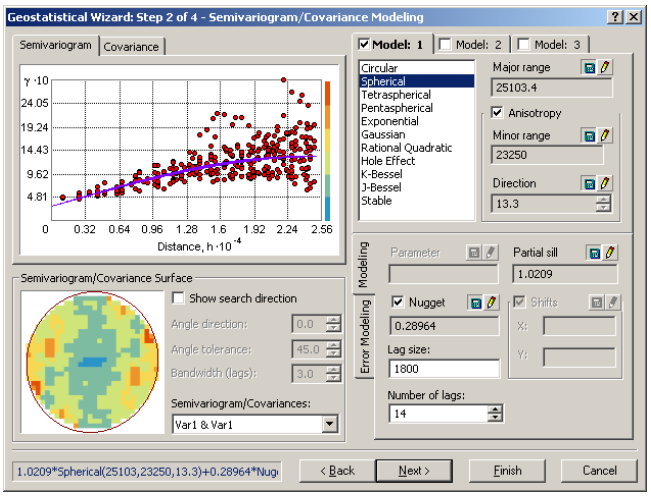

Figure (2-9) Semivariogram/covariance modeling dialog box

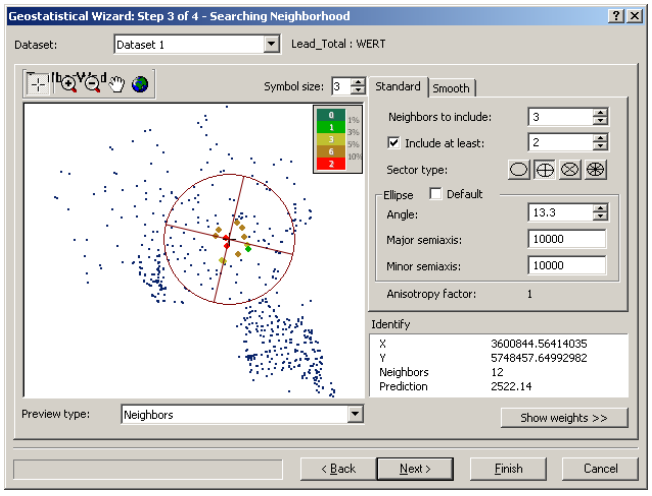

Figure (2-10) Searching neighborhood dialog box

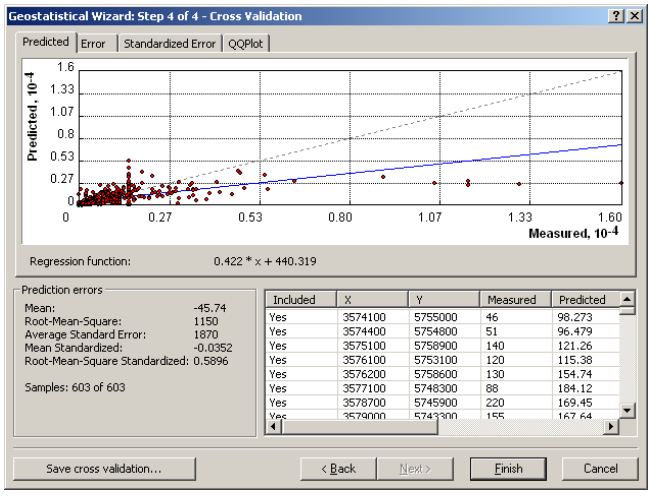

Figure (2-11) Cross validation dialog box on Geostatistical wizard

Chapter (3) Theory of Air Dispersion Modeling

3.1 Introduction to Air Dispersion Modeling

Mined ores are processed to concentrate the minerals of interest and removing the waste materials. In the case of metal ores, these mineral concentrates usually need to further processes to separate the required metal from other elements in the ore. Smelting is the process of separating the metal from impurities by heating the concentrate to specific temperatures which cause the minerals to melt. Smelting the concentrate produces a metal or a high-grade metallic mixture along with a solid waste product called slag. These smelters release gases and particulate matters from their chimneys (van Alphen, 1999; Kiikkilä, 2003). The released metal particles and gases can contaminate the soil in the vicinity of smelters and destroying much of the vegetation (Schroeder & Reuss, 1883). In addition, particulate matter emitted from smelters may include toxic metals such as arsenic, cadmium and mercury (Williamson et al., 2004). Air dispersion modeling is the science which studies the transportation of gases and particulate maters emitted from sources to the environment. An air dispersion model is a series of mathematical equations used to calculate the concentration of pollutants at various points surrounding emission sources (Awasthi et al., 2006). The air simulation model requires two types of data inputs, source information and meteorological data. Source data such as rate of emission, stack height and diameter, gas exit velocity and temperature. Meteorological data are wind velocity, atmospheric stability, mixing height, and ambient temperature. With these inputs, the model simulates mathematically the dispersion and the transport of contaminations for a particular period and at specific receptor locations (Schnelle & Dey, 2000). There are five types of air dispersion models, as well as some hybrids of the five types. They are Box Model, Gaussian Model, Lagrangian Model, Eulerian Model and Dense Gas Model. The box model is the simplest one of them. It assumes the study zone as a shape of a box. The model also assumes that the air plume inside the box distributes homogeneously and uses this assumption to estimate the average pollutant concentrations at each point within the box (Barrat, 2001). Lagrangian dispersion model dissipates air plume into parcels, and it models the motion of the parcels as a random walk process. The Lagrangian model then calculates the dispersion of pollutants by estimating the statistics of the trajectories of large number of the plume parcels. Eulerian dispersions model is similar to the Lagrangian model in that it follows the movement of plume parcels as they move from their initial location to any other place. The most important difference between the two models is that the Eulerian model uses a fixed three-dimensional Cartesian grid as a frame of reference rather than a moving frame of the reference (Ismael et

al., 2009). Dense gas models simulate the dispersion of dense gas plumes that are heavier than air. The Gaussian Model is perhaps the oldest and the most commonly used model type (Awasthi et al., 2006). It assumes that the air pollutant dispersion has a Gaussian distribution, meaning that the pollutant distribution has a normal probability distribution. Gaussian models are most often used for predicting the dispersion of continuous, buoyant air pollution plumes originating from ground or elevated sources. Gaussian models are based on a Gaussian distribution of the plume. The normal distribution on the plume depends on the vertical (σ_z) and on the horizontal (σ_y) standard deviations. At any point from a source, the width of the plume is determined by (σ_y) and (σ_z), which are defined according to atmospheric stability categories and distances along the wind direction (Ismael et al., 2009).

3.2 Meteorological Parameters

Meteorological parameters pertains to the atmosphere, such as wind, temperature, air pressure, density and other phenomena that affect the motion of an air parcel from place to another. Ambient temperature, wind speed and wind velocity are very important parameters in studying dispersion of pollutants. Potential temperature is the change of temperature with vertical height in the atmosphere; it is also named as Lapse rate.

3.2.1 The Atmosphere and Lapse Rate

A lapse rate is defined as the rate of change in temperature while moving upwards through the Earth's atmosphere. The actual lapse rate in the atmosphere is approximately -6 to -7 ^{0}C/km but it varies widely depending on location and time of day. An adiabatic process is one in which there is no transfer of heat or mass across the boundaries of the air parcel. A dry air parcel rising in the atmosphere cools at a dry adiabatic rate of 9.8 ^{0}C/km and has a lapse rate of -9.8 ^{0}C/km. Air is considered dry as long as any water in it remains in a gaseous state. A rising parcel of dry air containing water vapor will continue to cool at the dry adiabatic lapse rate until it reaches its condensation temperature, or dew point. At this point the pressure of the water vapor equals the saturation vapor pressure of the air and some of water vapor begins to condense. Condensation releases latent heat in the parcel, and thus the cooling rate of parcels slows. This new rate called the wet adiabatic lapse rate and it is assumed to be approximately -6 to -7 ^{0}C/km (Beychok, 2005). The actual temperature profile of the ambient air shows the environmental lapse rate, sometimes called the prevailing or atmospheric lapse rate. Environmental lapse rate is the result of complex interactions of meteorological factors and is usually considered to be a decrease in temperature with height. The temperature profile can vary considerably with altitude, sometimes changing at a

rate greater than the dry adiabatic lapse rate and sometimes changing less. The condition when temperature actually increases with altitude is referred to as a temperature inversion which is important in air pollution because it hinders vertical air motion (Barratt, 2001). Figure (3-1) indicates the dry adiabatic lapse rate and atmospheric lapse rate.

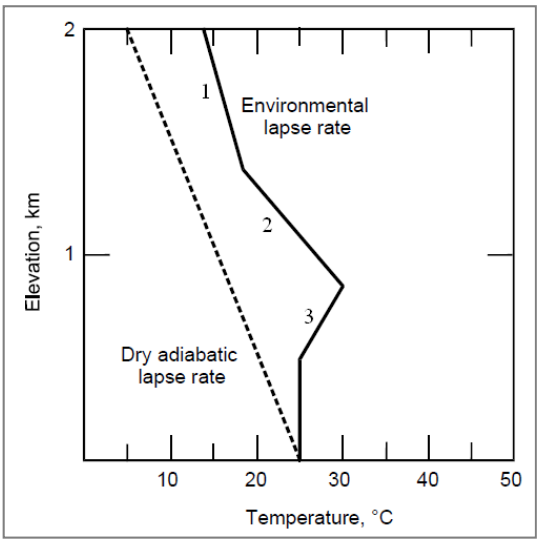

Figure (3-1) Dry adiabatic and Environmental lapse rate
1-Temperature changes less than dry adiabartic lapse rate. 2-Temperature changes greater than dry adiabatic lapse rate (super adiabatic lapse rate). 3- Temperature inversion.

3.2.2 Atmospheric Stability

The amount of turbulence in the ambient air has a major effect upon the rise of stack plumes and upon the dispersion of the plumes. Atmospheric variations in both thermal and mechanical turbulence and in wind velocity are greatest in the layer in contact with the surface. Turbulence induced by buoyancy forces in the atmosphere is closely related to the vertical temperature structure (Lapse rate) (Schnelle & Dey 2000). The amount of turbulence can be categorized into stability classes. By stability, we refer primarily to the degree of turbulence (both thermal and mechanical) presents in the atmosphere that can disperse airborne material. Gifford modified a system of stability classification based on the suggestion of Pasquill at British Meteorological Office; these classifications are known widely as Pasquill-Gifford stability categories (Schnelle & Dey 2000). The Pasquill-Gifford Stability Classes are A, B, C, D, E and F as indicated in Table (3-1) (Beychok, 2005). Atmospheric stabilities A, B, and C are daytime stability classes. Class A is the most unstable and occurs during daylight hours when maximum incoming solar radiation is existence with little or no cloud cover and with relatively light wind speed. Under these conditions, the ground will be warming rapidly and transferring heat to the lowest layer of air near the surface of the ground. This warmed air will then transfer this heat upward through turbulent mixing of the air. Under these

conditions, material released into the air will be rapidly dispersed. Stability classes B and C also refer to unstable atmospheric condition; however, B is moderately unstable and C is considered slightly unstable. Atmospheric stability class D refers to a neutral atmosphere. This condition may occur either during the daytime or during the nighttime. Class D is almost always the most likely stability class that occurs at a given location. Stability class E and F are nighttime stability classes. They refer to atmospheric conditions in which little energy is available in the atmosphere to cause rapid dispersion to occur. Class F stability is the most stable condition (Murphy, 1998). Table (3-2) provides the meteorological conditions that define each of the Pasquill-Gifford stability class (Barrat, 2001). Pollutants dispersion has strong relation with the stability. Such an atmosphere is said to be stable, since the vertical motion of pollutants is hindered. An extreme stability condition is the inversion. During inversion, the pollutants can't be dispersed and they accumulate in the lower atmosphere, leading to a very big pollution problem. The entire spectrum of atmospheric conditions (ranging from super-adiabatic to inversion) is divided into the six Pasquill stability classes as illustrated in Figure (3-2), with each class defined as being within a specific range of atmospheric air temperature gradients.

Table (3-1) Pasquill-Gifford stability classes (Beychok, 2005)

Stability class	Definition	Atmospheric Temperature gradient, (^{0}C/km)
A	Extremely unstable	less than -18.9
B	Moderately unstable	-18.9 to 16.9
C	slightly unstable	-16.9 to -14.9
D	Neutral	-14.9 to -4.9
E	slightly stable	-4.9 to 14.9
F	Moderately stable	More than 14.9

Table (3-2) Meteorological conditions that define the Pasquill-Gifford stability classes (Barrat, 2001)

Wind speed At 1o m height	Daytime Amount of incoming solar radiation			Night hours Cloud cover	
m/s	Strong	Moderate	Slight	> 4/8	< 3/8%
< 2	A	A – B	B	E	F
2 – 3	A – B	B	C	E	F
3 – 5	B	B – C	C	D	E
5 – 6	C	C – D	D	D	D
> 6	C	D	D	D	D
- Class D applies to heavily overcast skies, at any Windspeed day or night - Night is defined as the period from 1 hr before sunset to 1 hr after sunrise					

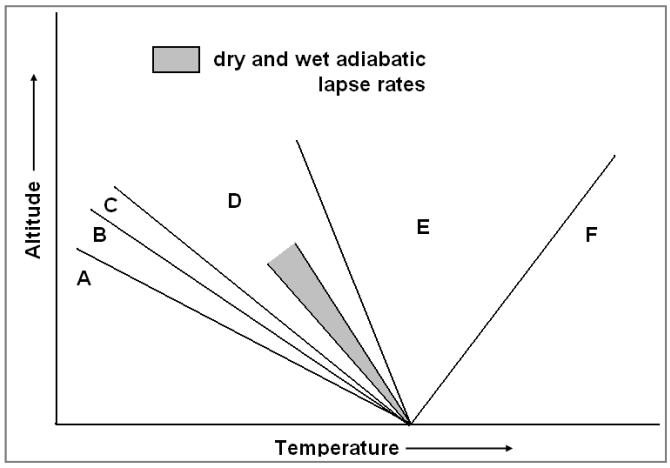

Figure (3-2) Pasquill-Gifford stability classes defined by different lapse rate (Beychok, 2005)

Incoming radiation that would be strong with clear skies can be expected to be reduced to moderate or slight according to the cloud cover. Table (3-3) indicates the altitude angle and the solar intensity (Schnelle & Dey, 2000). Cloudiness decreases incoming solar radiation and should be considered along with solar altitude in determining solar radiation.

Table (3-3) solar altitude determine the amount of solar radiation (Schnelle & Dey, 2000)

Solar Altitude	Insolation
$60^{o} < h$	Strong
$35° < h \leq 60°$	Moderate
$15° < h \leq 35°$	Slight
$h \leq 15°$	Weak

3.2.3 Plume Shape and Atmospheric Stability

The shape of an elevated plume is a depending maily on the stability of the atmosphere in which the plume is releases from stack height. Figure (3-3) illustrates the plume shape according to atmospheric stabilities. Looping plume occurs in extremely unstable conditions (stability A). While unstable conditions are generally favorable for pollutant dispersion, high ground concentrations can occur if the plume loops downwards to the surface. Coning plume characterizes the neutral or slightly unstable conditions (stability B). It occurs on cloudy days or on sunny days on which the plume disperses fairly equally into both horizontal and vertical dimensions. Fanning plume occurs in stable conditions. The inversion laps rate hinders vertical motion without prohibiting horizontal motion. In this case the plume spreads horizontally and travels long distances with little dilution. Lofting, if either due to a very high stack or due to a very high buoyant plume rise the plume source is effectively above the inversion, then the plume is dispersing upwards. The inversion

acts like a solid boundary. This situation protects the ground receptor from high pollutant levels. Fumigation; if the plume is released just under an inversion layer, a serious air pollution situation could happen (during a clear night). As the ground warms in the morning, air below an inversion layer becomes unstable. When the instability reaches the level of the plume that is still trapped below the inversion layer, the pollutants can be rapidly transported down toward the ground (Beychok, 2005).

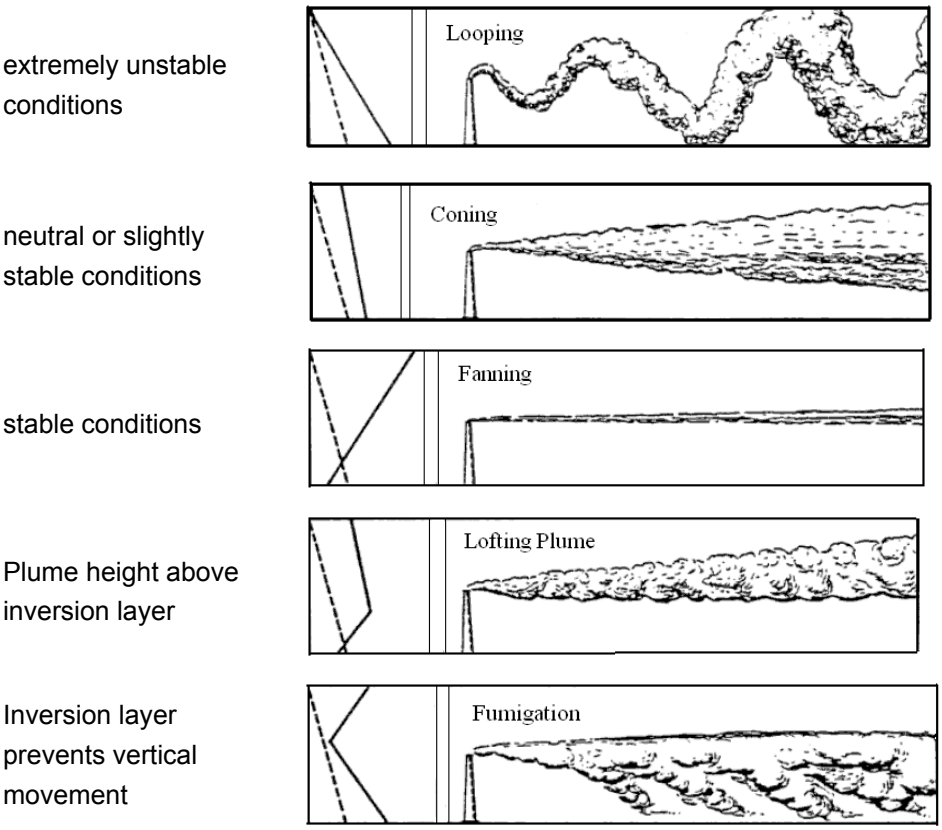

Figure (3-3) Different Plume behavior for different atmospheric conditions (Beychok, 2005)
(Dash line refers to dry adiabatic lapse rate, and solid line represents the atmospheric lapse rate)

3.3 Gaussian Plume Dispersion Model

Gaussian model is still used by the environmental agencies all over the world for its regulatory applications. Because of its well-known intrinsic limits, the reliability of a Gaussian model depends strongly on the determination of dispersion parameters based on the turbulence structure of the planetary boundary layer or mixing height. Pollutant transport is assumed to be governed by the atmospheric advection–diffusion Equation (3-1) (Hanna et al., 1982).

$$\frac{\partial C}{\partial t} = \frac{\partial}{\partial x}\left(K_x \frac{\partial C}{\partial x}\right) + \frac{\partial}{\partial y}\left(K_y \frac{\partial C}{\partial y}\right) + \frac{\partial}{\partial z}\left(K_z \frac{\partial C}{\partial z}\right) - w_x \frac{\partial C}{\partial x} - w_y \frac{\partial C}{\partial y} - w_z \frac{\partial C}{\partial z} + v_t \frac{\partial C}{\partial z} - S(x, y, z) + R(x, y, z) \quad (3\text{-}1)$$

where C is the particle concentration at the Cartesian coordinate [x, y, z]; K_x, K_y and K_z are the turbulent diffusion coefficients in the x, y and z directions, respectively; w_x, w_y and w_z are the x, y and z components of mean wind speed, respectively; v_t is particle fall speed; S(x, y, z) is a sink term, representing particle loss rate; R(x, y, z) is a source term, representing particle production rate. Analytical solutions to the complete advection–diffusion equation cannot be given but in a few specialized cases, and numerical solutions can be easily "interpreted" as the simple Gaussian model. The solution of Gaussian plume model is given by Equation (3-2), which computes the atmospheric concentration at a given point (x, y, z) downwind from the release location (Ermak, 1976; Vesovic, et al., 2001). Figure (3-4) illustrates the visualization of a Gaussian air pollution dispersion plume based on Gaussian atmospheric dispersion model.

$$Con(x, y, z) = \frac{Q\,K\,(VF)*(DF)}{2\pi u\,\sigma_z \sigma_y} \exp\left[-\frac{1}{2}\left(\frac{y}{\sigma_y}\right)^2\right] \quad (3\text{-}2)$$

Where:

Con = concentration of the substance at location x, y, z in $\mu g/m^3$

Q = rate that the substance is released into atmosphere (in g/s)

$K =$ a scaling coefficient to convert calculated concentrations to desired units (default value of $1x10^6$ for Q in g/s and concentration in $\mu g/m^3$).

VF = vertical term, due to the reflection from the inversion layer.

x= downwind distance along the wind direction, m.

z = the height of receptor above the ground at which C is calculated.

y = number of meters cross wind from release point at which C is calculated.

u = wind speed at the release height in m/s.

σ_y= standard deviation of the distribution of the substance in the crosswind (y) direction, as a function of x

σ_z= standard deviation of the distribution of the substance in the vertical (z) direction, as a function of x

DF= dry deposition factor or depletion factor. In case of particle size less than $0.1\ \mu m$ or gases, this factor is neglected.

The vertical term includes the effects of source elevation, receptor elevation, plume rise, and mixing height. The vertical term without any deposition is calculated

by Equation (3-3) (EPA, 1992). At long distances the vertical term is changed to the form given in Equation (3-4).

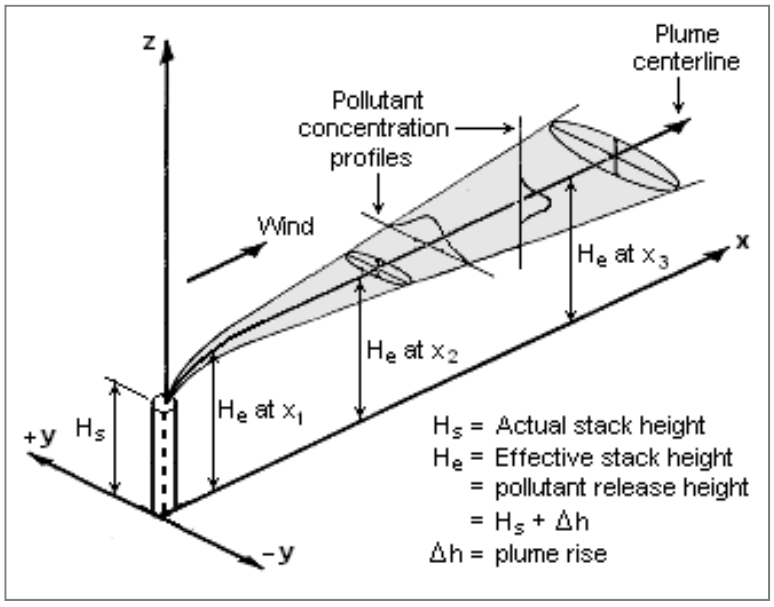

Figure (3-4) Visualization of a buoyant Gaussian air pollution dispersion plume

$$VF = \exp\left[-\frac{1}{2}\left(\frac{z_r - H_e}{\sigma_z}\right)^2\right] + \exp\left[-\frac{1}{2}\left(\frac{z_r + H_e}{\sigma_z}\right)^2\right] + \sum_{i=1}^{\infty}\left\{\exp\left[-\frac{1}{2}\left(\frac{H_1}{\sigma_z}\right)^2\right] + \exp\left[-\frac{1}{2}\left(\frac{H_2}{\sigma_z}\right)^2\right] + \exp\left[-\frac{1}{2}\left(\frac{H_3}{\sigma_z}\right)^2\right] + \exp\left[-\frac{1}{2}\left(\frac{H_4}{\sigma_z}\right)^2\right]\right\} \quad (3\text{-}3)$$

Where:

H_e = The effective plume height which includes the stack height and the plume rise

$H_1 = z_r - (2iH_m - H_e)$

$H_2 = z_r + (2iH_m - H_e)$

$H_3 = z_r - (2iH_m + H_e)$

$H_4 = z_r + (2iH_m + H_e)$

z_r is the receptor height above the ground, m, which equal to zero in ground surface. H_m is the mixing height, m

$$V = \frac{\sqrt{2\pi}\sigma_z}{z_i} \qquad \sigma_z/z_i \geq 1.6 \quad (3\text{-}4)$$

The depletion factor is presented in Equation (3-5) which applied for particulate matters greater than $0.1\ \mu m$ (Ermak, 1976; Vesovic, et al., 2001).

$$DF = \exp\left[-\frac{v_t}{u}\frac{H_e\, x}{\sigma_z^2} - \frac{v_t^2 x^2}{2u^2\sigma_z^2}\right] * \left[1 - \sqrt{2\pi}\frac{Vx}{u\sigma_z}\exp\xi^2\ \mathrm{erfc}\,\xi\right] \quad (3\text{-}5)$$

$$V = V_d - \frac{v_t}{2} \quad (3\text{-}6)$$

$$\xi = \frac{h}{\sqrt{2}\sigma_z} + \sqrt{2}\,\frac{Vx}{u\sigma_z} \quad (3\text{-}7)$$

Where, v_t and V_d are settling and deposition velocities of the particle; and erfc is the complementary error function. Calculations of settling and deposition velocities are given in details in the section of dry depositions. As the plume of airborne particulate is transported downwind, such deposition near surface reduces the concentration of particulates in the plume, and thereby alters the vertical distribution of the remaining particulates. As a result, the plume centerline height reduced, and the vertical concentration distribution is no longer Gaussian. A corrected source depletion model developed by Horst, 1977 is used to obtain a vertical term that incorporates both the gravitational settling of the plume and the removal of plume mass at the surface. The effective plume height in equation is replaced by Formula (3-8).

$$h_{ed} = H_e - h_v = H_e - \frac{x}{u}v_s \quad (3\text{-}8)$$

3.3.1 Lateral and Vertical Coefficients of Dispersion

The most important input parameters to the Gaussian model are the standard deviations (σ) along the wind direction, also known as dispersion coefficients. These coefficients express the speed of concentrations across the plume dimensions. For a given stability class, the diffusion coefficient can be determined as a function of the downwind distance from the source. Briggs proposed a series of interpolation equations to calculate the vertical and lateral dispersion coefficients for a plume emitted from elevated stack source. The equations for these coefficients are summarized in Table (3-4) and the general form is presented in Equation (3-9) (Schnelle & Dey, 2000).

$$\sigma_{y,z} = ax(1 + bx)^c \quad (3\text{-}9)$$

Where x is the downwind distance from the emitted source, the coefficients a and b and the exponent c are given in Table (3-4) for the various stability classes and the two kinds of terrain roughness considered (open country and urban). Coefficients σ_z and σ_y are functions of downwind distance x, since the characteristic of turbulence velocities are different in the horizontal and vertical directions. They depend on atmospheric conditions; for stable conditions, the turbulent velocities are very low and hence the dispersion coefficients small; for unstable conditions, the

turbulence is vigorous and we expect much larger dispersion coefficients. Experimental measurements over a range of stability conditions give the results of dispersion coefficients as plotted in Figures (3-5) and (3-6) respectively (Beychok, 2005).

Table (3-4) Brigg's Formulae (1973) for the Coefficients of Dispersion (Briggs, 1973)

kind of Terrain	Class	σ_y (m)	σ_z (m)
Rural	A	$0.22x(1+0.0001x)^{-0.5}$	$0.20x$
	B	$0.16x(1+0.0001x)^{-0.5}$	$0.12x$
	C	$0.11x(1+0.0001x)^{-0.5}$	$0.08x(1+0.0002x)^{-0.5}$
	D	$0.08x(1+0.0001x)^{-0.5}$	$0.06x(1+0.0015x)^{-0.5}$
	E	$0.06x(1+0.0001x)^{-0.5}$	$0.03x(1+0.0003x)^{-1}$
	F	$0.04x(1+0.0001x)^{-0.5}$	$0.016x(1+0.0003x)^{-1}$
Urban	A - B	$0.4x(1+0.0004x)^{-0.5}$	$0.3x(1+0.0010x)^{-0.5}$
	C	$0.28x(1+0.0004x)^{-0.5}$	$0.25x$
	D	$0.2x(1+0.0004x)^{-0.5}$	$0.18x(1+0.0003x)^{-0.5}$
	E - F	$0.14x(1+0.0004x)^{-0.5}$	$0.1x(1+0.0015x)^{-0.5}$

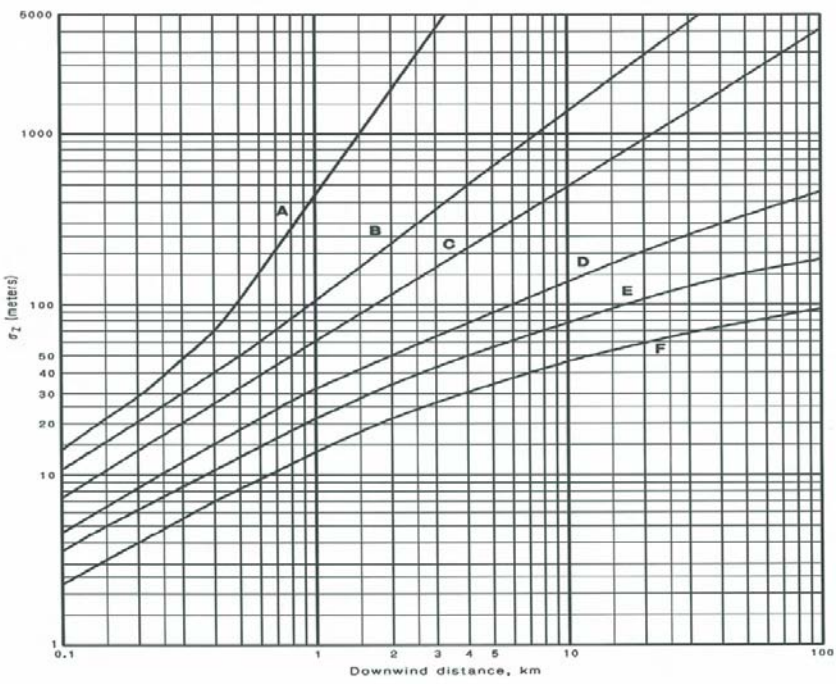

Figure (3-5) Vertical dispersion coefficient as a function of downwind distance from the source and stability conditions (Beychok, 2005)

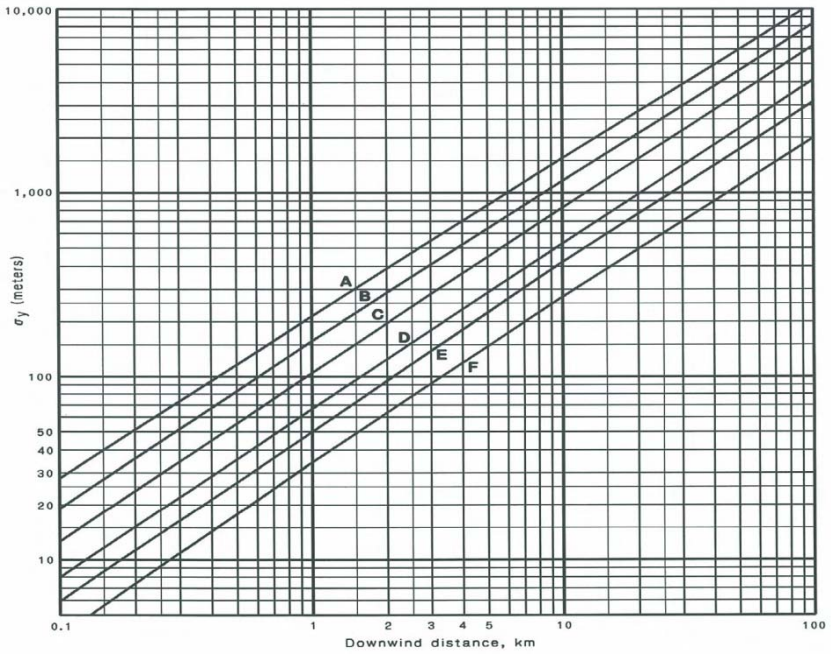

Figure (3-6) Horizontal dispersion coefficient as a function of downwind distance from the source and stability conditions (Beychok, 2005)

3.3.2 Adjusting of Wind Speed

The input wind speed to the air dispersion model is considered to be representative of the conditions in which the plume is dispersing. The wind at the stack elevation is commonly used as an approximation to this condition. Because the wind is generally measured at a specific height, an adjustment is made in the value of wind speed at stack tip by the following power law relationship (3-10) (Barratt, 2001).

$$u_s = u_f\left(\frac{h_s}{h_r}\right)^p \qquad (3\text{-}10)$$

Where u_s is hourly wind speed at stack height (m/s), u_f is hourly wind speed at reference height h_r (m/s), h_s is physical stack height (m), P is wind profile exponent. The profile exponent p is a function of stability which given in Table (3-5). The power law equation used to adjust wind speeds over a height range from about 10 to 300 m. the reference height is normally used as 10 m from the earth surface.

Table (3-5) wind profile exponent (p) as a function of atmospheric stability (Barratt, 2001)

Stability class	Urban areas	Rural Areas
A	0.10	0.07
B	0.15	0.07
C	0.20	0.10
D	0.25	0.15
E	0.30	0.35
F	0.30	0.55

3.3.3 Stack Tip Downwash

Stack tip downwash can occur when the ratio of the stack exit velocity to wind speed is less than 1.5. In this case, low pressure in the wake of the stack may cause the plume to be drawn downward behind the stack. Pollutant dispersion is reduced when this occurs and can lead to elevated pollutant concentrations immediately downwind of the source. The distance at which plume downwashes below the stack obtained from Equation (3-11) (Hanna et al., 1982).

$$h_s' = h_s + 2d_s\left[\frac{V_s}{u_s} - 1.5\right] \quad (3\text{-}11)$$

Where, V_s is stack gas exit velocity, u_s is wind velocity at stack height, h_s is physical stack height, h_s' is corrected stack height for stack downwash, d_s is stack diameter. We can note that, the maximum downwash correction is 3 stack diameters.

3.3.4 Plume Rise

A plume emitted from a stack may rise, fall, or stay roughly at the same height depending on the exit velocity of the plume, diameter of the stack source, stack gas temperature, ambient air temperature, and atmospheric stability. Very often, the exhaust gases from chimneys are hotter than the environment or they have substantial momentum. This makes them rise and hence the release height (He) that should be used in the Gaussian plume equation does not correspond truly to the physical stack height (hs). Instead, it corresponds to the stack height plus the plume rise distance Δh, which is the approximate height above the stack before the plume turns 90^o to follow the wind. Many individuals have studied plume rise over years. The most common plume rise formulas are those developed by Briggs, which have been extensively validated with stack plume observations (Briggs, 1969). The height of the plume is approximated by determining firstly whether buoyancy or momentum forces dominate the motion of the plume after exiting the stack source. If the temperature of the gas is less than the ambient temperature, momentum forces are assumed to dominate. If the temperature of the gas is greater than the ambient temperature buoyancy forces are assumed to dominate.

3.3.4.1 Plume Rise Dominated by Buoyancy

Buoyancy plume rise formulas are used on plumes with temperatures greater than the ambient air temperature. For unstable or neutral atmospheric conditions A, B, C, D, the downwind distance of final plume rise x_f can be calculated using Equations (3-12) (Beychok, 2005) according to the amount of buoyancy force. Then

the plume rise distance Δh under these conditions is estimated from Equation (3-13) (Briggs, 1969).

$$x_f = \begin{cases} 119\ F_b{}^{0.4} & \text{for } F_b \geq 55\ m^4 s^{-3} \\ 49\ F_b{}^{0.625} & \text{for } F_b < 55\ m^4 s^{-3} \end{cases} \quad (3\text{-}12)$$

$$\Delta h = \frac{1.6 F_b{}^{1/3} x_f{}^{2/3}}{u_s} \quad (3\text{-}13)$$

In case of the down distance x is smaller than x_f, we used x instead of x_f in Equation (3-13). The buoyancy flux F_b is calculated by Equation (3-14) (EPA; 1977).

$$F_b = g v_s D^2 \frac{(T_s - T_a)}{4T_s} \quad (3\text{-}14)$$

Where Vs is stack exit velocity in m/s; D is the top inside stack diameter in m, Ts is stack gas temperature in ^{0}K, Ta is air temperature in ^{0}K and g is the gravity force in m/s^2. In case of stable atmospheric stability E and F, the downwind distance of final plume rise x_f, and the plume rise Δh are calculated using the formulas from Equations (3-15) & (3-16) (Beychok, 2005).

When $x_f \leq 1.84\ u\ s^{-0.5}$

$$\Delta h = \begin{cases} 1.6\ F_b{}^{1/3}\ x^{2/3}\ u^{-1} & \text{for } x < x_f \\ 1.6\ F_b{}^{1/3}\ x_f{}^{2/3}\ u^{-1} & \text{for } x > x_f \end{cases} \quad (3\text{-}15)$$

When $x_f > 1.84\ u\ s^{-0.5}$

$$\Delta h = \begin{cases} 1.6\ F_b{}^{1/3}\ x^{2/3}\ u^{-1} & \text{for } x < 1.84\ u\ s^{-0.5} \\ 2.4\ (F_b/u\ s)^{1/3} & \text{for } x \geq 1.84\ u\ s^{-0.5} \end{cases} \quad (3\text{-}16)$$

Where s is stability parameter defined by Equation (3-17), and x_f calculated from Equations (3-12) or (3-13). DALR in Equation (3-18) is the dry adiabatic laps rate which equal to 1 ^{0}K/100 m height, and $\frac{\Delta\Theta}{\Delta T}$ is the potential temperature gradient. If $\left(\frac{\Delta\Theta}{\Delta T}\right)$ is not given, we can use, 0.02 ^{0}K/100 m for E stability and 0.035 ^{0}K/100 m for F stability (Schnelle & Dey, 2000).

$$s = \frac{g}{T_a}\left(\frac{\Delta\Theta}{\Delta T}\right) \quad (3\text{-}17)$$

$$\left(\frac{\Delta\Theta}{\Delta T}\right) = \frac{dT}{dz} + DALR \quad (3\text{-}18)$$

3.3.4.2 Plume Rise by Momentum Dominated

When stack gas temperature is greater than the ambient air temperature, it must be determined whether the plume rise is buoyancy dominated or momentum dominated. For this purpose a crossover temperature ΔT_c is calculated from Equations (3-19). When $\Delta T = T_s - T_a$ is less than the crossover temperature, the plume is momentum dominated and the following equations must be used. For momentum dominated plumes, unstable or neutral conditions A, B, C, and D, the form of the equation of crossover temperature difference ΔT_c is determined by the value of the buoyancy flux parameter F_b. For plumes dominated by momentum in unstable and neutral conditions, the plume rise is calculated from Equation (3-20) (EPA; 1992).

$$\Delta T_c = \begin{cases} 0.0297 T_s \frac{v_s^{1/3}}{d_s^{2/3}} & F_b < 55 \\ 0.00575 T_s \frac{v_s^{2/3}}{d_s^{1/3}} & F_b \geq 55 \end{cases} \quad (3\text{-}19)$$

$$\Delta h = 3 d_s v_s u^{-1} \quad (3\text{-}20)$$

For momentum dominated plumes, stable conditions E and F, the form of the equation for ΔT_c is determined by the value of the stability parameter s. The crossover temperature is calculated by Equation (3-21). In this case; the plume rise is related to the momentum flux parameter Equation (3-22) and the plume rise calculated using equation (3-23).

$$\Delta T_c = 0.019582 T_s v_s s^{1/2} \quad (3\text{-}21)$$

$$F_m = \frac{v_s^2 d_s^2}{4} \frac{T_a}{T_s} \quad (3\text{-}22)$$

$$\Delta h = 1.5 \left(\frac{F_m}{u}\right)^{1/3} s^{-1/6} \quad (3\text{-}23)$$

The final plume height (H_e) is the sum of calculated plume height (Δh) and the physical height of the stack (h_s).

3.3.5 Effect of Complex Terrain on Plume Height

Complex terrain is defined as terrain whose elevation exceeds the release height of the source being modeled. The model assumes that the plume is deflected vertically as it is transported over elevated terrain and that this vertical displacement can be simply described as a function of plume height (H_e), terrain height (h_t), and stability class. The adjusted plume height due to the terrain effect is presented using maney models as given by Equation (3-24) to Equation (3-27) (Lott, 1984; Lott, 86).

$$H^1 = \begin{cases} H_e - \frac{h_t}{1-R} & \text{for } H_e > h_t \\ H_e R & \text{for } H_e \le h_t \end{cases} \quad (3\text{-}24)$$

$$H^2 = \begin{cases} H_e\left(1 - \left(\frac{h_t}{H_e}\right)(1-R)\right) & \text{for } H_e > h_t \\ H_e R & \text{for } H_e \le h_t \end{cases} \quad (3\text{-}25)$$

$$H^3 = \begin{cases} H_e\left[1 - \left(\frac{h_t}{H_e}\right)\left[1 - \frac{R}{[1+R(H_e/h_t-1)]}\right]\right] & \text{for } H_e > h_t \\ H_e R & \text{for } H_e \le h_t \end{cases} \quad (3\text{-}26)$$

$$H^4 = \begin{cases} H_e - h_t - \frac{h_t^3}{H_e^3}(1-C_t) & \text{for } H_e > h_t \\ H_e(1-C_t) & \text{for } H_e \le h_t \end{cases} \quad (3\text{-}27)$$

Where C_t = 0.4 for stability classes A-E and C_t=0.7 for stability class F. The value of R is also a function of stability class and is presented in Table (3-6) (Lott, 1984). The following models handles terrain adjustment as indicated in Figure (3-7) and Equations (3-28) & (3-29) (EPA, 1985).

Table (3-6) Value of variable R as a function of stability classes (Lott, 1984)

Stability class	A	B	C	D	E	F
R	0.8	0.7	0.6	0.5	0.4	0.3

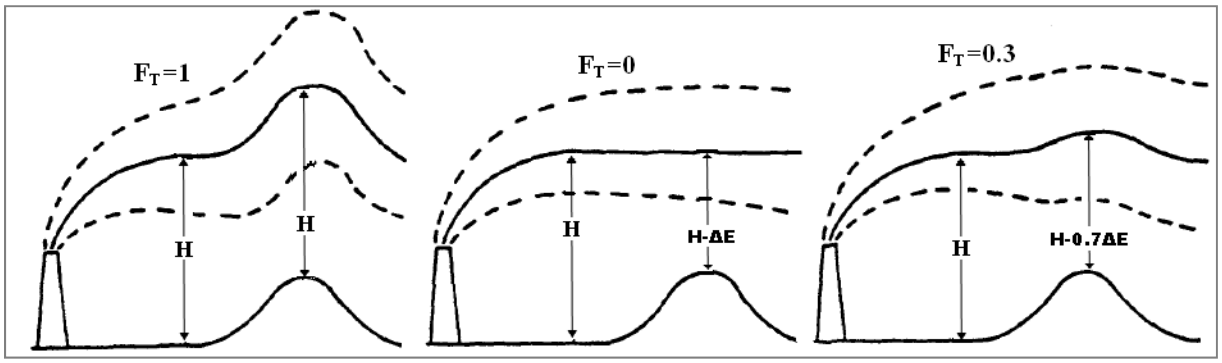

Figure (3-7) Deflection of plume rise due to terrain effect (EPA, 1985)

$$H^5 = H_e - (1 - F_T)\Delta E \quad (3\text{-}28)$$

$$H^6 = H_e + (Z_s - Z_r) \quad (3\text{-}29)$$

Whre $\Delta E = Z_r - Z_s$, Z_r is the receptor height, Z_s is the elevation base of source, and F_T is the terrain adjustment factor. For unstable to netural conditions (A, B, C, D), F_T is set to 0.5 and 0.25 for stable conditions flow (E and F). Due to the terrain effect, a modified plume height (H_e) is substituted for the effective stack height (H) .

3.3.6 Mixing Height at Different Atmospheric Stabilities

The planetary boundary layer is defined as the layer of the lower atmosphere whose characteristics are directly influenced by the ground surface (Barrat, 2001). In the atmosphere, turbulent mixing forms and maintains this layer; hence, the planetary boundary layer is also a mixing layer. Mixing Height or Mixing Layer is used by meteorologists to quantify the vertical height of mixing in the atmosphere. Transport and diffusion of pollutants is highly dependent on the mixing height values (Coulter, 1979). Pollutants are mixed nearly uniformly throughout this layer by turbulence. Turbulent mixing can be either convective or mechanically produced. During the day-time, turbulent mixing is formed and maintained predominantly from strong surface heating, whereas during the night-time, primarily the mechanical regime dominates the mixing layer (Schnelle & Dey, 2000). Thus mixing height of the atmosphere can be defined as that layer where vigorous mixing takes place due to thermal and mechanical turbulence. In the atmosphere, thermal turbulence dominates in an unstable layer and mechanical turbulence usually exists in a neutral layer, but turbulence is suppressed within a stable layer. Therefore, mixing of pollutants is greatest within an unstable layer and least in a stable layer. Mixing height could be estimated by practical methods or/and modeling methods. It is determined practically by profile observations of temperature and wind speed.

There are many methods of temperature/wind profile observations such as radiosonde, SODAR, RASS, and LIDAR (Coulter, 1979). A radiosonde is a small box-instrument that is carried by a balloon. During its travelling upward in the atmosphere, it measures pressure, altitude, temperature, relative humidity, and wind (both wind speed and its direction). Radiosonde transmits the measured meteorological parameters to a fixed station on the ground. SODAR (Sonic Detection and Ranging), is a meteorological instrument also known as a wind profile which measures the scattering of sound waves by atmospheric turbulence. SODAR systems are used to measure wind speed at various heights above the ground. A radio acoustic sounding system (RASS) is a system for observing the temperature profile upward of the atmosphere using backscattering of radio waves. LIDAR (Light Detection And Ranging) is an optical remote sensing technology that measures properties of scattered light. From backscattered intensity and the travel time, detailed information on aerosols and clouds, water vapour, atmospheric trace gases as well as wind speed and wind direction can be directly obtained with high spatial and temporal resolution. The practical method to estimate the mixing height is not available at the study area. The other possibility is parameterizations or using simple models with only few measured parameters as input. Many studies (Yu, 1978; Benkley & Schulman, 1979; Coulter, 1979; Arya, 1981; Hanna & Chang, 1992; Khan & Simpson, 1997; Fatogoma & Jacko, 2002) used simple models to estimate the height of mixing layer. The proposed model to estimate mixing height at unstable conditions (stability A, B and C) is suggested as given by Equation (3-30) (Giovannoni, 1993). Benkley & Schulman, 1979 suggested Equation (3-31) to calculate the mechanical mixing height at neutral conditions which presented also in (Arya, 1981). The top of the stable mixing height is defined as the height at which turbulence disappears and above which shear stress and sensible heat become negligible. For stable atmospheric conditions (atmospheric stability E and F), Arya, 1981 proposed the relationship (3-32) also the formula is given by Giovannoni, 1993.

$$H_m = -kL\left(\frac{\omega_*}{U_*}\right)^3 \quad (3\text{-}30)$$

$$H_m = 0.185\frac{U_*}{f} \quad (3\text{-}31)$$

$$H_m = 113 + 0.34\left(\frac{LU_*}{f}\right)^{0.5} \quad (3\text{-}32)$$

Where H_m is the mixing height, K is Von Karman's constant, L is the Monin-Obukhov length, U_* is the friction velocity, f is the Coriolis factor, and ω_* is the

convective velocity scale. The Coriolis factor f is defined by $f = 2\omega \sin\phi$, where ω is the rate of earth rotation and ϕ is the latitude of the location (Schnelle & Dey, 2000).

3.3.6.1 Friction Velocity and Monin-Obukhov Length

Monin-Obukhov length is a parameter with dimension of length that gives a relation between parameters characterizing dynamic, thermal, and buoyant processes of the atmosphere. The surface friction velocity and the Monin-Obukhov length (L) can be determined using an iteration procedure. This method is based on the knowledge of sensible heat flux, H, an observation of the wind speed U (m/s) at a height Z, and the standard wind speed profile as given in Equation (3-33) (Hanna and Chang, 1993).

$$U = \frac{U_*}{k}\left(\ln\frac{(Z-d)}{Z_0} - \Psi\left(\frac{Z}{L}\right)\right) \quad (3\text{-}33)$$

Where Ψ is universal dimensionless function; Z_0 is the surface roughness length and d is the displacement length ($d \cong 5\,Z_0$). For the case of purely mechanical turbulence or neutral stability the solution of Equation (3-38) gives Equation (3-34) (Schnelle & Dey, 2000).

$$U = \frac{U_*}{k}\left(\ln\frac{(Z-d)}{Z_0}\right) \quad (3\text{-}34)$$

Because Ψ is a function Z/L and L is a function of U_* , a simple analytical solution of U_* is possible for stable conditions when $\Psi(Z/L) = -4.7 * Z/L$, while the following formula has been developed (3-35) (Hanna & Chang, 1992).

$$U_* = \frac{0.2U}{\ln(Z-d)/Z_0}\left[1 + \left(1 - 4\left(\frac{4.7gZ\theta_* \ln((Z-d)/Z_0)}{0.4TU^2}\right)^{1/2}\right)\right] \quad (3\text{-}35)$$

Where T is absolute temperature, g is acceleration due to gravity and θ_* is the scaling temperature. The scaling temperature θ_* can be estimated using Holtslag and Van Ulden's (1983) empirical Equation (3-36).

$$\theta_{*1} = 0.09(1 - 0.5N^2) \quad (3\text{-}36)$$

Where N is the fractional cloud cover and θ_{*1} has units of Kelvin. In order to find the real solution to the past equation, Weil & Brower (1983) set the following limit to θ_{*1} in Equation (3-37).

$$\theta_{*2} = \frac{0.4TU^2}{18.8gZln((Z-d)/Z_0)} \quad (3\text{-}37)$$

The correct value of θ_* is selected from the smaller estimated values of θ_{*1} and θ_{*2}. Also, there is an upper limit of 0.05 mK/s to the product of $U_*\theta_*$. The function $\Psi(Z/L)$ is very complicate during unstable conditions. To estimate the friction velocity at unstable conditions, Hanna & Chang (1992) proposed the following analytical solution Equation (3-38).

$$U_* = \frac{0.4U}{\ln[(Z-d)/Z_0]}[1 + d_1 \ln(1 + d_2 d_3)] \quad (3\text{-}38)$$

Where

$$d_1 = \begin{cases} 0.128 + 0.005\ln(Z_0/(Z-d)), & \text{if } (Z_0/(Z-d)) \le 0.01 \\ 0.107, & \text{if } (Z_0/(Z-d)) > 0.01 \end{cases} \quad (3\text{-}39)$$

$$d_2 = 1.95 + 32.6(Z_0/(Z-d))^{0.45} \quad (3\text{-}40)$$

$$d_3 = \frac{H_s}{\rho C_p}\frac{0.4g(Z-d)}{T}\left(\frac{\ln((Z-d)/Z_0}{0.4U}\right)^3 \quad (3\text{-}41)$$

Where H_s is the sensible heat flux, ρ is the air density C_p is the specific heat of dry air at constant pressure and the term $d_1 \ln(1 + d_2 d_3)$ represents the correction due to instability. Once the friction velocity is determined, the Monin–Obukhov length (L) is estimated using from Equation (3-42) (Golder, 1972).

$$L = -\frac{\rho C_p T {U_*}^3}{kgH_s} \quad (3\text{-}42)$$

Where L is in meters, P is the atmospheric pressure in millibar, U_* is the friction velocity in m/s, and H_s is the sensible heat flux in W/m^2. In case of unstable conditions the Monin-Obkhuv length is negative value. Table (3-7) presents the range of the Monin-Obkhuv length values according to the atmospheric stability.

Table (3-7) Values of Monin-Obukhov length L with respect to atmospheric stability

L	Range of Monin-Obukhov	Stability
Small negative	-100 m < L < 0	Very unstable
Large negative	-105 m≤ L ≤ -100 m	Unstable
Very large(positive or negative)	|L| >105 m	Neutral
Large positive	10 m ≤ L ≤105 m	Stable
Small positive	0 < L < 10 m	Very stable

3.3.6.2 Sensible Heat and Convective Velocity Scale

Holtslag & van Ulden (1983) suggested Equation (3-43) to calculate the net surface radiation.

$$Q^* = \frac{(1-r)S_I + c_1 T^6 - \sigma T^4 + c_2 N}{1+c_3} \quad (3\text{-}43)$$

Where r, c_1, c_2, c_3 are empirical constants, S_I is the measured incoming solar radiation, and T is the absolute temperature, r is Albedo which describes the effects of the surface on the net incoming solar radiation. The surface sensible heat flux calculated as presented in Equation (3-44).

$$H_s = \frac{(1-\alpha)+(\gamma/s)}{1+(\gamma/s)}(Q^* - c_G Q^*) - \beta \quad (3\text{-}44)$$

Where, $c_G = 0.1$ is the ratio between soil heat flux and net radiation, $\alpha = 1.2$ and $\beta = 20\ Wm^{-2}$ are empirical parameters of surface moisture, which are estimated for a grass-covered surface in Netherland. The ratios γ/s and $\frac{(\gamma/s)}{1+(\gamma/s)}$ are tabulated by Holtslag and Van Ulden, 1983 as a function of surface temperature, Table (3-8). Venkatram (1978) suggested a simple formula (3-45) to calculate the convective velocity scale.

$$\omega_* = 4.74\ Q_m^{1/2} \quad (3\text{-}45)$$

Where, $Q_m = \frac{Q_0}{\rho.cp}$ is the kinematic heat surface flux (m s^{-1} K), $Q_o = A_g S_I$ is the sensible heat flux W/m^2 and S_I is the measured incoming solar radiation. The constant A_g is a function of ground cover, and it varies from 0.25 for a crop canopy to 0.55 for a dry surface (Venkatram, 1986).

3.3.7 Deposition Velocity

Particulate matters are brought to the ground surface through the combined processes of turbulent diffusion and gravitational settling. Near the surface, small particles may be removed from the atmosphere and deposited on the ground. The process of removing particles from the atmosphere to the surface by non-precipitation is defined as dry deposition (Sehmel, 1980). Many models of dry deposition express the deposition velocity as the inverse of a sum of resistances plus gravitational settling velocity terms (Atkinson et al., 1997; Pai et al., 1997). The resistances represent the opposition to transport of the deposited particles from a

reference height through the turbulent atmospheric surface layer, and through a quasi-laminar layer just above the surface to the surface itself.

Table (3-8) Ratios of $\gamma/_s$ and $\frac{(\gamma/_s)}{1+(\gamma/_s)}$ as a function of surface temperature (Holtslag & van Ulden 1983)

T ^{0}C	$\gamma/_s$	$\frac{(\gamma/_s)}{1+(\gamma/_s)}$
-5	2.01	0.67
0	1.44	0.59
5	1.06	0.51
10	0.79	0.44
15	0.6	0.38
20	0.45	0.31
25	0.35	0.26
30	0.27	0.21
35	0.21	0.17

Over smooth surfaces, a thin non-turbulent sublayer develops that can be a significant obstacle to the transfer of the pollutant onto the surface. Small particles (< 0.05 μm diameter) are transported through the quasi-laminar layer primarily by Brownian diffusion. However, Brownian diffusion becomes less efficient as the particle size increases. Particles in the 1-20 μm diameter range tend to penetrate the quasi-laminar layer by inertial impaction. Gravitational settling velocity has dominate effect on particle diameter larger than 20 μm. The predicted deposition velocity is close to the gravitational settling velocity for large particles (e. g., greater than 20 μm diameter), and decreases with decreasing particle size to about 0.1-1.0 μm, where it reaches a minimum. The deposition velocity then increases with decreasing particle size for smaller sized particles. This behavior is consistent with the importance of Brownian motion in enhancing deposition rates for very small particles (EPA, 1994). The general approach used in the resistance methods is to include explicit parameterizations of the effects of Brownian motion, inertial impaction, and gravitational settling. The deposition velocity is written as the inverse of sum of resistances to pollutant transfer through various layers, plus gravitational settling velocity as presented in Equation (3-46) (Kumar et al., 2008).

$$V_d = (r_a + r_d + r_a r_d v_t)^{-1} + v_t \quad (3\text{-}46)$$

Where, V_d is the deposition velocity (cm/s), v_t is the gravitational settling velocity (cm/s), r_a is the aerodynamic resistance (s/cm), and r_d is the deposition layer resistance (s/cm). For large settling velocities, the deposition velocity

approaches the gravitational settling velocity, whereas for small settling velocities, V_d tends to be dominated by $r_a$and r_d resistance terms. The lowest few meters of the atmosphere can be divided into two layers: a fully turbulent region where vertical fluxes are nearly constant, and the thin quasi-laminar sublayer. The resistance to transport through turbulent, constant flux layer is the aerodynamic resistance r_a is given in Equation (3-47) (Xu & Carmichael, 1998).

$$r_a = \frac{1}{k\,U_*}\left[\ln\left(\frac{z}{z_0}\right) - \psi_H\right] \qquad (3\text{-}47)$$

Where, ψ_H is a stability adjustment factor which given by Equation (3-48), U_* is the friction velocity (cm/s), K is the von Karman constant (0.4), z is the reference height, m (10 m), and z_0 is the effective level at which the horizontal wind speed approaches zero, commonly known as surface roughness length as given in Table (3-9) (Voldner et al. 1985). The approach used to parameterize the deposition layer resistance term is given in Equation (3-49) (Atkinson et al., 1997).

$$\psi_H = \begin{cases} -5\frac{z}{L} & \text{stable conditions} \\ 0 & \text{neutral conditions} \\ 2\ln\left(\frac{1+\sqrt{1-16\,z/L}}{2}\right) & \text{unstable conditions} \end{cases} \qquad (3\text{-}48)$$

Table (3-9) surface roughness z_0(cm) for each surface type (Voldner et al., 1985)

Surface type	Winter	Spring	Summer	Fall
Coniferous forest	90	90	90	90
Deciduous forest	90	90	90	90
Cultivated land	0.02	0.7	1	1
Grassland	0.02	0.7	2	2
Urban	100	100	100	100
Snow/ice	0.02	—	—	—
Deserts	0.0005	0.0005	0.0005	0.0005

$$r_d = \left[Sc^{-\frac{2}{3}} + 10^{-\frac{3}{St}}\right]^{-1} U_*^{-1} \qquad (3\text{-}49)$$

Where Sc is the Schmidt number ($Sc = v/D$) (dimensionless), v is the viscosity of the air (0.157 cm^2/s), D is the Brownian diffusivity (cm^2/s), St is the Stokes number $St = \left(\frac{v_t}{g}\right)\left(\frac{u_*^2}{v}\right)$ (dimensionless), and v_t, is the settling velocity for small particles. The first term of Equation (3-49) involving the Schmidt number, parameterizes the effects of Brownian motion. This term controls the deposition rate for small particles. The second term, involving the Stocks number, is a measure of

the importance of inertial impaction, which tends to determine for intermediate-size particles in the 2-20 μm diameter size range. The gravitational settling velocity is calculated using Formula (3-50) (EPA, 1994).

$$v_t = \frac{\rho g\, d_p^2\, c_2}{18\,\mu}\, S_{cf} \qquad (3\text{-}50)$$

Where, ρ is the particle density (g/cm^3), d_p is the particle diameter (μm), μ is the absolute viscosity of air (= 1.81 x 10^{-4} g/cm/s), c_2 is air units conversion constant (1 x 10^{-8} cm^2/μm^2), and S_{cf} is the slip correction factor for small particles, which is computed using Equation (3-51) (Atkinson et al., 1997).

$$S_{cf} = 1 + \frac{2x_2\left(a_1 + a_2\, e^{-\left(\frac{a_3 d_p}{x_2}\right)}\right)}{10^{-4} d_p} \qquad (3\text{-}51)$$

Where, $x_2, a_1, a_2, a_3,$ are constants with values of 6.5×10^{-6}, 1.257, 0.4 and 0.55×10^{-4}, respectively. The Brownian diffusivity of the pollutant (in cm^2/s) is computed from the Relationship (3-52) (Atkinson et al., 1997).

$$D = 8.09 \times 10^{-10}\left[\frac{T S_{cf}}{d_p}\right] \qquad (3\text{-}52)$$

The particle size distribution plays an important role in the dry deposition velocity. A minimum values is reached for particles of about 0.5-1 μm diameter (EPA, 1994). The determination of the V_d values for particles is still an open question, even more difficult than for gases. Values commonly vary over two orders of magnitude, such as from 0.01 to 2.00 cm/s. The size distribution, the surface of the canopy layer, the roughness height z_0 and the friction velocity U_*, directly affect the particle deposition (Sehmel, 1980)

Chapter (4) Results and Discussion of Geostatistical Analysis

In Chapter (4), the raw data of soil samples were analyzed to examine the normality of each metal. Also in this chapter, geostatistical methods were applied (1) to improve the predicted values of soil contaminations by selecting new sites of soil samples; (2) to analyze the spatial autocorrelation of soil heavy metals; (3) to generate the continuous distribution of each soil pollutants (i.e. predicted maps), (4) to compare between the predicted values after and before taking the new soil samples, (5) to investigate areas which intensively contaminated by heavy metals, and (6) to examine the effect of 2D and 3D dimensions among samples on the predicted values.

4.1 Selecting New Sites of Soil Samples

Predicted values of soil heavy metals at unsampled locations are created using Geostatistical Analyst extension of ArcGIS. Ordinary Kriging was used to calculate these prediction concentrations within Goslar County. No prediction is certain and every estimated value has error (Fraczek & Byttnerowicz, 2007). The Standard Prediction Error (SPE) shows a distribution of square root of Kriging variance. Values of SPE were created using the same kriging method and parameters that were used to generate the prediction maps. Figure (4-1) presents the SPE for Pb, Zn, As, Cd and Cu. It is important to analyze prediction errors to understand the reliability of the results. Improving reliability of geostatistical prediction maps is possible by selecting more samples at locations where reliability is the lowest. The bright yellow colors in Figure (4-1) indicate areas where the SPE of the predicted values is low. While dark brown was used to indicate high value of SPE. We note that the dark brown colors are existed in areas that have few numbers of samples. The south area of Goslar County is empty from soil samples especially for As and Hg soil heavy metals except concentrated samples around St. Andreasberg. Also the soil samples in the north borders of the study area have few numbers for all variables. SPE maps present high value of uncertainly in these locations. The soil samples in St. Andreasberg are used to predict the concentrations south sites of the city, which gives a poor prediction accuracy because the lack of samples. Therefore selecting more samples within these regions is required to improve the predicted values. The selection of most new sample sites will be in the north-borders and south regions of the study area. Selection new sites of soil samples could be done manually; alternatively a GIS automated model can be used to determine them. Part of the ArcGIS framework is the Model-Builder which provides a graphic environment for creating, running, and saving models. A simple ArcGIS model is built to select new soil samples, illustrated

in Figure (4-2). The model depends on geostatistical layers of SPE and forest regions which are the interesting locations in this study. In the generated model, SPE layers classified (using Reclassify of GIS Spatial Analyst Tool) to ten levels, with maximum value taken as ten. Then the Weighted-Overlay Tool used to mark the classes from one to eight as NODATA, so that only the selected new samples are within the classes 9 and 10 which are the highest SPE. Also the selected new samples are restricted to be in forest regions. The results of the model are 9 new locations for Pb, 4 new samples for Zn, and 6 soil samples for Cd within the north borders as given in Figure (4-1). In south area, the selected soil samples are 7 locations for Hg and 5 new samples for As. Other soil samples were selected to study dispersion modeling of heavy metal contaminations emitted from smelter stacks. Chimneys of these smelters had emitted harmful gases and heavy metals which affected soil in the forest areas up to several km distances. Based on dispersion modeling studies, the other 19 soil samples were selected according to the following criteria. (1) Different distances from the industrial smelters. (2) Within main wind direction from smelters. (3) Hill facing side to the smelters. (4) Existing visibility to the smelters. (5) Near to the roads in the area. The selected soil samples based on dispersion modeling is illustrated in Figure (4-1, f). The total selected soil samples are 50 new locations presented in Figure (4-1, g) (Rabeiy et al., 2010).

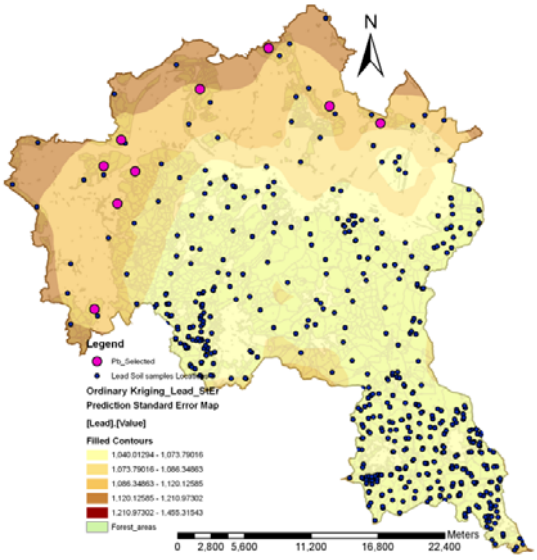

Figure (4-1, a) SPE of Pb and its selected new sites of soil samples

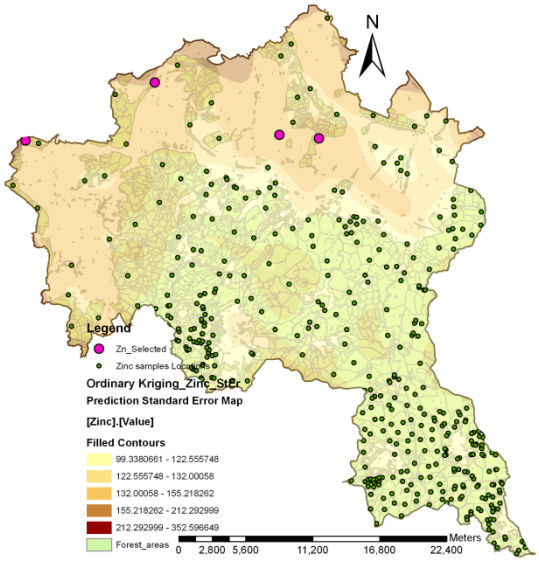

Figure (4-1, b) SPE of Zn and its selected new sites of soil samples

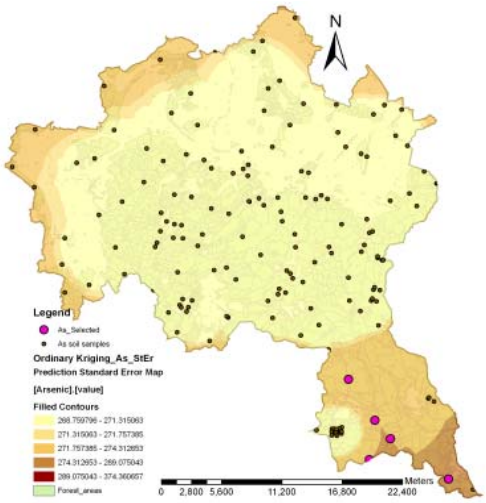

Figure (4-1, c) SPE of As and its selected new sites of soil samples

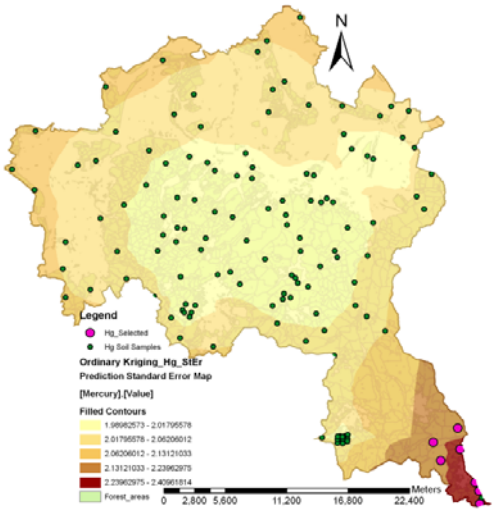

Figure (4-1, d) SPE of Hg and its selected new sites of soil samples

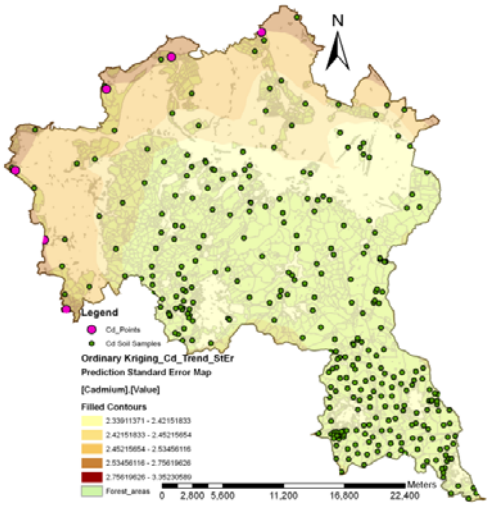

Figure (4-1, e) SPE of Cd and its selected new sites soil samples

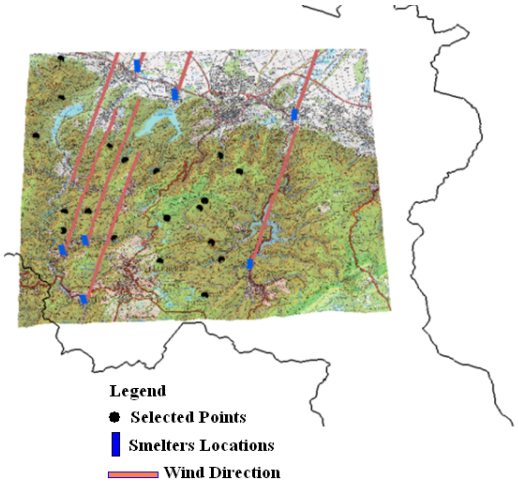

Figure (4-1, f) sites of new soil samples selected based on dispersion modeling

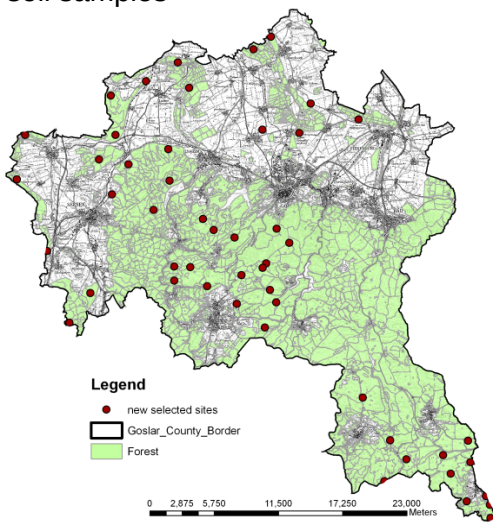

Figure (4-1, g) locations of the selected new 50 soil samples within forest areas in Goslar county

Figure (4-1) Standard Prediction Errors of soil heavy metals and locations of new soil samples

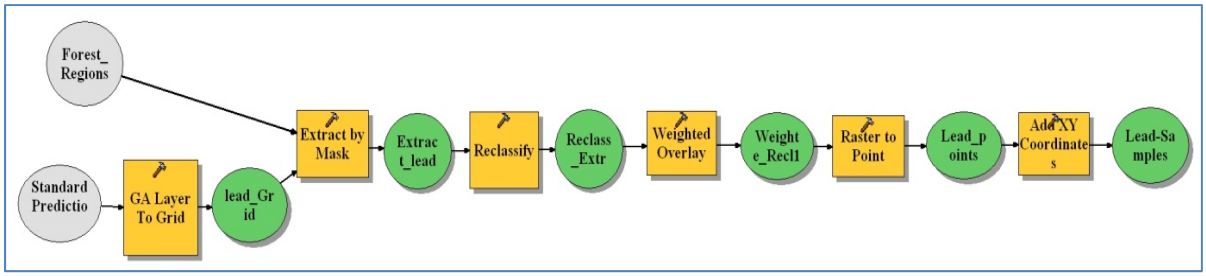

Figure (4-2) Automated ArcGIS model to select new locations of soil samples

4.2 Data Analysis and Transformation

The new 50 soil samples selected in the previous section were taken and analyzed for each soil heavy metal and the results are added to the total soil samples. Data statistics is examined for each heavy metal in the data sets. Summary of the statistics gives useful information about the raw data sets, such as minimum value, maximum value, mean, skewness and kurtosis among others. Skewness and kurtosis characterize the degree of symmetry of a distribution around its mean and give information about the normality of a variable. Because the effect of the mining and smelter activities on the area, the soil heavy metals are usually positive skewed. Histograms of raw data sets were generated as indicated in Figure (4-3). Also, summary of kurtosis and skewness is presented in Table (4-1). It is shown from the figure and the table that kurtosis and skewness for all the metals are higher than that of the normal distribution and all the samples are positively skewed. Therefore transformation is applied for the raw data sets to get distribution closer to the normality before generating geostatistical prediction. Table (4-1) presents comparison between skewness and kurtosis of the data sets before and after the transformation. Lognormal transformation is applied to Pb, Zn, Hg, Cd and Cu soil heavy metals. While this transformation is not enough to get the normality for As and Sb, so Box-Cox power transformation is found to be suitable for these variables. Figure (4-3) also indicates the new histograms of the transformed data sets.

Table (4-1) Type of transformation of the raw data sets

Metal	Raw Data		Log transformation		Box-Cox transformation	
	Skewness	kurtosis	Skewness	Kurtosis	Skewness	kurtosis
Pb	5.69	46.72	0.14	3.24	-	-
Zn	5.01	32.67	-0.13	4.24	-	-
As	5.13	32.57	1.60	6.09	-0.01	2.49
Hg	3.73	23.09	0.18	2.67	-	-
Cd	5.47	46.28	0.42	2.69	-	-
Sb	3.02	12.34	1.38	3.89	0.86	2.32
Cu	3.15	19.49	-0.32	3.82	-	-

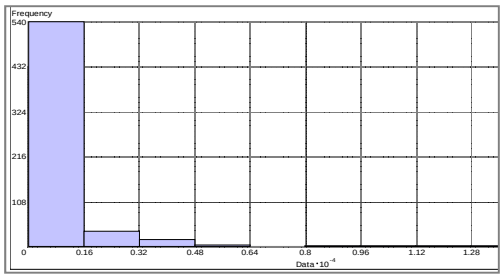

Figure (4-3, a1) Histogram of Pb raw data

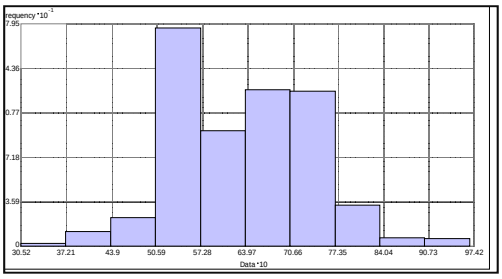

Figure (4-3, a2) Histogram of Pb Log-Transformation

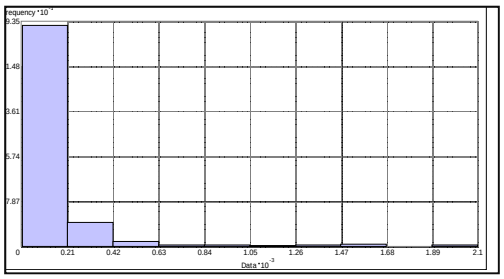

Figure (4-3, b1) Histogram of Zn Raw data

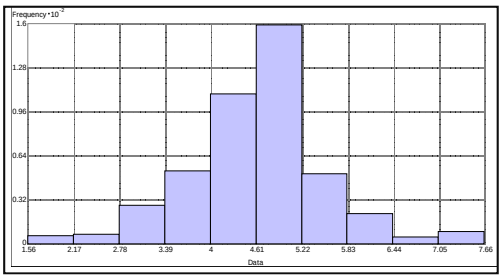

Figure (4-3, b2) Histogram of Zn Log-Transformation

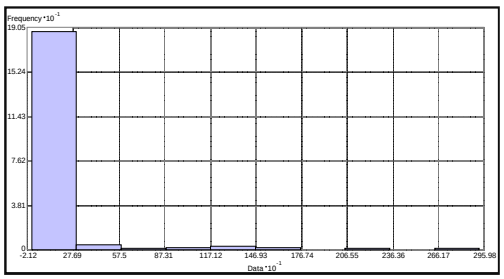

Figure (4-3, c1) Histogram of As raw data

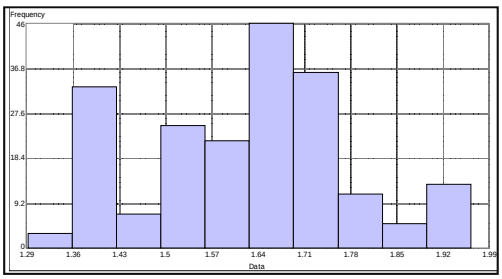

Figure (4-3, c2) Histogram of As Box-Cox transformation

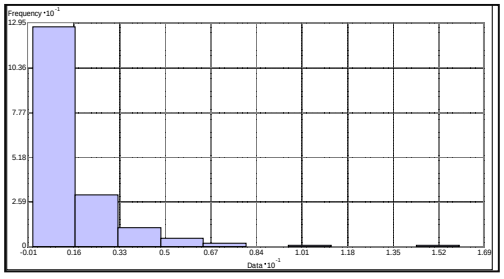

Figure (4-3, d1) Histogram of Hg raw data

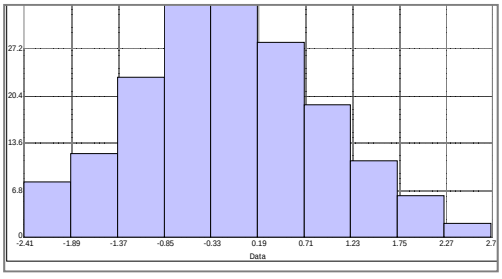

Figure (4-3, d2) Histogram of Hg Log-Transformation

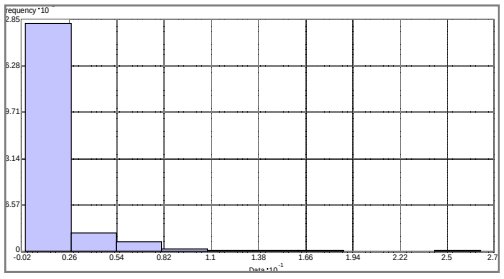

Figure (4-3, e1) Histogram of Cd raw data

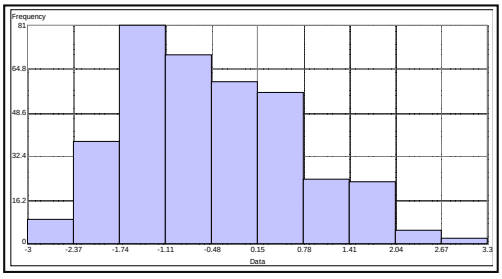

Figure (4-3, e2) Histogram of Cd log Transformation

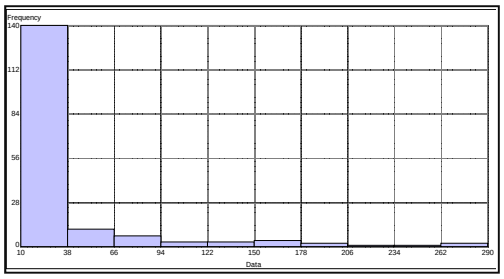

Figure (4-3, f1) Histogram of Sb raw data

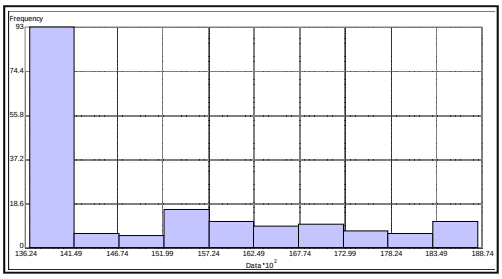

Figure (4-3, f2) Histogram of Sb Box-Cox Transformation

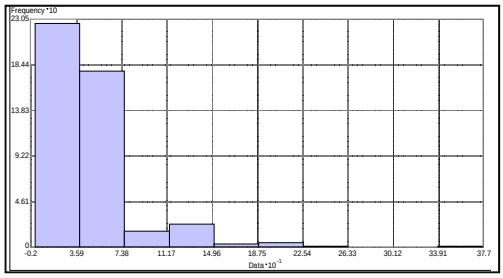

Figure (4-3, g1) Histogram of Cu raw data

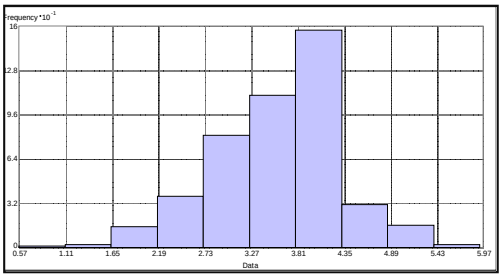

Figure (4-3, g2) Histogram of Cu Log-transformation

Figure (4-3) Histogram of the data sets before and after transformation (*Horizontal axis is the value of heavy metal, vertical axis gives the frequency*)

4.3 Results of Geostatistical Analysis

Geostatistical computations were performed using Geostatistical Analysis extension of ArcGIS package. The best fitted mathematical models to the experimental semivariograms were applied to predict the spatial correlation of Pb, Zn, As, Hg, Cd, Sb and Cu soil heavy metals. The parameters of the semivariogram models are summarized in Table (4-2). These data were generated from spherical and Gaussian models which were the best fitting descriptor of the data set as illustrated in Figure (4-4). Soil heavy metals Pb, Zn, Cd and Cu were fitted by Gaussian model, while As, Hg, Sb were fitted by Spherical model. Calculating the semivariogram in different directions proved that all the studied soil heavy metals exhibited geometrical anisotropy properties except Pb. All the heavy metal variables presented a nugget variance and sill. The nugget variance (C_0) is the value of semivariogram at a lag distance equal to zero. The sill (C) is the maximum variance at which the semivariogram model flattened or takes the horizontal shape. The distance at which the spherical semivariogram reaches to the sill is called the range (a). The range gives the correlation distance of the soil heavy metals. After this distance there is no relation between the variable. The correlation distances resulted from modeling the semivariogram range from 13.56 km for Zn and 24.29 km for Sb.

Table (4-2) Results of the best fitted semivariogram models for soil heavy metals

Metal	fitted Model	Major Range*,(km)	Minor Range, km	Direction	C_0	C	$(C_0/C)\%$	Meas. Er., %
Pb	Gaussian	22.26	-		0.416	1.406	29.577	98
Zn	Gaussian	13.56	12.25	46	0.345	1.003	34.352	47
As	Spherical	19.14	16.91	265	0.002	0.027	9.340	0
Hg	Spherical	21.48	20.07	53	0.420	1.155	36.315	60
Cd	Gaussian	19.14	17.48	295	0.568	1.393	40.743	92
Sb	Spherical	24.29	16.38	55	0.549	0.807	68.059	0
Cu	Gaussian	15.95	12.73	70	0.268	0.721	37.156	62

Meas. Er. %: Measurement error % from total nugget value

The Nugget/Sill (C_0/C) ratio can be regarded as a criterion to classify the spatial dependence of soil properties. If the ratio is less than 25%, the variable has strong spatial dependence; between 25% and 75%, the variable has moderate spatial dependence, and greater than 75%, the variable shows only weak spatial dependence (Liu, et al., 2006; Chang et al., 1998). From Table (4-2) it is found that, As marked strong spatial dependence with C_0/C ratio less than 10%. While Sb, has a relatively weak correlation with C_0/C ratio of 0.68%. The rest of soil heavy metals gave a moderate spatial dependence; ranges from 29.6% for Pb, to 37.2% for Cu. The Nugget variance refers to two sources, the experimental error and/or variations at scale too fine to detect (Microstructure). Because soil samples were taken along different years by different organizations that used many analysis methods, some locations have more than one measured value of the same metal. From these locations, soil samples were taken on different times and at different depths. Also different analysis methods were applied on these soil samples. Table (4-3) gives many values of Pb at the same point. The samples in this site are taken from three depths with average value of 2.5 cm, 7.5 cm and 12.5 cm respectively. For each depth we have three different values of Pb. These values are resulted from three different analysis methods. Geostatistical Analysis Extension of ArcGIS has the ability to calculate the error due to experimental work using Equation (2-5). By this quantity we can distinguish the nugget value to its source. Table (4-2) gives the percentage of measurement errors in the Nugget value. The nugget variance of soil heavy metals Pb and Cd refer approximately to the measurement errors. While Zn, Hg and Cu nearly 50 % of the nugget effect variances are caused by measurement errors. Because there are no coincident measurements for As and Sb, there is no opportunity to estimate the variance due to measurement errors, and the nugget variance for these variables refers to the variation in the microstructure. From previous discussions we can conclude that by reducing the measurement errors, nugget value will be reduced, hence the spatial dependency of the studied variables will be increased which will improve the predicted maps.

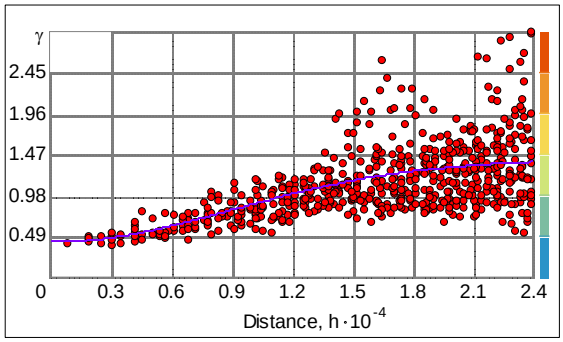

Figure (4-4, a) semivariogram model of Pb

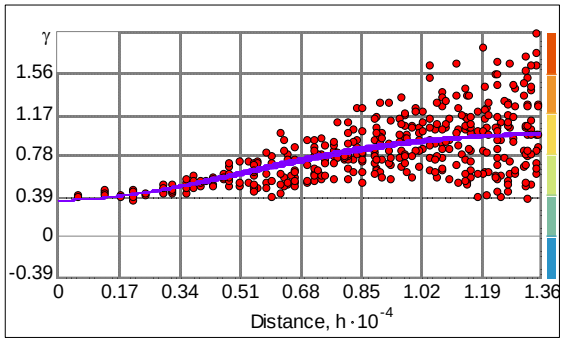

Figure (4-4, b) semivariogram model of Zn

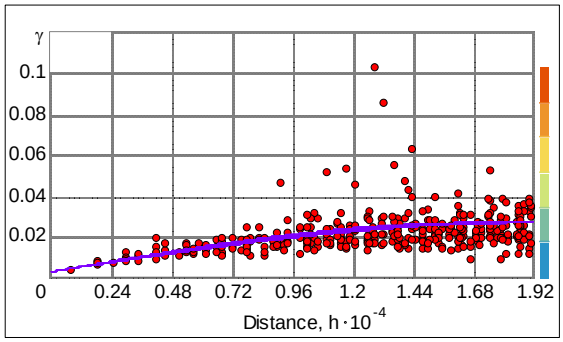

Figure (4-4, c) semivariogram model of As

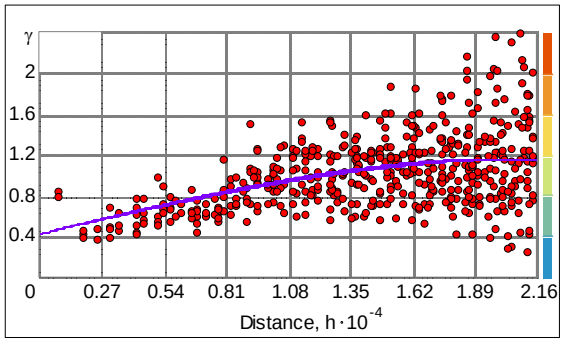

Figure (4-4, d) semivariogram model of Hg

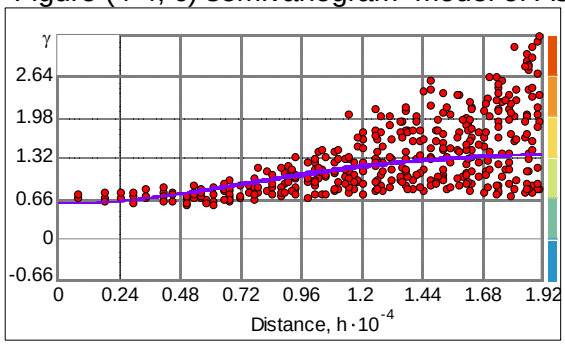

Figure (4-4, e) semivariogram model of Cd

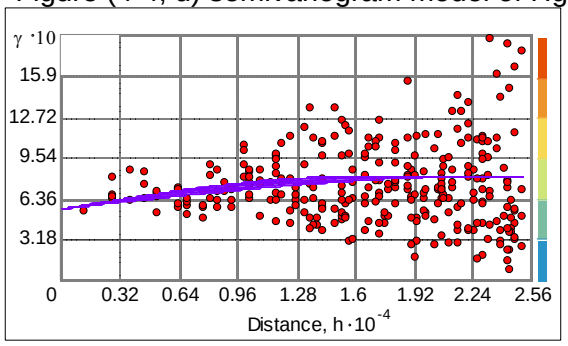

Figure (4-4, f) semivariogram model of Sb

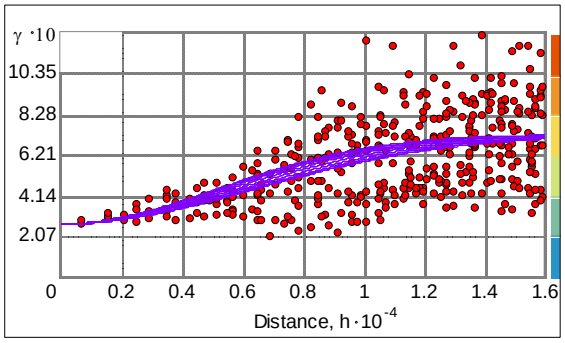

Figure (4-4, g) semivariogram model of Cu

Figure (4-4) Experimental semivariogram of soil heavy metals with their fitted models

Table (4-3) Different values for Pb in the same location along different depths

East, m	North, m	Min. depth, cm	Max. depth, cm	Average depth, cm	Analysis* Methods	Pb, mg/kg
3606211	5756886	0	5	2.5	KW	#Av-59
3606211	5756886	0	5	2.5	Salpetersäure	Av-40
3606211	5756886	0	5	2.5	HF	Av+100
3606211	5756886	5	10	7.5	KW	Av-49
3606211	5756886	5	10	7.5	Salpetersäure	Av-31
3606211	5756886	5	10	7.5	HF	Av+81
3606211	5756886	10	15	12.5	Salpetersäure	Av-27
3606211	5756886	10	15	12.5	KW	Av-16
3606211	5756886	10	15	12.5	HF	Av+45

#Av: average value at each depth, *KW (Königswasser, German): aqua regia, mixture of HCl, HNO3 and H2O2; Salpetersäure (German): Nitric acid (HNO3), also known as aqua fortis ; HF: Hydrofluoric acid (Jonušaitė, et al., 2004; Nomeda et al., 2007)

The fitted semivariograms are used to generate the predicted concentration maps of the studied soil heavy metals. Figure (4-5) illustrates the generated spatial distribution of soil heavy metals within Goslar County. The figure presents the anomaly of soil heavy metals as classes; with class number (1) resembles the minimum concentration. From this figure we can see that all heavy metals have distinct geographical distribution. The spatial distribution map of Pb shows high concentration in the middle area especially around Clausthal-Zellerfeld, Altenau and Lautenthal cities and in the south region around St. Andreasberg. For Zn the spatial distribution refers high concentration in the north east regions. The high concentration of As located only in small regions around Oker valley and St. Andreasberg city, in the vicinity of Samson mine. Mercury soil contamination has high values around Goslar, Oker and Clausthal-Zellerfeld locations. In these areas, there were the activities of smelters and old mines, especially Ramelsberg mine. Sb has small patches of high concentrations around St. Andreasberg, Lautenthal and Clausthal-Zellerfeld. Cadmium predicted map presents high concentration in the north-west region. While Cu heavy metal gives small area of high concentration around Oker city.

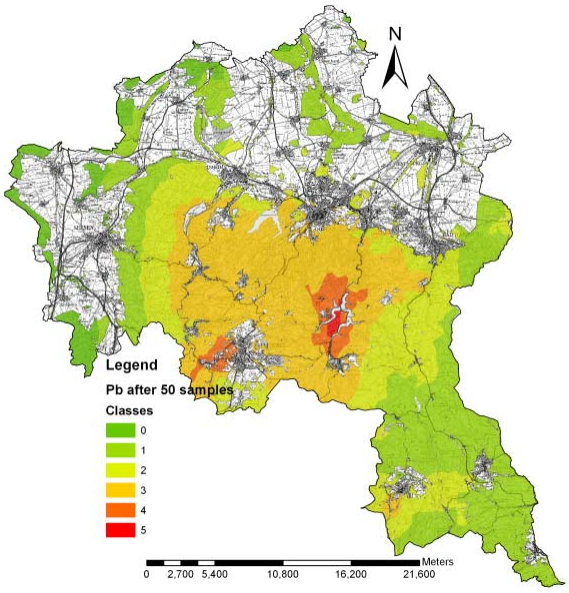

Figure (4-5, a) Predicted soil contamination map of Pb

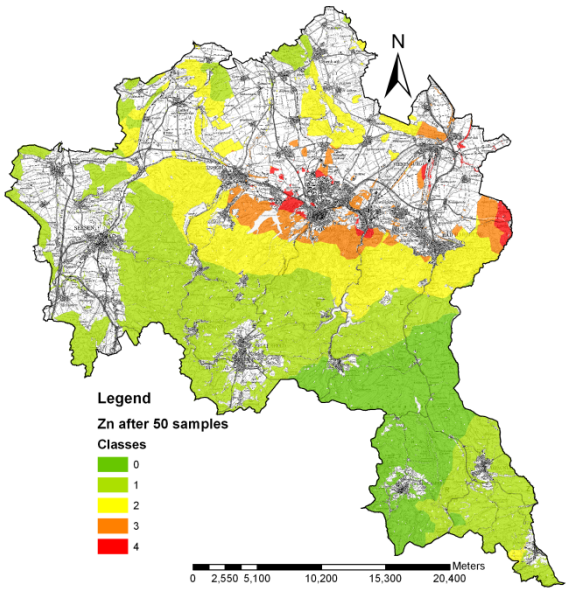

Figure (4-5, b) Predicted soil contamination map of Zn

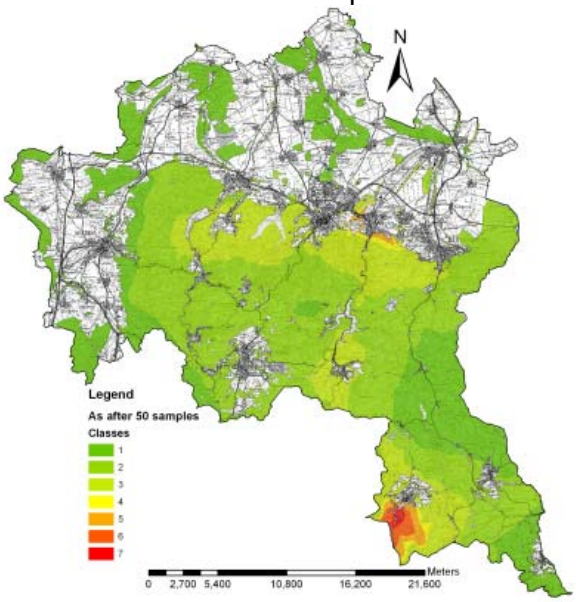

Figure (4-5, c) Predicted soil contamination map of As

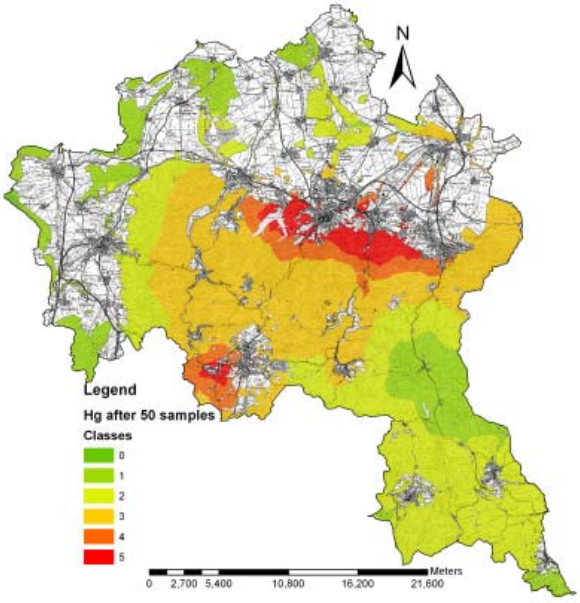

Figure (4-5, d) Predicted soil contamination map of Hg

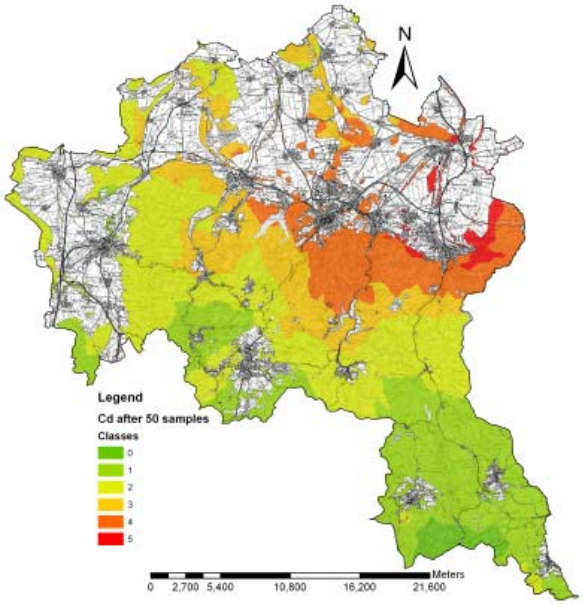

Figure (4-5, e) Predicted soil pollution map of Cd

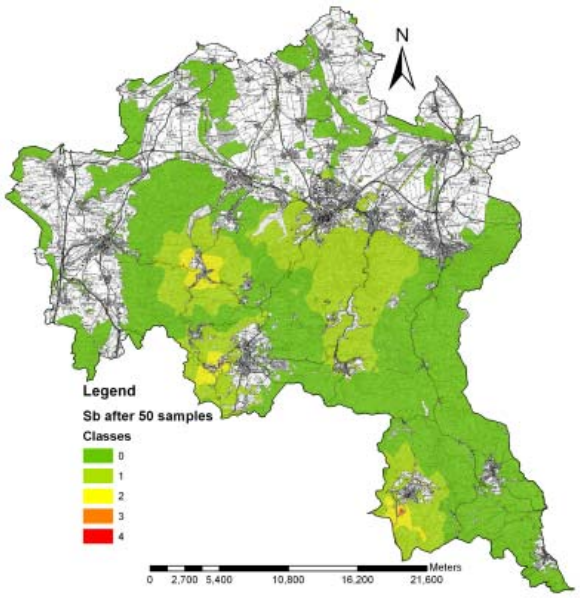

Figure (4-5, f) Predicted soil pollution map of Sb

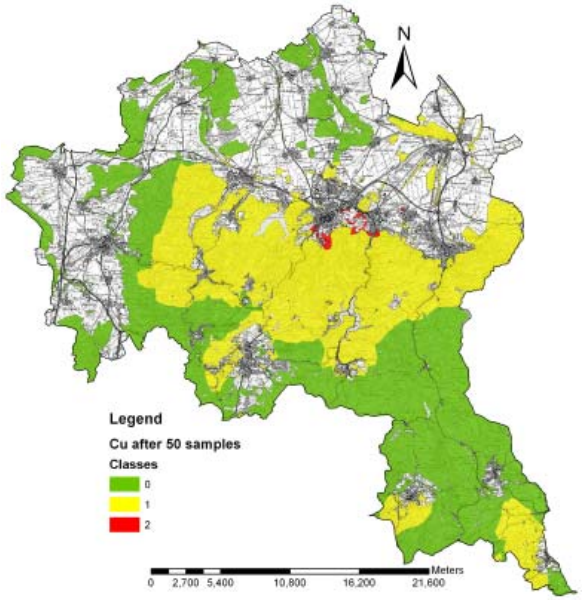

Figure (4-5, g) Predicted soil pollution map of Cu

Figure (4-5) Result of predicted concentration created by ordinary Kriging of different variables

To understand the relation between the different variables, the Pearson correlation coefficients of the raw data were calculated with its significance values as given in Table (4-4). Significance value of 0.1 indicates a 90% confidence. Strong positive correlations are observed between Zn & Cd; 89 % and Hg & Cu; 84 %. These correlations are recognized in Figure (4-5) of spatial distribution maps of these variables. Moderate correlation coefficients are found between many variables; e.g., Pb & Hg and Hg & Sb; of 60 % for the both. For As and Sb the correlation coefficient is 69 %.

Table (4-4) Correlation coefficient between soil heavy metals

Variable	Pb	Zn	As	Hg	Cd	Sb	Cu
Pb	1						
Zn	0.09* 0.0250§	1					
As	0.11 0.0751	-0.01 0.4347	1				
Hg	0.6 0.0000	0.44 0.0000	0.19 0.0049	1			
Cd	0.16 0.0009	0.89 0.0000	-0.01 0.4613	0.42 0.0000	1		
Sb	0.6 0.0000	0.01 0.4242	0.69 0.0000	0.41 0.0000	0.04 0.2937	1	
Cu	0.44 0.0000	0.47 0.0000	0.1 0.0902	0.84 0.0000	0.47 0.0000	0.46 0.0000	1

***: Correlation coefficient; §: Significance level**

4.4 Comparison between Measured and Predicted Values

The effect of 50 new soil samples on the final predicted maps is studied by comparing the predicted maps before and after sampling these locations. The predicted maps are generated for the studied soil heavy metals before and after these new samples. The two predicted maps for each soil heavy metal are created using the same geostatistical specifications (i.e., variogram parameters and search neighborhood). Analysis of the fitted semivariogram models is tabulated in Table (4-5) for each soil heavy metal before and after the new samples. Figures (4-6) to (4-12) give the difference between the two predicted maps for each variable with focusing on the difference between them. Predicted maps before and after taking the new 50 soil samples could also be compared using ArcGIS tools. The comparison is developed by calculating the difference between the predicted maps. The calculations are applied using 3D Analyst-Tools extension in ArcGIS after converting the geostatistical layers from vector to raster format. Figures (4-6) to (4-12) illustrate also the calculated deference of the predicted maps for before and after taking new soil samples. In this figure the green color refers to equal estimation, the white color presents underestimation while the red color gives overestimation. Equal estimation range is not more than 15% from the total estimated difference. For example, the percent of equal estimation from the total difference is 2%, 10%, and 15% for Hg, Pb, and Sb respectively. From this figure, we find that Pb, in the centre of the study area varies randomly from overestimation to underestimation and the effect of the new soil samples is not clear. For Zn, the two maps have equal estimation except a small area at the north of Goslar and Oker. In this location, there are only two soil samples available before selecting new samples. Therefore, taking new samples in this area increases the samples which uses to make prediction and improves the spatial distribution of Zn contamination.

For As, the effect of new samples is appeared around St. Andreasberg. Soil samples are concentrated within the city, and the effect of these points is extended to larger areas on the predicted map before taking new samples. By taking more samples around the city, we found that these new samples have less concentration than expected, which improved the final spatial distribution map of As. For Cd, the predicted maps before is overestimated in the north area of the Goslar County. While for Hg and Cu, the middle regions have large areas of overestimation but underestimated areas are found in the north for Hg. The same effect as for As is appeared again for the Sb soil heavy metal around St. Andreasberg city.

Table (4-5) Semivariogram models parameters for soil heavy metals before and after the new samples

Metal	Model	Major Range*,km	Minor Range, km	Direction	C_o	C	$(C_o/C)\%$	Meas. Er. %
Pb-B	Gaussian	22.27	-	-	0.44	1.372	32.070	100
Pb-A	Gaussian	22.26	-	-	0.416	1.406	29.577	98
Zn-B	Gaussian	13.56	12.16	31	0.325	1.074	30.261	54
Zn-A	Gaussian	13.56	12.25	46	0.345	1.003	34.352	47
As-B	Spherical	18.99	15.77	88	0.0022	0.028	7.801	0
As-A	Spherical	19.14	16.91	265	0.002	0.027	9.340	0
Hg-B	Spherical	21.48	19.1	55	0.498	1.113	44.744	51
Hg-A	Spherical	21.48	20.07	53	0.42	1.155	36.315	60
Cd-B	Gaussian	19.14	17.51	288	0.554	1.384	40.029	77
Cd-A	Gaussian	19.14	17.48	295	0.568	1.393	40.743	92
Sb-B	Spherical	24.27	17.43	65	0.557	0.949	58.693	0
Sb-A	Spherical	24.29	16.38	55	0.549	0.807	68.059	0
Cu-B	Gaussian	15.84	12.15	70	0.277	0.742	37.332	58
Cu-A	Gaussian	15.95	12.73	70	0.268	0.721	37.156	62

B: before the new samples; A: after new samples

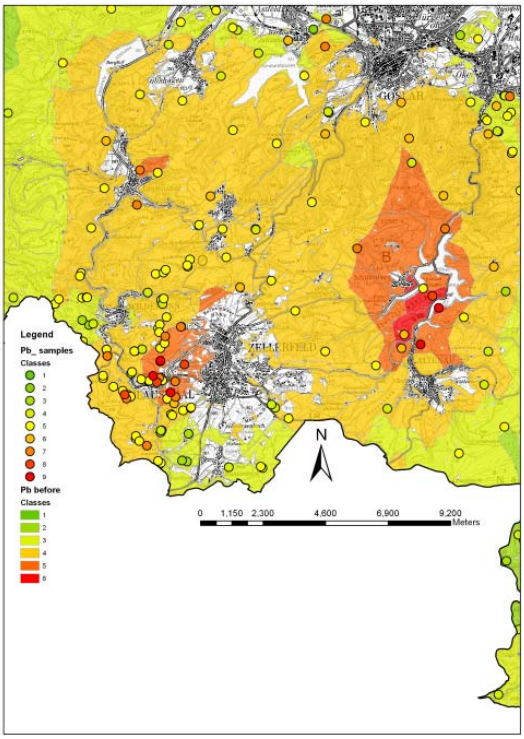

Figure (4-6, a) Predicted map of Pb before 50 soil samples

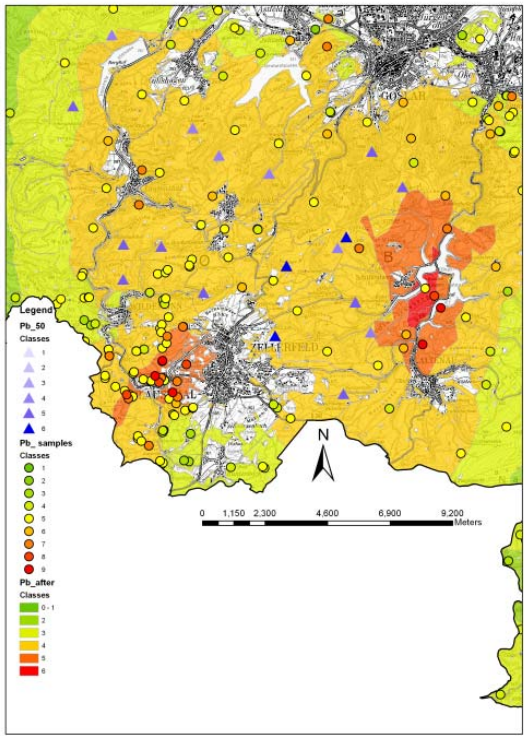

Figure (4-6, b) Predicted map of Pb after 50 new soil samples

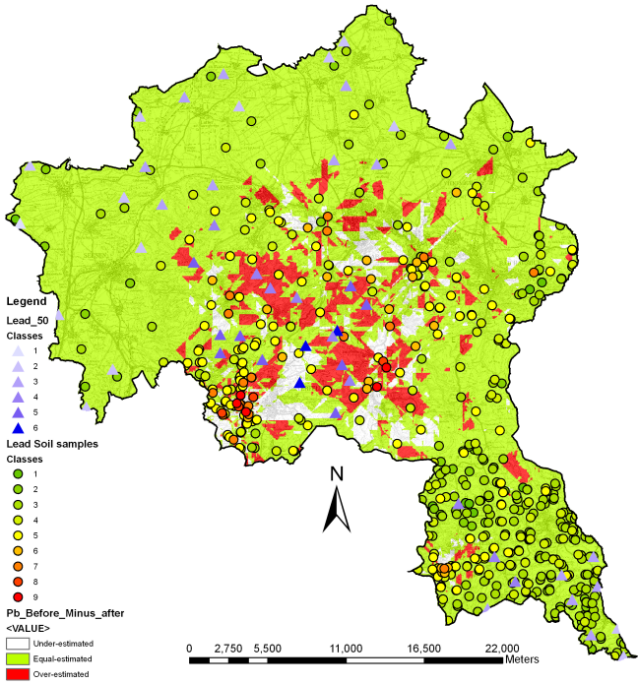

Figure (4-6, c) Predicted map of Pb before 50 minus predicted map of Pb after 50

Figure (4-6) Pb comparison between predicted maps before to after new soil samples

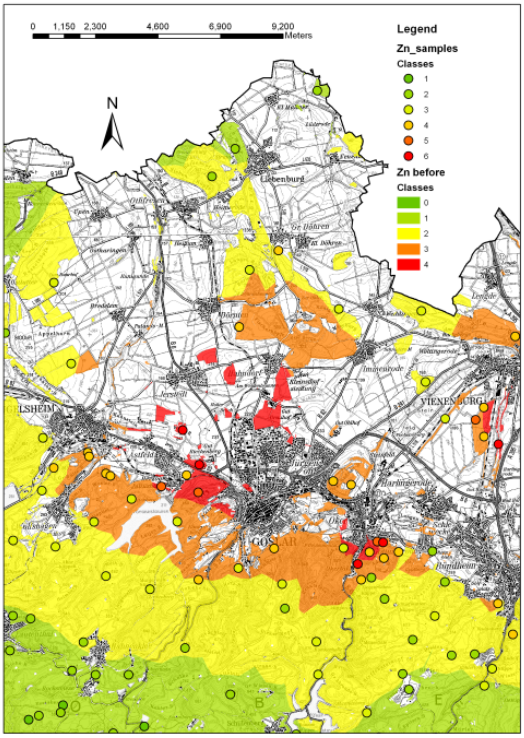

Figure (4-7, a) Predicted map of Zn before 50 soil samples

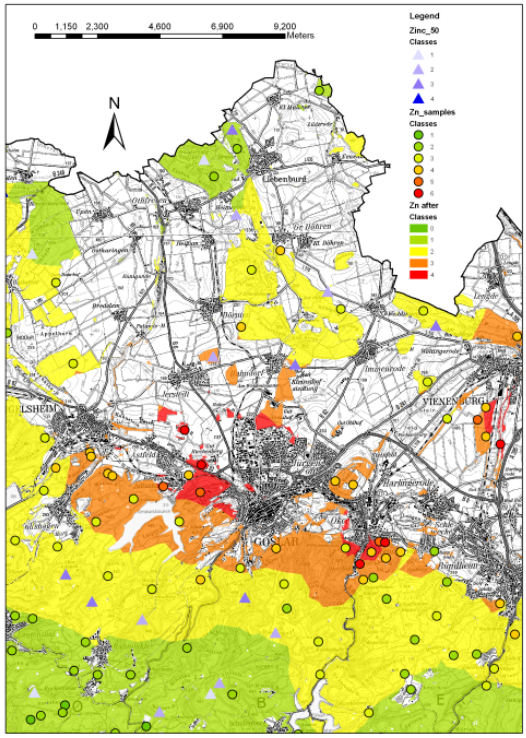

Figure (4-7, b) Predicted map of Zn after 50 new soil samples

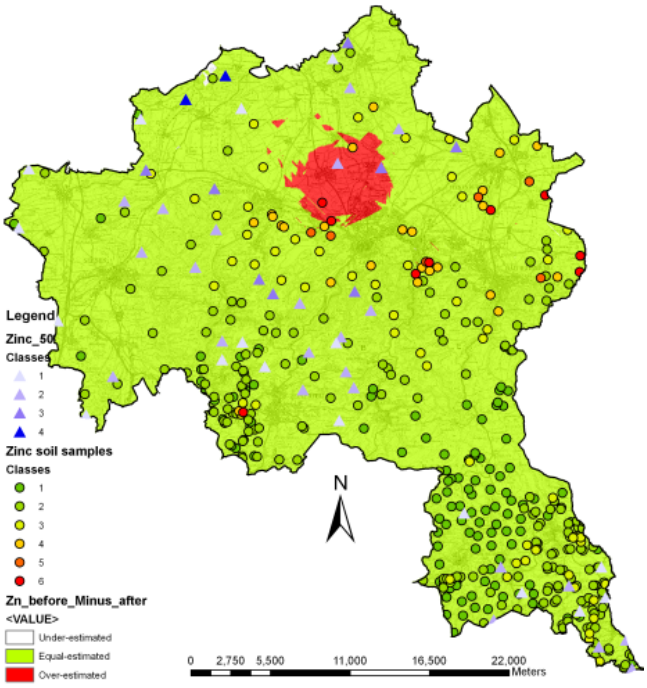

Figure (4-7, c) Predicted map of Zn before 50 minus predicted map of Zn after 50

Figure (4-7) Zn comparison between predicted maps before with after new soil samples

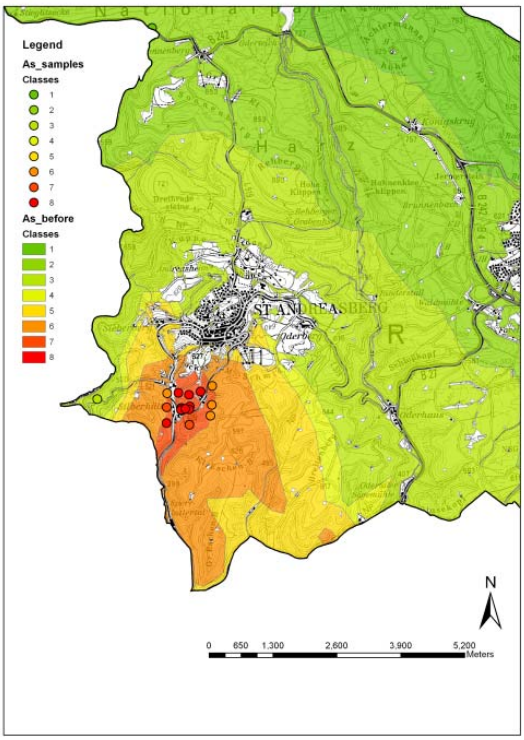

Figure (4-8, a) Predicted map of As before 50 soil samples

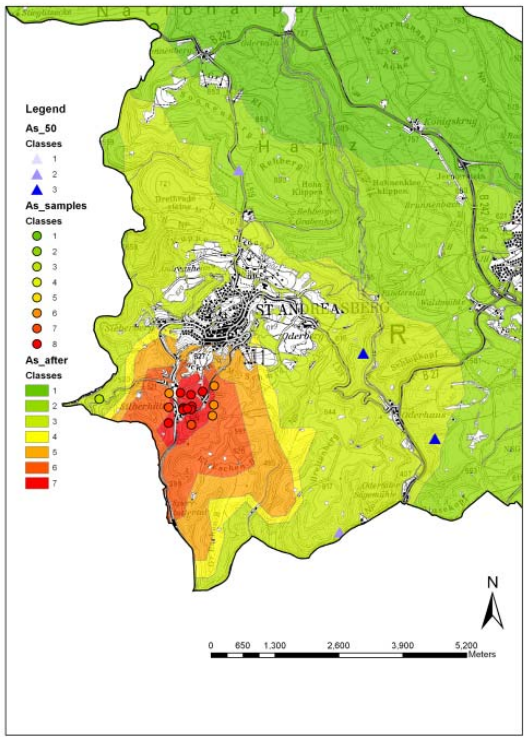

Figure (4-8, b) Predicted map of As after 50 new soil samples

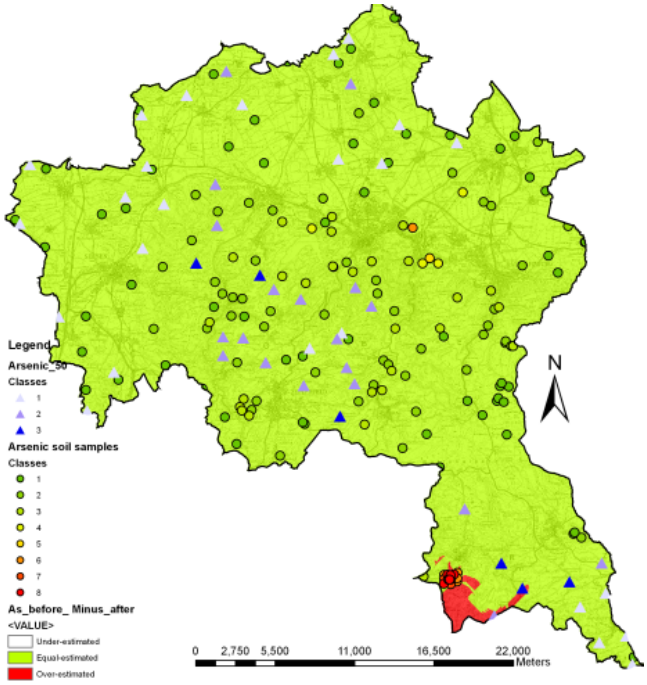

Figure (4-8, c) Predicted map of As before 50 minus predicted map of As after 50

Figure (4-8) As comparison between predicted maps before with after new soil samples

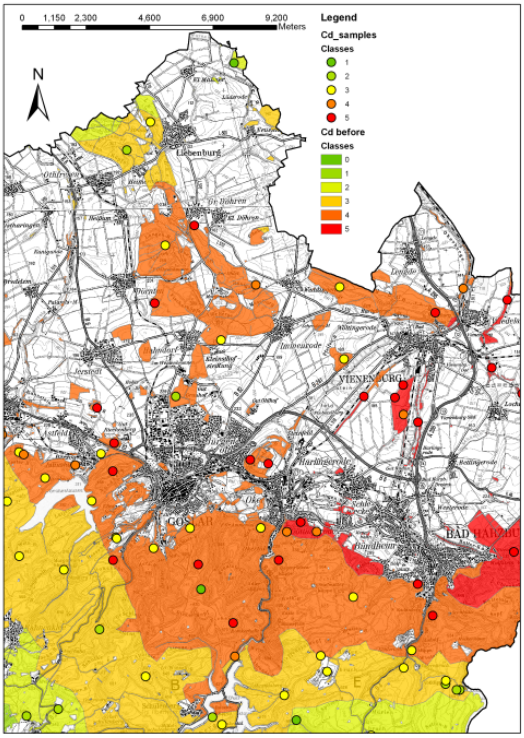

Figure (4-9, a) Predicted map of Cd before 50 soil samples

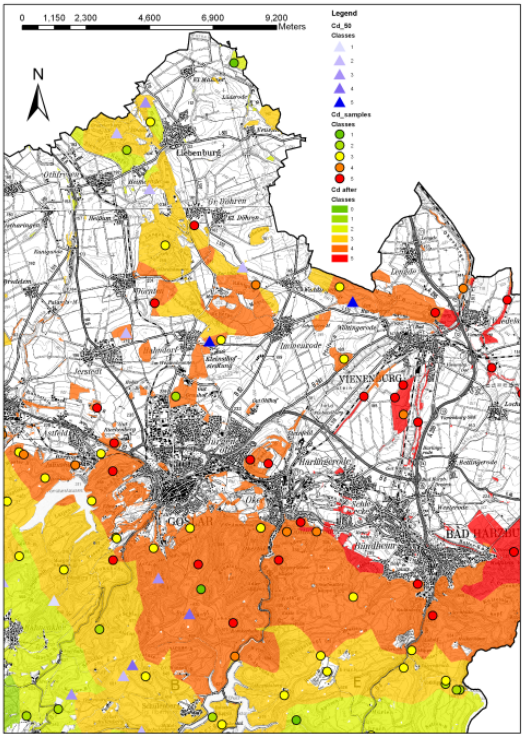

Figure (4-9, b) Predicted map of Cd after 50 new soil samples

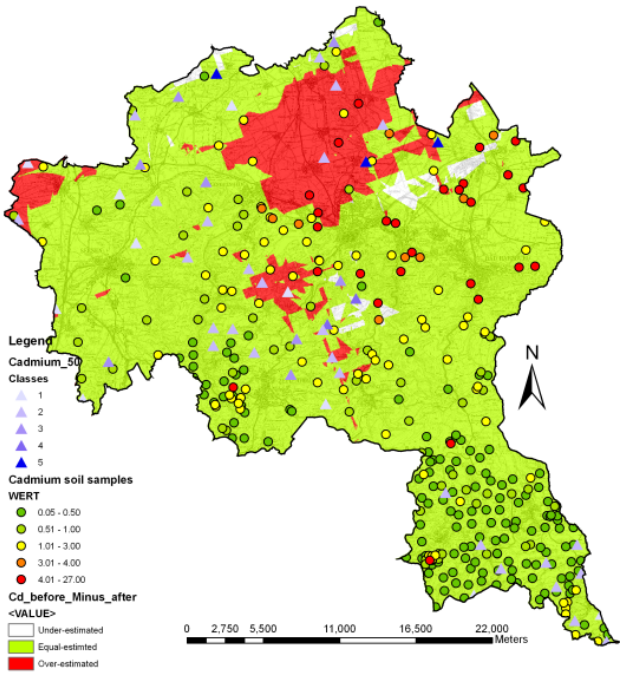

Figure (4-9, c) Predicted map of Cd before 50 minus predicted map of Cd after 50

Figure (4-9) Cd comparison between predicted maps before to after new soil samples

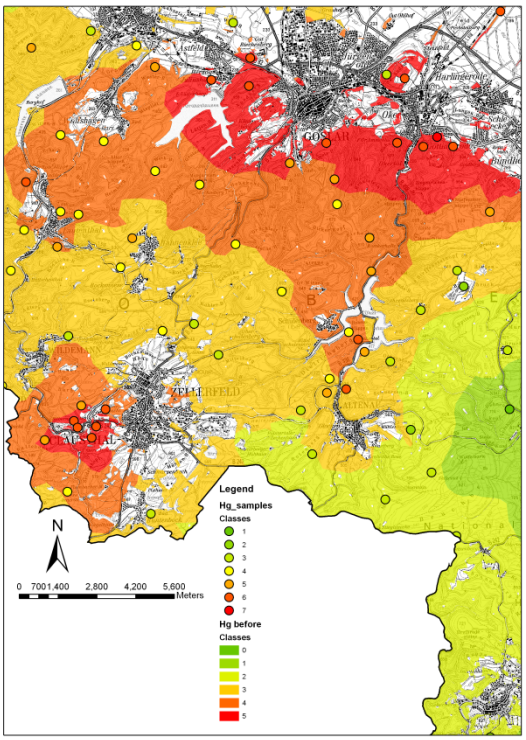

Figure (4-10, a) Predicted map of Hg before 50 soil samples

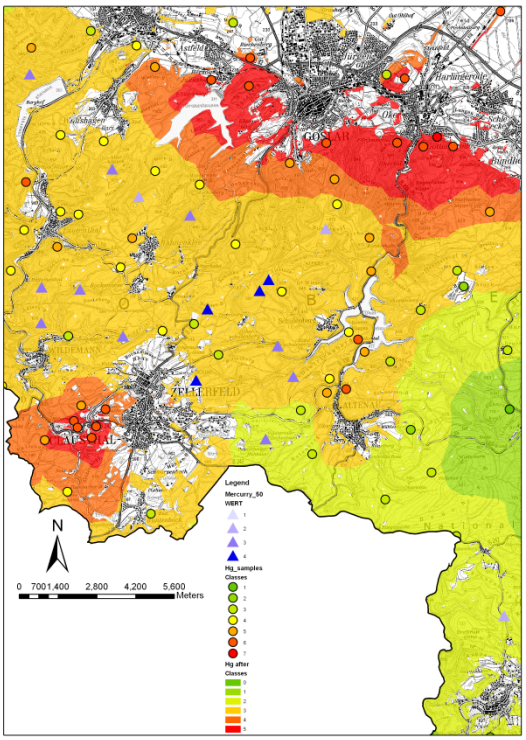

Figure (4-10, b) Predicted map of Hg after 50 new soil samples

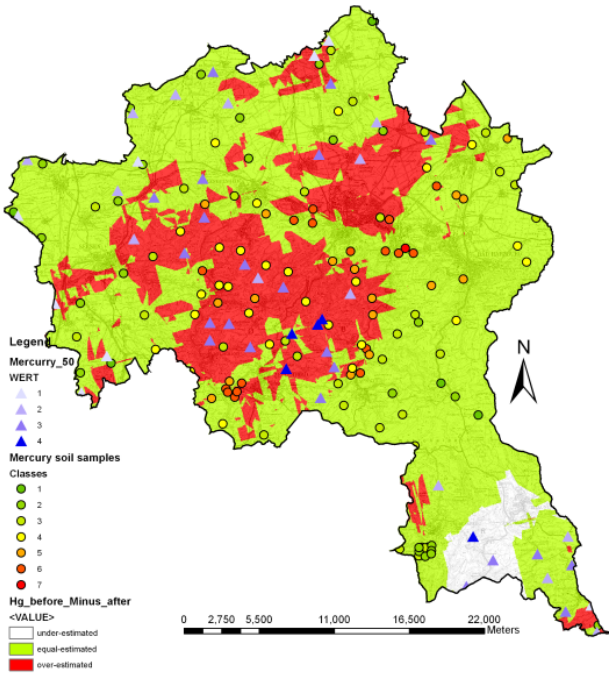

Figure (4-10, c) Predicted map of Hg before 50 minus predicted map of Hg after 50

Figure (4-10) Hg comparison between predicted maps before with after new soil samples

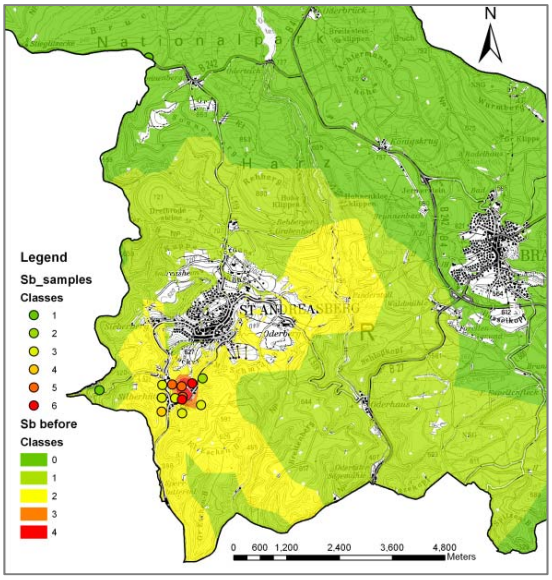

Figure (4-11, b) Predicted map of Sb before 50 soil samples

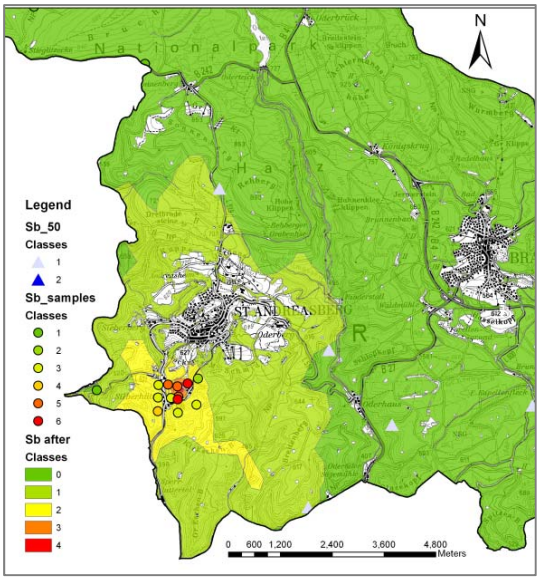

Figure (4-11, b) Predicted map of Sb after 50 new soil samples

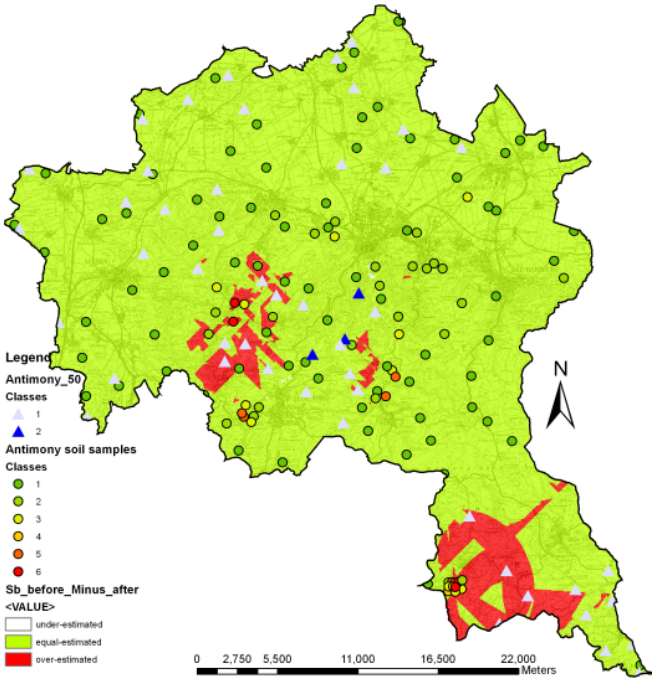

Figure (4-11, c) Predicted map of Sb before 50 minus predicted map of Sb after 50

Figure (4-11) Sb comparison between predicted maps before with after new soil samples

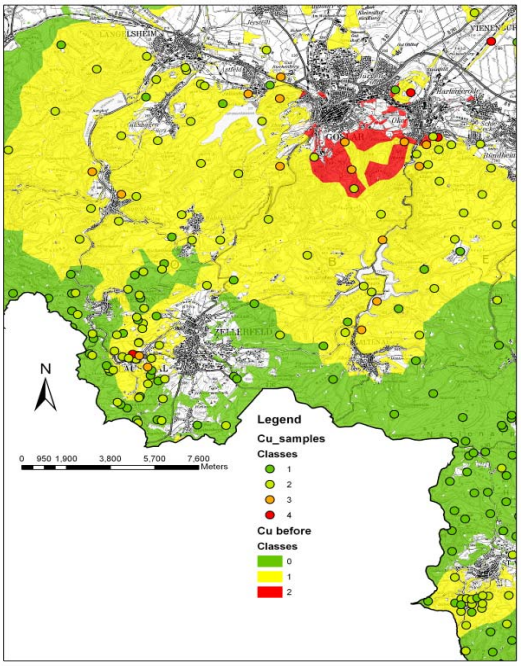

Figure (4-12, a) Predicted map of Cu before 50 new soil samples

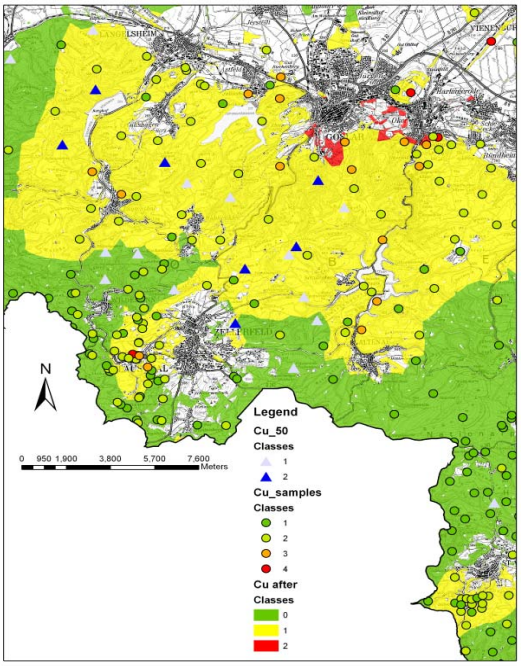

Figure (4-12, b) Predicted map of Cu after 50 new soil samples

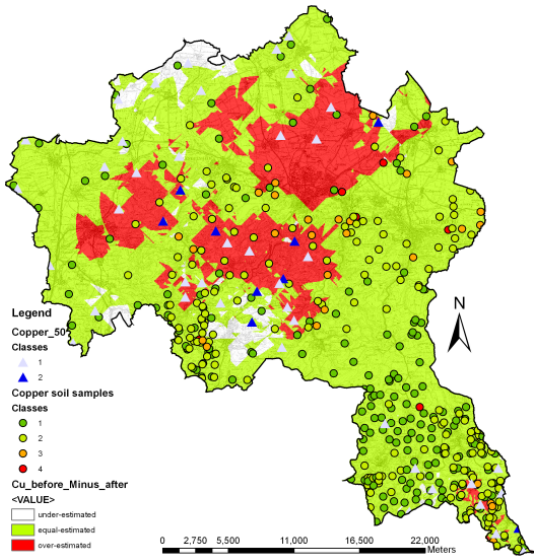

Figure (4-12, c) Predicted map of Cu before 50 minus predicted map of Cu after 50

Figure (4-12) Cu comparison between predicted maps before with after new soil samples

The predicted concentrations of soil heavy metals are also compared with the measured values for each soil heavy metal. The comparison is applied for the predicted values before and after taking the new 50 samples. This comparison is illustrated in Figure (4-13). In this figure the horizontal axis resembles the field value of soil heavy metals and the vertical axis refer to the difference between the predicted values before or after the 50 samples with respect to the measured values. The perfect prediction gives a difference zero between estimated and

measured values. In this case, the difference should follow zero horizontal line, but errors usually haunt the predictions. From Figure (4-13) we note that, the difference is closed to zero for most of soil heavy metals in case of low measurement values. While the difference increased for the high value of concentrations. This give a conclusion that the predicted maps gave a good estimation for low values of soil heavy metals and presents underestimation for the high concentration of pollutants. The measured field values of 50 new soil heavy metals are compared with the predicted values before and after taking these new samples. The comparison is based on the estimated correlation coefficient factor between them. The result is indicated in Table (4-6). The table shows that, the correlation coefficient is weak before taking the 50 values. For Pb, the Correlation coefficient was 67% before taking 50 samples which increased to 80% after them. Also the correlation values increased for all other soil heavy metals.

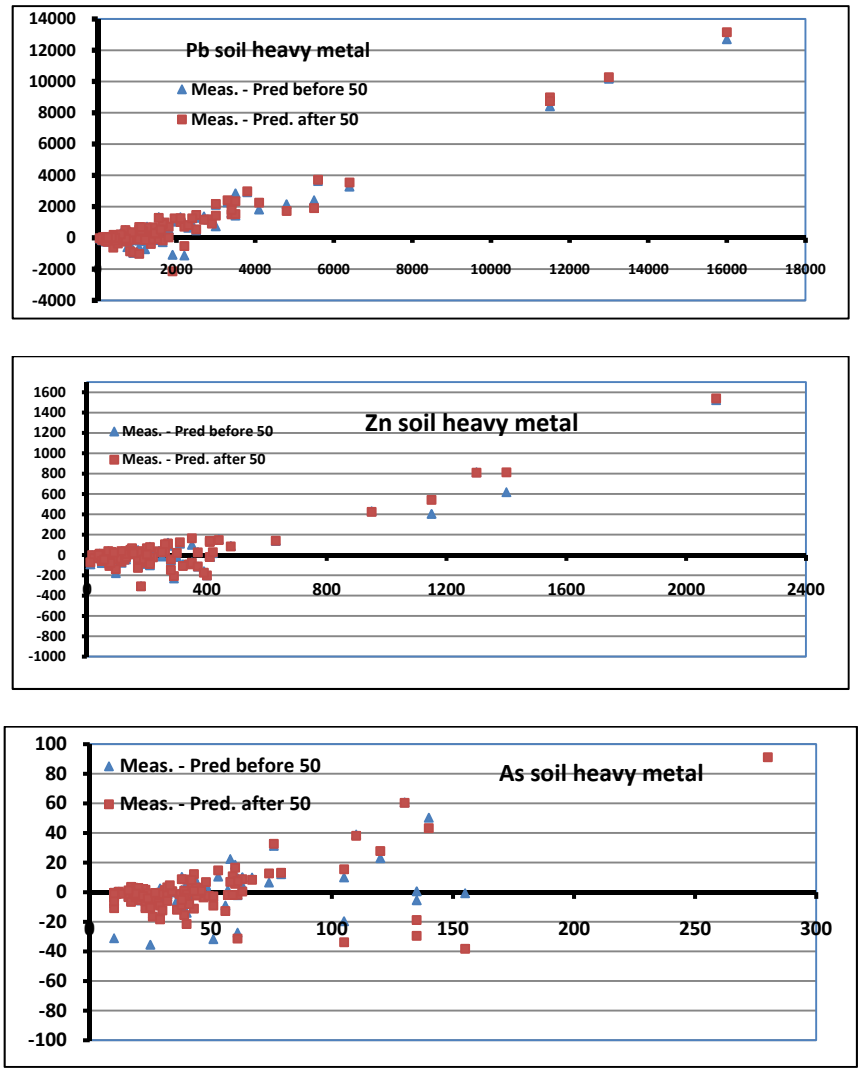

Figure (4-13) comparison between predicted maps based on the measured values

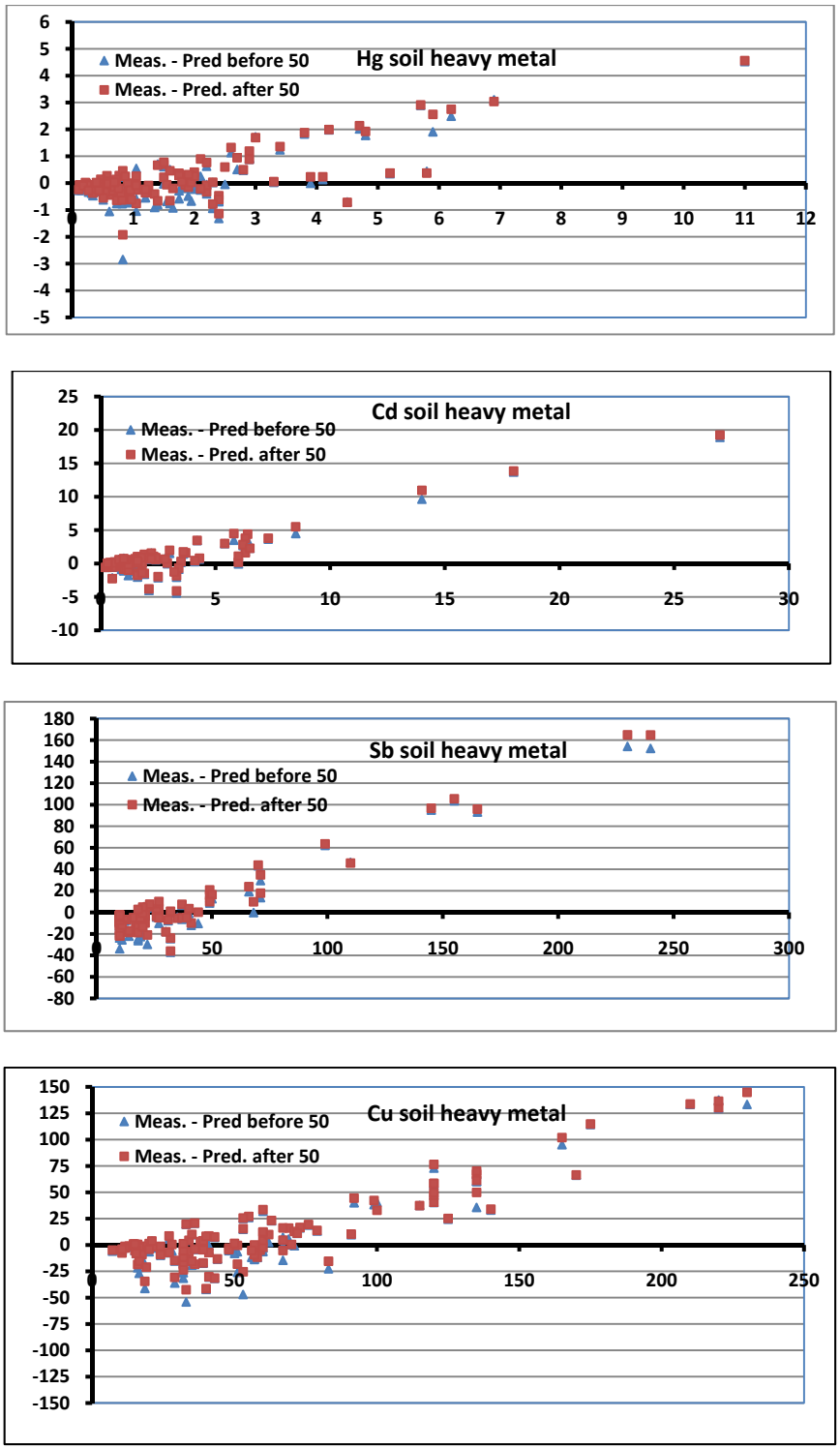

Figure (4-13) comparison between predicted maps based on the measured values
(Horizontal axis is the measured value, vertical axis is difference between measured and the predicted values before or after the new samples)

Table (4-6) Correlation coefficient between measured samples and predicted after and before the 50 new soil samples

Soil heavy metals	Correlation coefficient	
	Before	after
Pb	0.67	0.80
Zn	0.30	0.55
As	0.63	0.92
Hg	0.58	0.76
Cd	0.39	0.59
Sb	0.22	0.50
Cu	0.56	0.64

4.5 Investigation of Intensively Contaminated Sites

In Goslar County there are many hotspot locations at which forest soils are intensively polluted with heavy metals. That was caused by local mining or/and smelting activities. Therefore more care is taken to analysis these locations. Because of the assumption of second order stationarity, it is not possible by geostatistical methods to take into consideration all the hotspot areas and valley directions in one predicted map of concentrations. Therefore, many prediction values were calculated for each soil variable with different geostatistical characteristics (variogram model and search neighborhood) for each hotspot location or valley direction. Pb, for example, has three hotspot locations in Altenau, Clausthal-Zellerfeld and Lautenthal. Three prediction maps are created for these; two of them are developed for hotspot locations and one for a general prediction map named as Global Map. The result of different geostatistical structures for each predicted map of Pb and As are illustrated in Table (4-7). A combination of the predicted surfaces of different hotspot areas and the global map of the same soil heavy metal is carried out to get one spatial distribution called Merged Map. The combination of global and hotspot surfaces were done by two methods: vector method and raster method.

Table (4-7) Semivariogram properties for global and hotspot predicted maps of Pb and As soil heavy metals

soil heavy metal	Prediction map type	Fitted model	Major Semiaxis, m	Minor Semiaxis, m	Angle of major Semiaxis, 0	(C_o /C) ratio
Pb	Hotspot in Cl-Z and Lautenthal	Gaussian	2500	800	25	31.27
	Hotspot in St. Andreasberg and Altenau	Gaussian	7000	1000	15	32.70
	Global map	Gaussian	10000	10000	0	29.58
As	Hotspot in St. Andreasberg	Spherical	2000	1000	30	9.34
	Global map	Spherical	5000	5000	0	9.34

4.5.1 Composite of Global and Hotspot Maps Using Vector Method

In the vector method the geostatistical layers are converted to filled contours and the ArcEditor extension, available in ArcGIS, is used to clip and join hotspot areas with the global map. For Pb, in Altenau city there is a valley in the direction South-North as given in Figure (4-14, a). A specific prediction is developed along this valley for Pb and the result is presented in Figure (4-14, b). But in this predicted map, the level of anomaly in the whole study area are elongated in the direction of the valley which is not true, therefore this map dose not present the real contaminations exactly. Another predicted map of Pb, is produced for the global area is illustrated in Figure (4-14, c). From this figure, we notice that the predicted map of the global map is good for the whole area, but it does not resemble the Altenau valley well. To solve this problem, the predicted map of Altenau valley in the global map is selected and removed as presented in Figures (4-14, c & d). While the interested area in the Altenau map is selected and is made as a single layer as given in Figure (4-14, e). The last step is the use of the Union-Tool of the Analysis-Tools extended in ArcGIS to create one layer from Figures (4-14, d & e) to get the final predicted map given in Figure (4-14, f). The same previous steps are made for each hotspot locations within the study area to get the Merged Predicted Map. A comparison between the Global and the Merged predicted maps of Pb are illustrated in Figure (4-15). In this figure, Altenau and Lautenthal cities have concentrations of contamination in the merged map higher than that of the global map and take the valley direction. Also the difference between the two predicted maps is calculated using 3D-Analyst extension in ArcGIS as presented in Figures (4-16). The red color in Figure (4-16) refers the overestimated areas in the merged map compared with the global map. While the green color gives equal-estimation and the white color refers to underestimation. Figure (4-17) gives two profiles along the areas of interest which illustrate the difference between the two predicted maps within the hotspot locations.

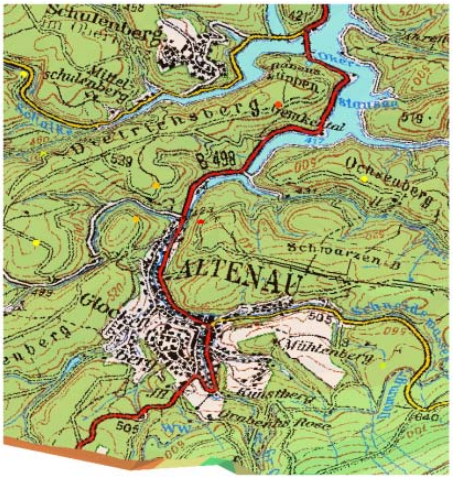

Figure (4-14, a) valley of the Altenau area

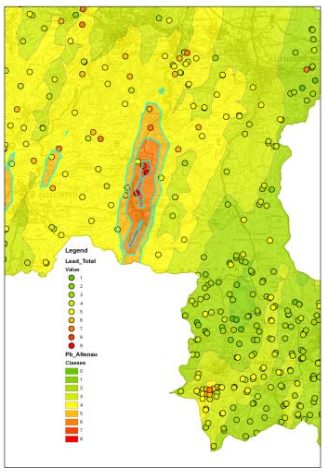

Figure (4-14, b) Pb specific predicted map for the Altenau Valley

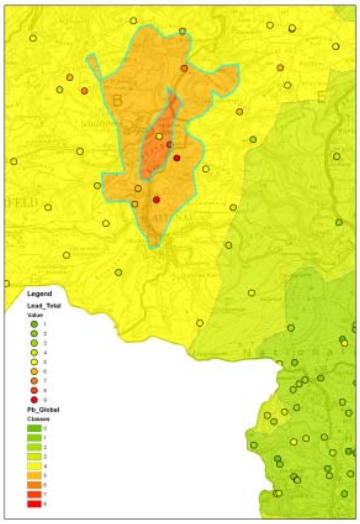

Figure (4-14, c) Pb Global predicted map

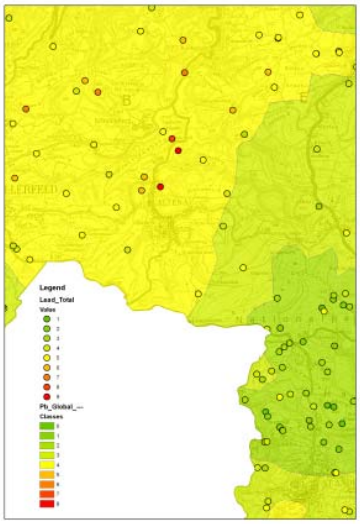

Figure (4-14, d) Pb Glopal map without the location of Altneau valley

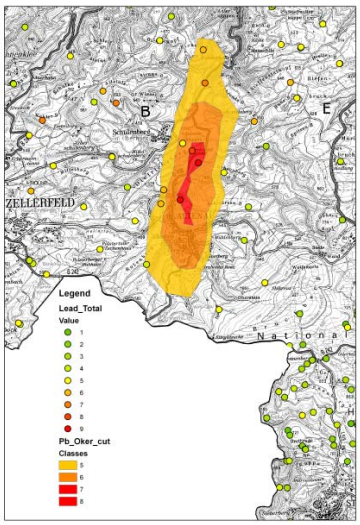

Figure (4-14, e) Selected the interested area from Figure (4-14,b) and created as single layer

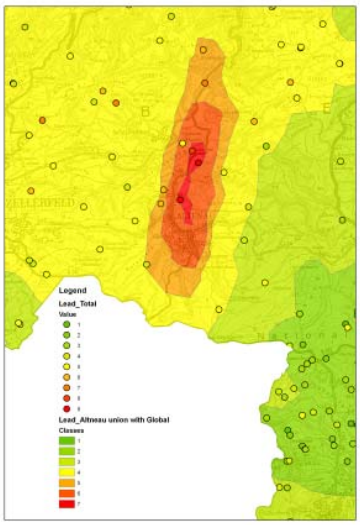

Figure (4-14, f) union between the Global map of Figure (4-14, d) and the single layer in Figure (4-14,e)

Figure (4-14) Steps of creating merged predicted map from hotspot locations and global prediction

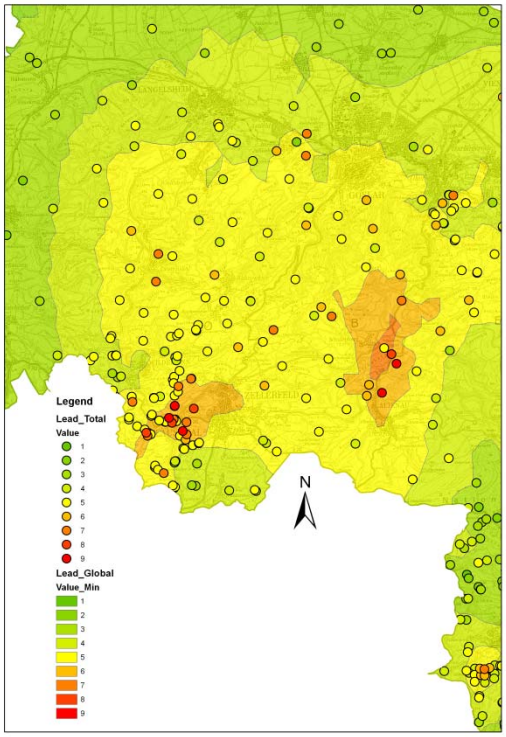

Figure (4-15, a) Pb Global- Map

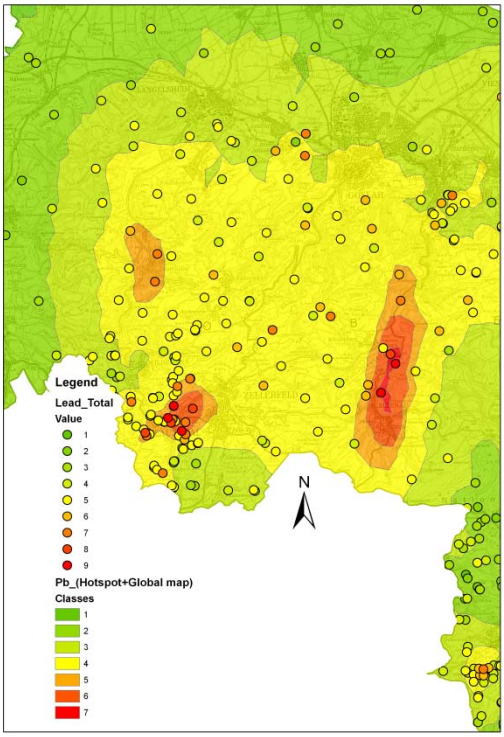

Figure (4-15, b) Pb Merged-Map

Figure (4-15) Comparison between Pb Global prediction map and merged hotspots locations into the Global map

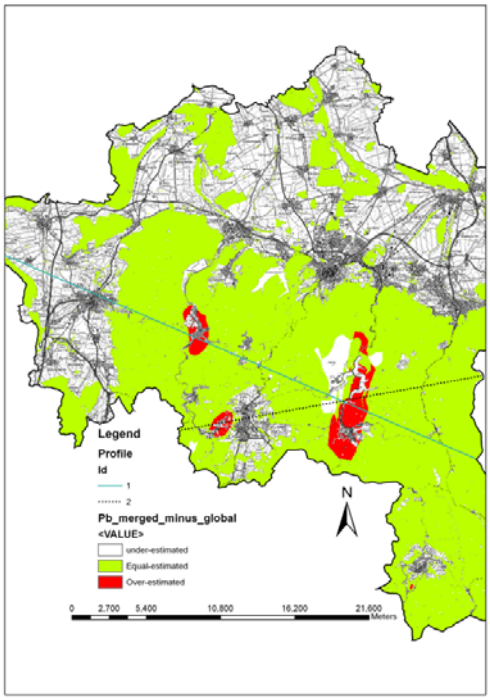

Figure (4-16) difference between Pb Merged map and Global predicted map

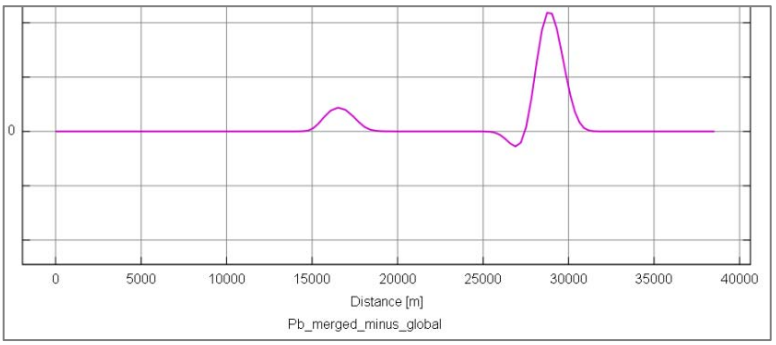

Figure (4-17, a) Profile (1)

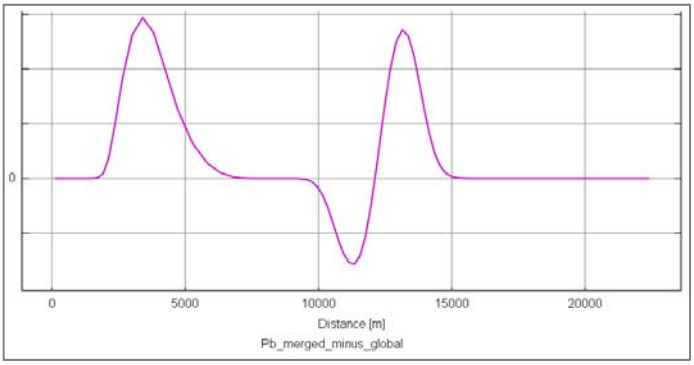

Figure (4-17, b) Profile (2)

Figure (4-17) Profiles along the hotspot locations of Pb soil heavy metal (vector method)

For As, it has a hotspot location in the south region of the study area around St. Andreasberg city. Specific geostatistical parameters, are applied to As in this area, are given in Table (4-7). The specific predicted area is also cut and merged into the predicted Global map as explained for Pb. Figure (4-18) gives the steps of merging the hotspot location into the global map of As. Additional to cut and union the filled contour could also be modified by controlling the vertices of them. Figure (4-18, a) presents the vertices of a polygon which could be modified using ArcEditor extension in ArcGIS. The filled contours are modified to be more concentrated around the hotspot location as illustrated in Figures (4-18, c & e).

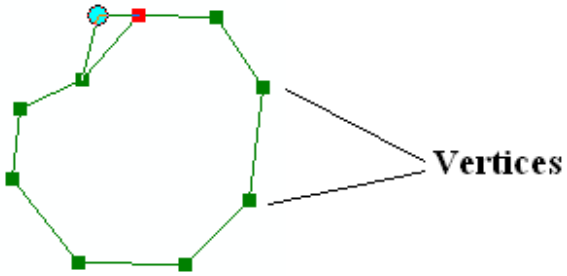

Figure (4-18, a) vertices could be modified to reshape the polygon

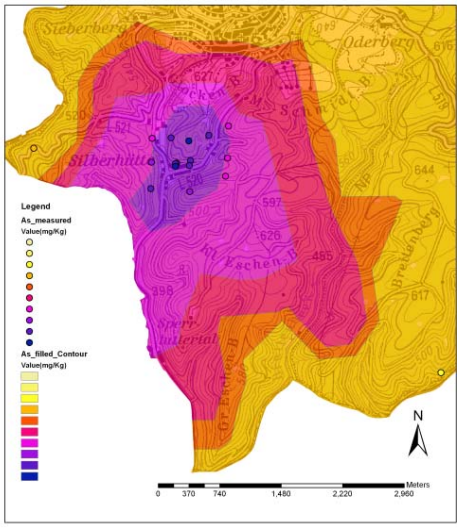

Figure (4-18, b) Global predicted map of As in St. Andreasberg

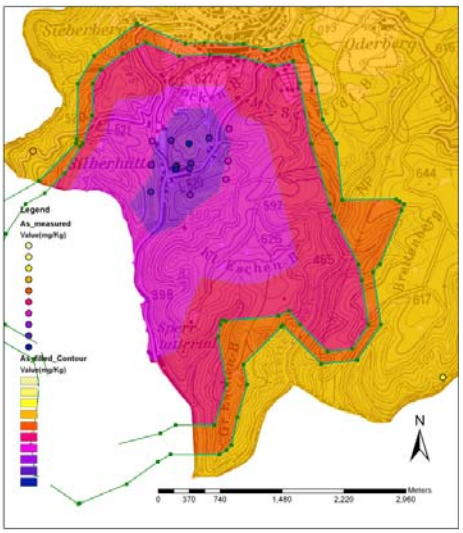

Figure (4-18, c) Selected Border lines to be modified to As Global map

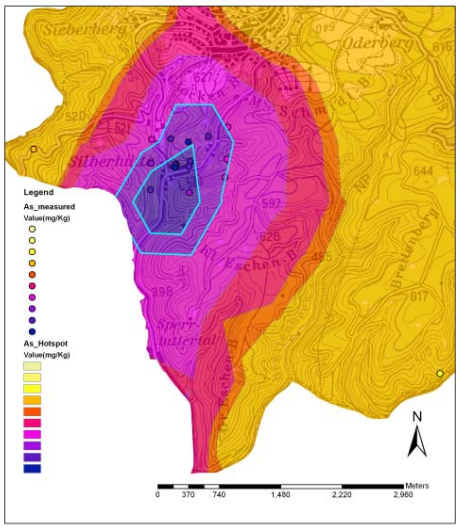

Figure (4-18, d) As Hotspot and the selected levels to be merged in the Global modified map

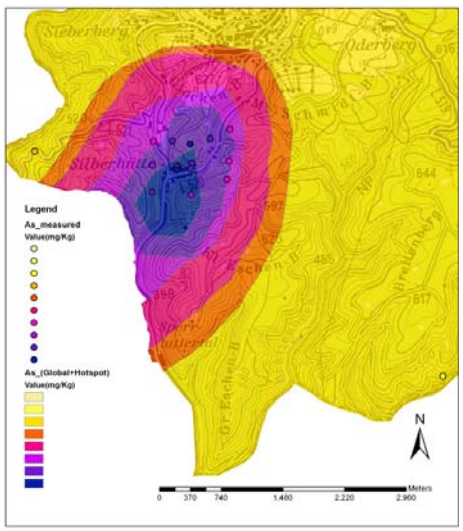

Figure (4-18, e) As Merged predicted map

Figure (4-18) merging Hotspot locations into the Global predicted map for As

4.5.2 Raster Overlaying Method

Merging the hotspot locations into the global map of the soil heavy metals could be applied also using raster method. In this method, the geostatistical layers are converted to raster. A GIS model is built to apply this method as given in Figure (4-19). The feeding layers to the model are hotspot geostatistical layers, Global gostatistical layers and map of forest regions. The model converts all geostatistical layers to raster, cut the hotspot locations and merge them into the global predicted map. To avoid the discontinuity between the merged parts, the model generates an overlap zone. We can summarize the model steps as follows: (1) convert the geostatistical layers of the hotspot to filled contour; (2) select the highest contour values of hotspot layers; (3) convert the selected contour to polygons; (4) select the required polygon of the hot spot area; (5) make a buffer zone with specific distance (overlap distance) to the selected polygon; (6) convert both the geostatistical layers of hotspot and the Global layers (G) to raster form; (7) extract by mask the hotspot raster, using the mask as the polygon in step 4 and the buffer area (B) in step 5; (8) calculate the Euclidean distance (w) for the clipped area by the polygon in step 4 with the same distance of step 5, this area is used as overlap region; (9) calculate the overlap area which is pasted in the Global raster using Equation (4-1) (The specific distance which used as overlap area selected as 500 m); (10) use Mosaic-Tool to composite the calculated area in step 9 with the Global raster layers; (11) repeat the previous steps for the other hotspot locations of the same soil heavy metal, the final result are a Global map combined with all the required hot spot of this variable.

$$G * \frac{w}{\text{Overlap Distance}} + B * \left(1 - \frac{w}{\text{Overlap Distance}}\right) \qquad (4\text{-}1)$$

Comparison between the spatial distribution of Pb Global and Pb Merged is presented in Figure (4-20). The figure compares between the general prediction map (global prediction map) of Pb and the predicted soil contamination levels after combining hot-spot locations with the global predicted map. Difference between merged and global map are calculated by 3D analyst-Tools, ArcGIS and the result is given in Figure (4-2, a). Also a line profile is created to illustrate the difference between the global and merged predicted maps in Figure (4-21, b). Comparing between vector and raster methods which are used to add the effect of Hotspot location to the Global Prediction map we find that, the filled contour method gives more smother and precise shapes and we can control the extended polygon. Raster method is more practical because using a GIS model especially in case of many Hotspots for one variable and many soil heavy metals have hotspot locations. But

the final result is in favor of the method of vector, which gives better results than the raster method.

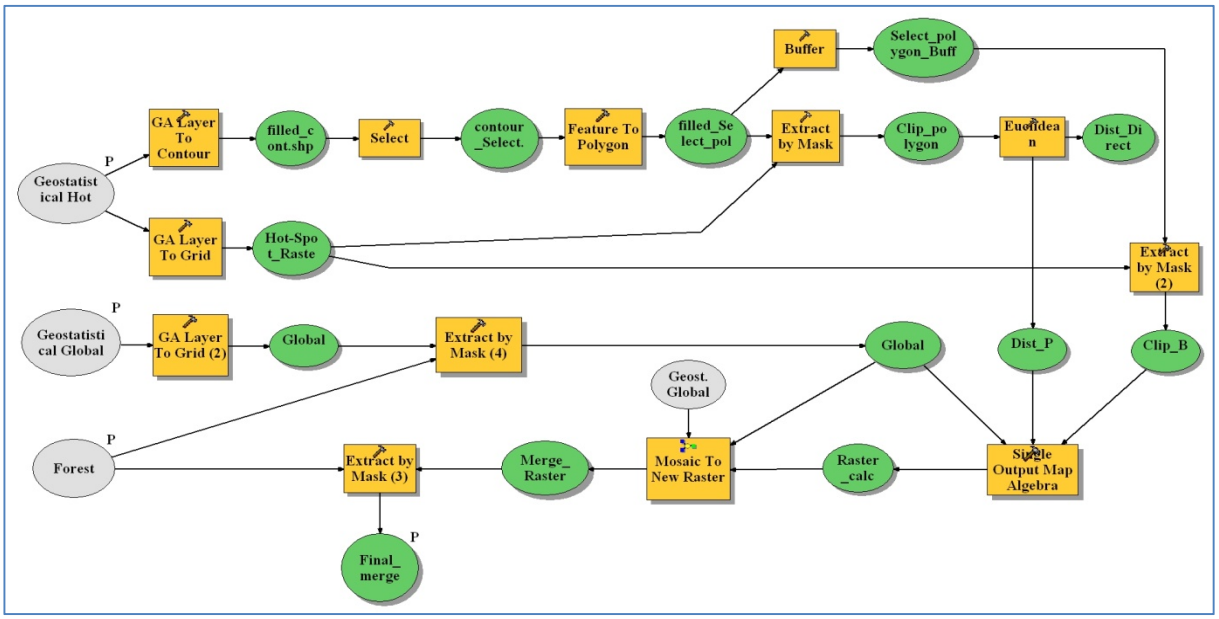

Figure (4-19) a built-model to merge hotspot locations into general predicted map using raster method

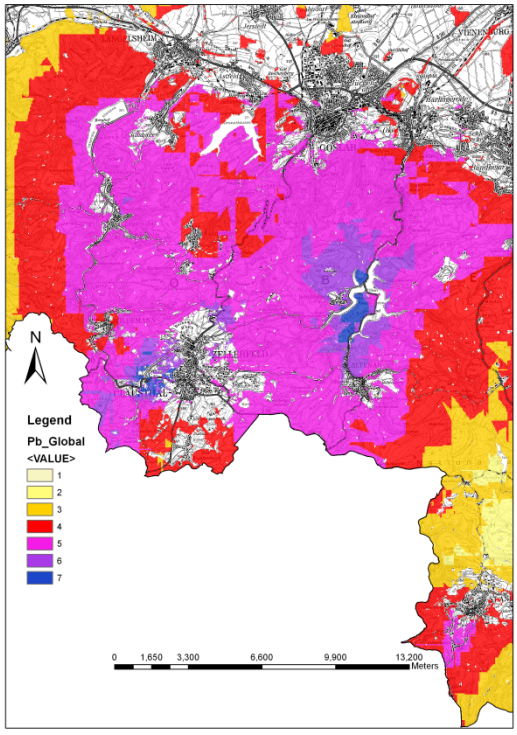

Figure (4-20, a) Pb Global predicted map (Raster)

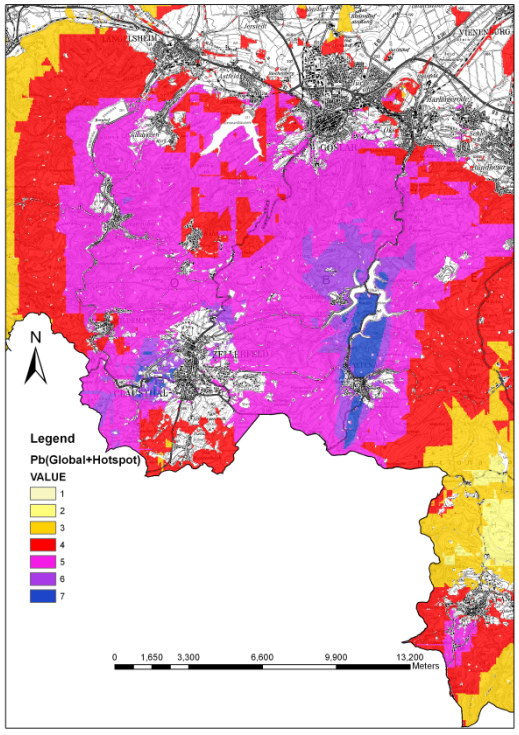

Figure (4-20, b) Merged predicted map of Pb (raster)

Figure (4-20) Comparison between Pb global prediction map and merged hotspots locations into the global map (Raster method)

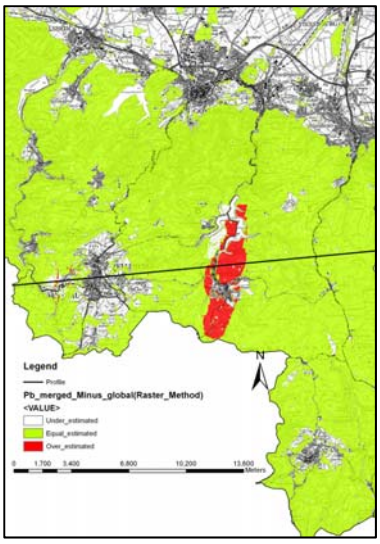

Figure (4-21, a) Pb Merged map minus Pb Global map

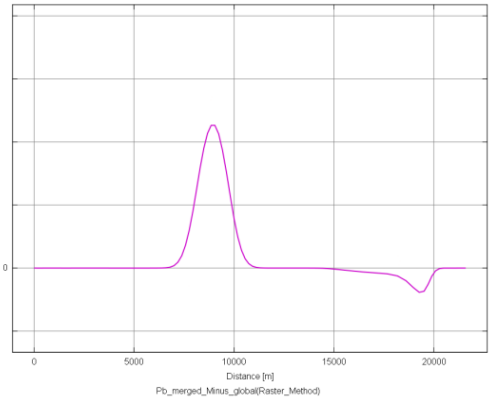

Figure (4-21, b) Profile along the hotspot location

Figure (4-21) Calculated difference between Pb Merged map and Global map with a profile along the interested location (raster method)

4.6 Effect of Inclined Distance on Geostatistical Estimations

Geostatistical prediction of unknown value depends mainly on the distance between the measured samples. Most of geostatistical software uses the horizontal distance (2D) between variables to generate the predicted maps. The horizontal distances computed only from X and Y coordinates values. This assumption is true only if the study area is a level region which is not the case in our world. Any distance in the real world need X, Y and Z to calculate the real or inclined distance between any two points. The effect of inclined distance on the predicted values is discussed in this section. 30 sampled values of a soil heavy metal are used to estimate 32 unsampled locations using Ordinary kriging method. Microsoft Excel was used to estimate the experimental semivariogram based on inclined distances. The fitted semivariogram is generated by Matlab software. Also Matlab is used to solve the Ordinary kriging matrices and calculate the soil heavy metal values at unknown locations. The procedures of calculations are applied on four cases as follow: (1) inclined distance with raw data set (3D), (2) inclined distance with log data set (3D-Log), (3) horizontal distance with raw data set (2D); and (4) horizontal distance with log data set (2D-Log). Figure (4-22) indicates the fitted models in each case. The same unknown locations are estimated also using Geostatistical Analysis extension in ArcGIS and the results are given in Table (4-8). The Table compares between predicted values using horizontal to inclined distances. The table contains also statistics of the measured soil samples and the predicted values using ArcGIS software. We can see that, there is no noticeable difference between using inclined distances or horizontal distances on the estimated values. But the difference is

visible between raw data sets and Log-data sets. The average value estimated from 2D and 3D methods is 95 mg/kg, which is the nearest value to the average of the samples measured.

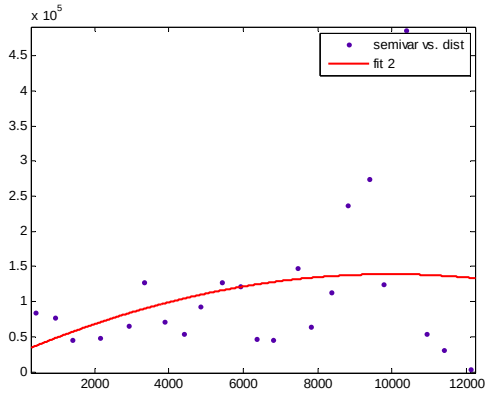

Linear model Poly2:
f(x) = p1*x^2 + p2*x + p3
p1 = -0.001121 (-0.005166, 0.002923)
p2 = 22.36 (-29.62, 74.33)
p3 = 2.769e+004 (-1.158e+005, 1.712e+005)
Inclined distance with raw data sets (3D)

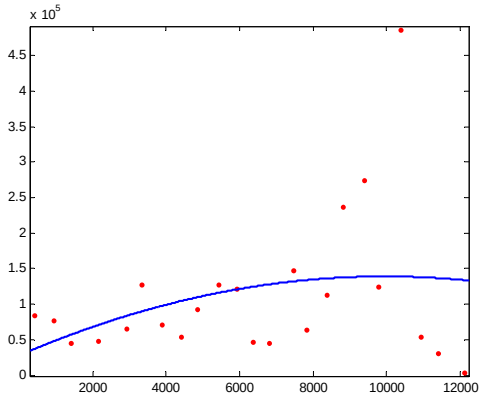

Linear model Poly2:
f(x) = p1*x^2 + p2*x + p3
p1 = -0.001122 (-0.005165, 0.00292)
p2 = 22.36 (-29.58, 74.3)
p3 = 2.773e+004 (-1.156e+005, 1.711e+005)
Horizontal distance with raw data sets (2D)

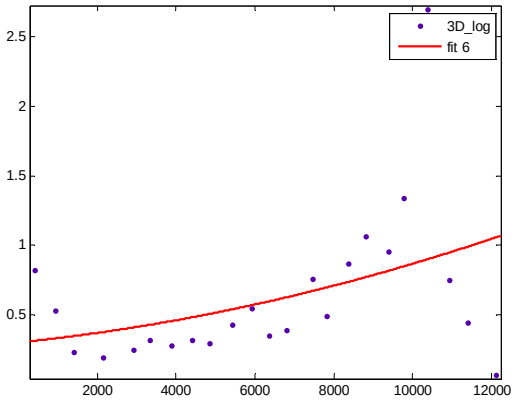

Linear model Poly2:
f(x) = p1*x^2 + p2*x + p3
p1 = 2.758e-009 (-1.801e-008, 2.352e-008)
p2 = 2.906e-005 (-0.0002378, 0.0002959)
p3 = 0.299 (-0.4377, 1.036)
Inclined distance with Log-data sets (3D-Log)

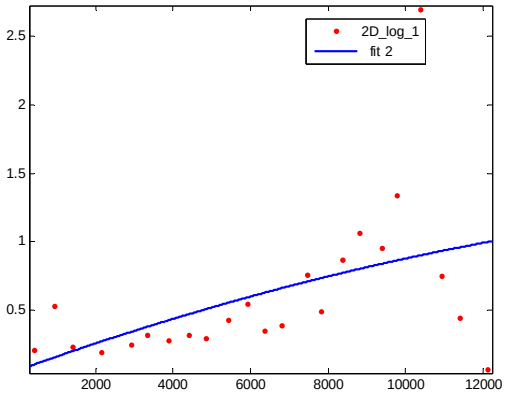

Linear model Poly2:
f(x) = p1*x^2 + p2*x + p3
p1 = -2.035e-009 (-2.208e-008, 1.801e-008)
p2 = 0.000102 (-0.0001556, 0.0003596)
p3 = 0.0596 (-0.6514, 0.7706)
Horizontal distance with Log-data sets (2D-Log)

Figure (4-22) Fitted semivariogram model for inclined and horizontal distances

Table (4-8) Estimated of unsampled locations using horizontal and inclined distances

	3D	3D-Log	2D	2D-Log	OrKr ArcGIS	OrKr_Log ArcGIS	Measured values
Count	32	32	32	32	32	32	30
Minimum	95.97	131.49	95.34	132.87	200.67	207.04	74
Maximum	1189.7	1119.3	1189.5	1114	867.49	735.77	1400
Mean	332.58	319.01	332.82	316.31	336.98	350.43	378.93
std	240.37	217.36	240.65	213.42	164.7	138.07	307.07
Quantile 25%	197.09	201.09	197.61	197.22	228.28	249.74	200
Median	232.61	237.14	232.57	237	264.84	308.01	255.61
Quantile 75%	371.27	370.74	371.54	369.17	353.78	383.66	414.07

Chapter (5) Results and Discussion of Air Dispersion Modeling

This chapter comprises the results obtained from the generated Auxiliary Meteorological Model and Dispersion Plume Model. The generated models were applied on Pb Clausthal-Zellerfeld smelter using the measured meteorological data from 2004 to 2009. The chapter firstly presents some statistical analysis of the measured meteorological data such as wind and ambient temperature. The generated Auxiliary Meteorological Model used these meteorological data to determine the atmospheric stabilities based on Pasquill–Gifford classifications. The model examines a new approach to determine the amount of insolation strength during day hours. Instead of using the solar elevation angle and amount of cloud cover, the model used the measured solar radiation to determine amount of insolation. Based on the results of atmospheric stabilities the model estimates friction velocity, Monin-Obhkouv length, convective velocity, mixing height, and deposition velocity. The frequency distribution of the determined atmospheric stabilities was classified according to the four seasons of the year. Diurnal variations were developed for the measured meteorological parameters and the estimated parameters. The chapter also presents the results of the Dispersion Plume Model. The model used the results from Auxiliary Meteorological Model as feed data additional to the smelter stack parameters. The model examined the plume rise emitted from smelter stack at different meteorological conditions. This chapter also gives the estimated concentrations of Pb particles emitted from Clausthal-Zellerfeld smelter. Finally, the chapter provides a comparison between the predicted concentrations of soil contaminations from geostatistical analysis with the estimated values by the dispersion modeling.

5.1 Analysis of Meteorological Data

Meteorological data in Clausthal-Zellerfeld is used to demonstrate the application of Auxiliary Meteorological Model and Dispersion Plume Model. The meteorological and topographical conditions of the area are generally more complex than the features of inland areas (such as Goslar city). The hills and the valleys around the area can combine to prevent the dispersion of pollutants. Surface meteorological data of Clausthal-Zellerfeld was measured by a weather station located on the Institute of Electrical Information Technology at Clausthal University of Technology. The station located at 51.80511 N and 10.33761 E with height of 600 m above sea level. The available meteorological data are from 2004 to 2009, and the station measures wind speed, wind direction, temperature, pressure, relative humidity, precipitation and incoming solar radiation. Cloud cover information is not available during this period. The weather station measures the meteorological

data at each minute; therefore a simple Matlab code is developed to get hourly average values for each measured meteorological parameter. Statistical analysis of the measured meteorological data is developed for winter, spring, summer and fall seasons. The wind speed and its direction are analyzed using Wind Rose Plots for meteorological data WRPLOT, version (5.9) (www.weblakes.com/). Analysis of wind speed and wind directions is very important to determine the transport and dispersion directions of air pollutants. Table (5-1) presents the statistical analysis of wind speed and the frequency of occurrence for each speed categories. Wind speed categories are classified to meet the wind speed ranges suggested by Pasquill-Gifford as indicated in Table (3-2). From Table (5-1) we note that, the average wind speed is almost equal in the four seasons. Maximum wind speed values are 7.13 m/s, 8.17 m/s, and 9.44 m/s, 11.24 m/s at summer, fall, spring and winter, respectively. Calm wind means that the wind speed is almost zero. The occurrence of calm wind is relatively low with value of 1.58% for the total measurements. There is a significant frequency of the wind speed category less than 2 m/s at all season. For example, the frequency of this category is 46.72%, and 40.54 % in summer and fall respectively. The high frequency of wind speed that is less than 2 m/s makes the occurrence of stable atmosphere (E and F categories) more satisfied than the neutral conditions during the night in case of clear sky. Wind rose analyzed the wind direction with the same wind speed category of Table (5-1). Figure (5-1) illustrates the results of wind rose for each season and for the total measurements. The wind is mostly blowing towards North-East direction with significance frequency towards North direction. For all seasons, the frequency of wind speed is from 27% to 36% to the North-East direction with different angles from the north, and from 10% to 18 % to the North. For the total measured wind data, frequency of wind direction is 32 % towards North-East and 14% towards North direction.

Table (5-1) Wind speed analysis in Clausthal-Zellerfeld from 2004 to 2009

	Winter	Spring	Summer	Fall	Total data
Min	0	0	0	0	0
Average	2.87	2.43	2.11	2.46	2.47
Max	11.24	9.44	7.13	8.17	11.24
Std	1.74	1.36	1.16	1.43	1.46
Speed range	Frequency of occurrence, %				
Calm wind	1.17	1.37	2.2	1.59	1.58
<2	35.29	39.41	46.72	40.54	40.50
2-3	20.01	28.13	29.99	24.57	25.69
3-4	17.51	18.76	16.55	18.41	17.81
4-5	13.25	8.82	5.12	10.22	9.35
5-6	8.42	3.49	1.27	4.96	4.52
>6	5.52	1.39	0.35	1.30	2.13

The height of the study area from sea level causes low temperature and medium precipitation, especially in the winter, in comparison with inland areas. Maximum temperature noted in summer days is 31 ^{o}C, while minimum temperature reaches to -20 ^{o}C during winter nights. The average temperature in the spring and fall days is 9 ^{o}C. During summer the temperature is relatively high that increases sometimes than 30 ^{o}C during day hours, while the average value is ^{o}C. The average solar radiation during the winter day hours not exceeds 105 W/m^2, with maximum of 480 W/m^2. While the maximum incoming solar radiation in summer days reaches to 640 W/m^2 with average value of 310 W/m^2. In spring and fall seasons, the average solar radiation during the day is 216 W/m^2, and 144 W/m^2 respectively. The high values of surface temperature and solar radiation in summer increases the occurrence of unstable classes (A, B and C); hence increases the dispersion of pollutants in the atmosphere. The atmosphere in the study area has high humidity for most of time in a year with average value of 90 % in the winter and 84 % in the summer. The average precipitation is 0.13 mm/h and the snow is the predominant during the winter and some days in the spring, while the rain is prevailing during summer and fall seasons.

5.2 Atmospheric Stability in the Study Area

The Auxiliary Meteorological Model uses meteorological data to determine hourly atmospheric stabilities according to Pasquill-Gifford's classification. According to every stability category, the model estimates friction velocity, Monin–Obukhov length, mixing height and deposition velocity. Determination of atmospheric stabilities (A, B, C, D, E, and F) requires information of insulation strength, wind speed, daytime and amount of cloud cover (Schnelle & Dey 2000). Because of the absence of cloud cover data at the smelter location (Clausthal-Zellerfeld), this study uses the measured incoming solar radiation to determine the insolation strength during day hours. Table (5-2) gives the suggested categories of incoming solar radiation as follow: greater than 500 W/m^2 for strong insolation; from 500 W/m^2 to 300 W/m^2 for moderate insolation; from 300 W/m^2 to 200 W/m^2 for slight insolation and less than 200 W/m^2 for weak insolation. The solar altitude is a function of location, day time, and year time. When clouds exist, their cover and thickness decrease the incoming and outgoing radiation whereas the solar altitude has no effect and still unchanged. Therefore using the measured solar radiation to determine stability of atmosphere is more reliable than using solar altitude. The hourly solar elevation angle (solar altitude) is determined at Clausthal-Zellerfeld during the same period of investigation (from 2004 to 2005). The calculated solar altitude is classified based on insolation strength categories and is compared with measured incoming solar radiation at each corresponding time as presented in

Table (5-2). In case of summer days, the solar altitude is more than 60°, and the insolation should be strong, but the existence of clouds reduces insolation strength to be moderate or slight. Table (5-2) indicates that, during the hours at which solar altitude is greater than 60°, only 10.4% of the measured incoming radiation is greater than 500 W/m^2 (strong insolation). In times of solar altitude range from 35° to 60°, the occurrence of moderate insolation is 34.9% from the measured radiation.

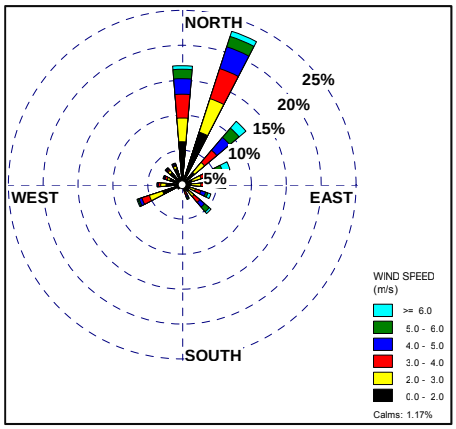

Wind Rose in Winter

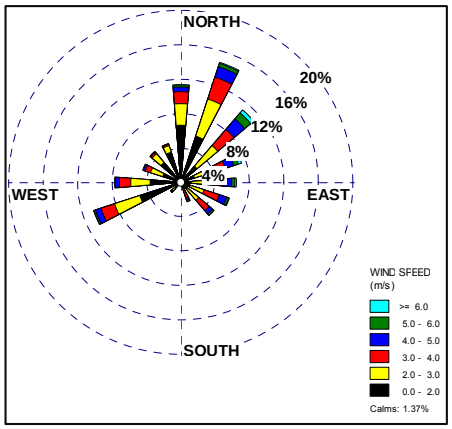

Wind Rose in Spring

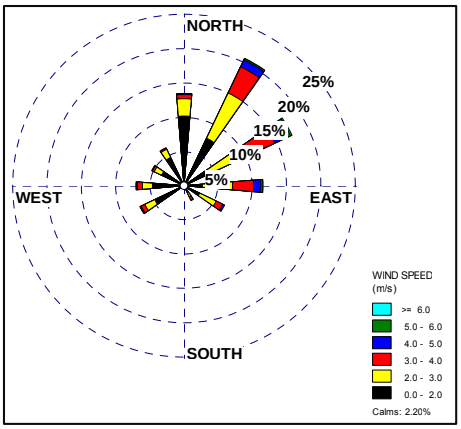

Wind Rose in Summer

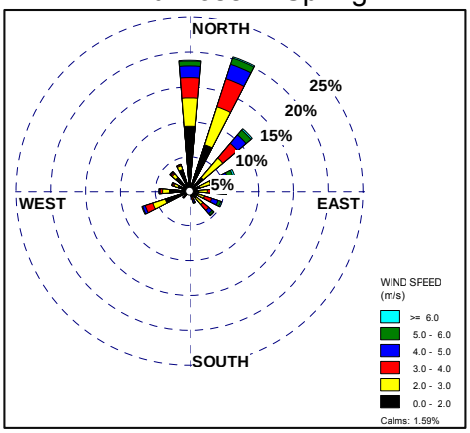

Wind Rose in Fall

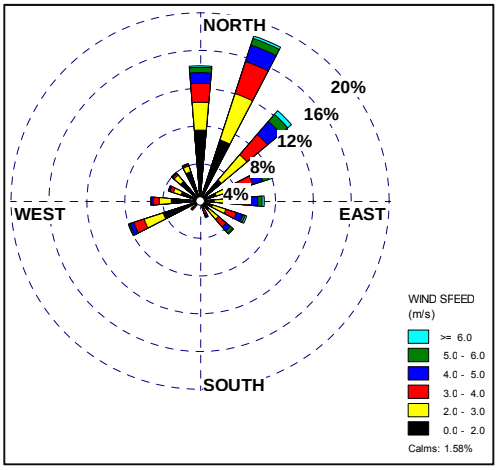

Wind Rose for total measurements

Figure (5-1) Wind-Rose diagram, with the proportion of calm winds identified in the central circle

Table (5-2) Suggested incoming solar radiation based on insolation strength

Insolation strength	Solar Altitude, (h^o)	Suggested incoming radiation categories, W/m^2	Frequency of measured data according to solar categories
Strong	60< h	>500	10.4% are greater than 500 W/m^2
Moderate	35< h ≤60	500-300	34.49% are moderate
Slight	15< h ≤35	300-200	25.75% are slight
Weak	h ≤15	>200	95.83% are less than 200 W/m^2

The generated Auxiliary Meteorological Model predicts hourly atmospheric stabilities according to the suggested incoming solar radiation, time, and wind speed categories as given in Table (5-3). When solar radiation is less than 200 W/m^2, the sky is heavily covered with clouds; hence the neutral atmospheric stability is dominated at any wind speed category as indicated in the table. During the night, the amount of cloud cover is determined by the measured wind speed. If the measured wind speed is less than 2 m/s the cloud covers assumed to less than 3/8 and the atmosphere has F stability.

Table (5-3) atmospheric stability categories as a function of suggested incoming solar radiation, time, and wind speed

wind speed m/s	Daytime incoming solar radiation in W/m^2				Nighttime Cloud cover	
	>500	300-500	200-300	<200	>4/8	< 3/8
< 2	A	A	B	D	E	F
2 – 3	A	B	B	D	E	F
3 – 5	B	B	C	D	D	E
5 – 6	C	C	D	D	D	D
> 6	C	D	D	D	D	D

The predicted Pasquill-Gifford atmospheric stabilities via the Auxiliary Meteorological Model are classified according to each season for day and night hours. Day time begins from one hour after sunrise to one hour before sunset of the local time. The frequency of occurrence of atmospheric stability categories is developed and given in Figure (5-2) for daytime, Figure (5-3) during nighttime and figure (5-4) for all measurement times. In each season, the atmosphere was found to vary from very unstable to very stable Pasquill-Gifford stability classes. Generally, the atmosphere is more neutral for a longer period during day-hours. During day-hours, solar incoming radiation should be strong in summer, therefore it is expected that the occurrence of unstable conditions increased in this time than any other seasons. Figure (5-2) shows that during day-hours, stability of the atmosphere is mostly neutral at winter and fall, while it is 50% unstable condition in summer and spring. During night-hours the atmosphere is more stable than neutral condition. It is 75 % stable in winter, spring and fall, while it is 92 % stable in summer. Very stable

conditions (stability F) refer that the occurrence of inversion layer especially after mid night. The inversion layer hinders the vertical dispersion of pollutants in the atmosphere which increases the deposited contaminations on ground surface. Figure (5-4) illustrates that, the atmosphere is mostly stable with frequency of 56.79%, 48.39%, 49.02%, and 55.35% in winter, spring, summer, and fall respectively. The high frequency of stable condition occurrence is caused by the high frequency of wind speed category less than 2 m/s as indicated in Table (5-1).

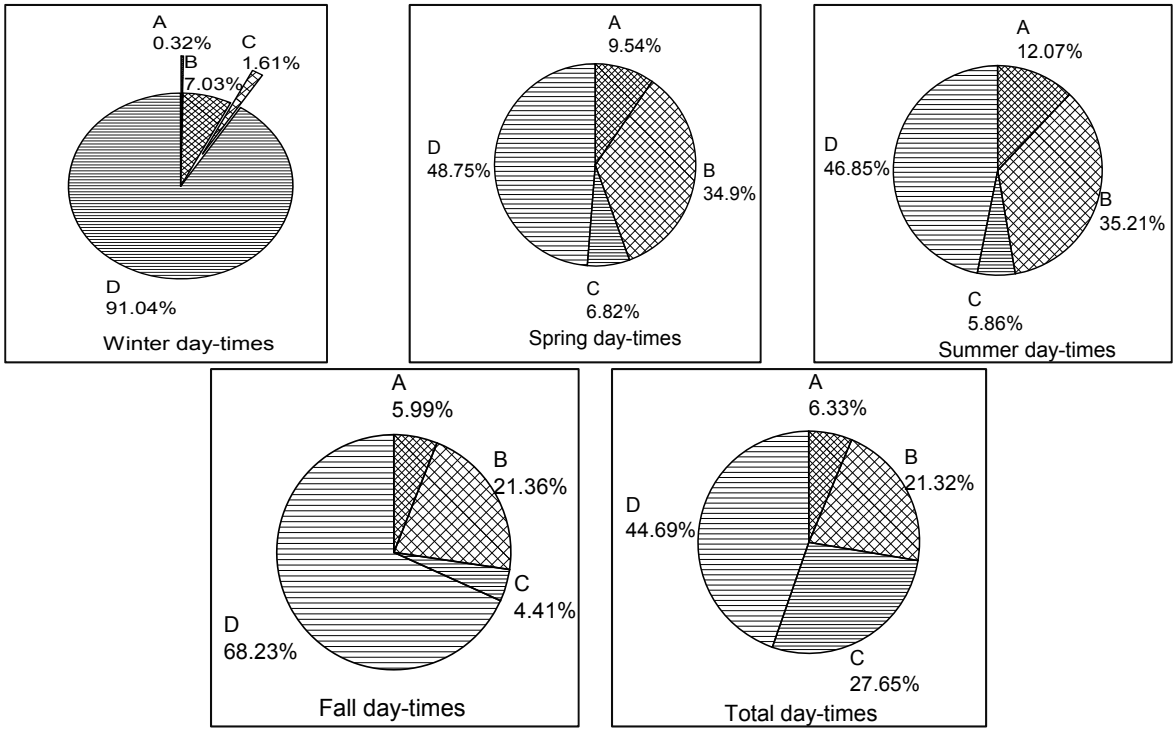

Figure (5-2) Occurrence of Pasquill-Gifford stability categories during day hours

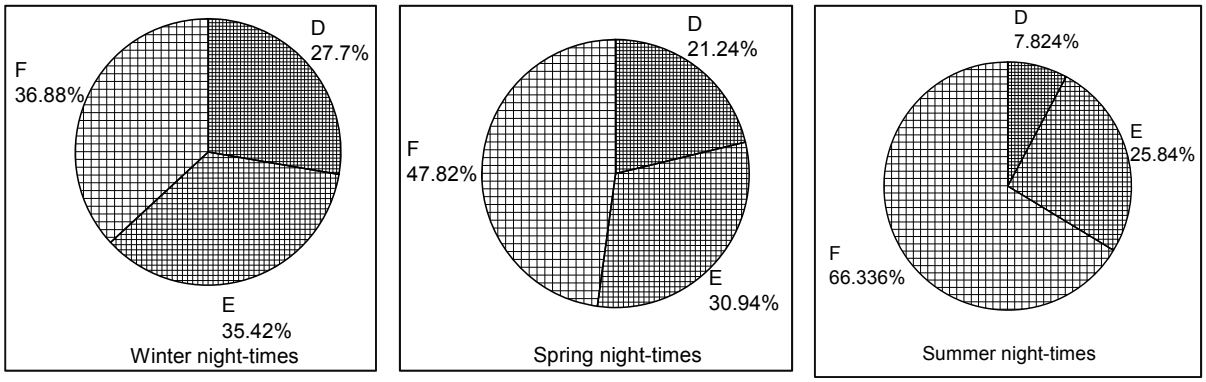

Figure (5-3) Occurrence of Pasquill-Gifford stability categories during night hours

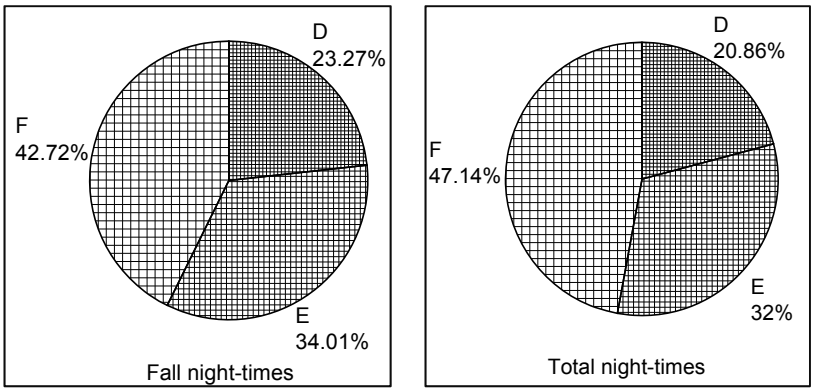

Figure (5-3) Occurrence of Pasquill-Gifford stability categories during night hours

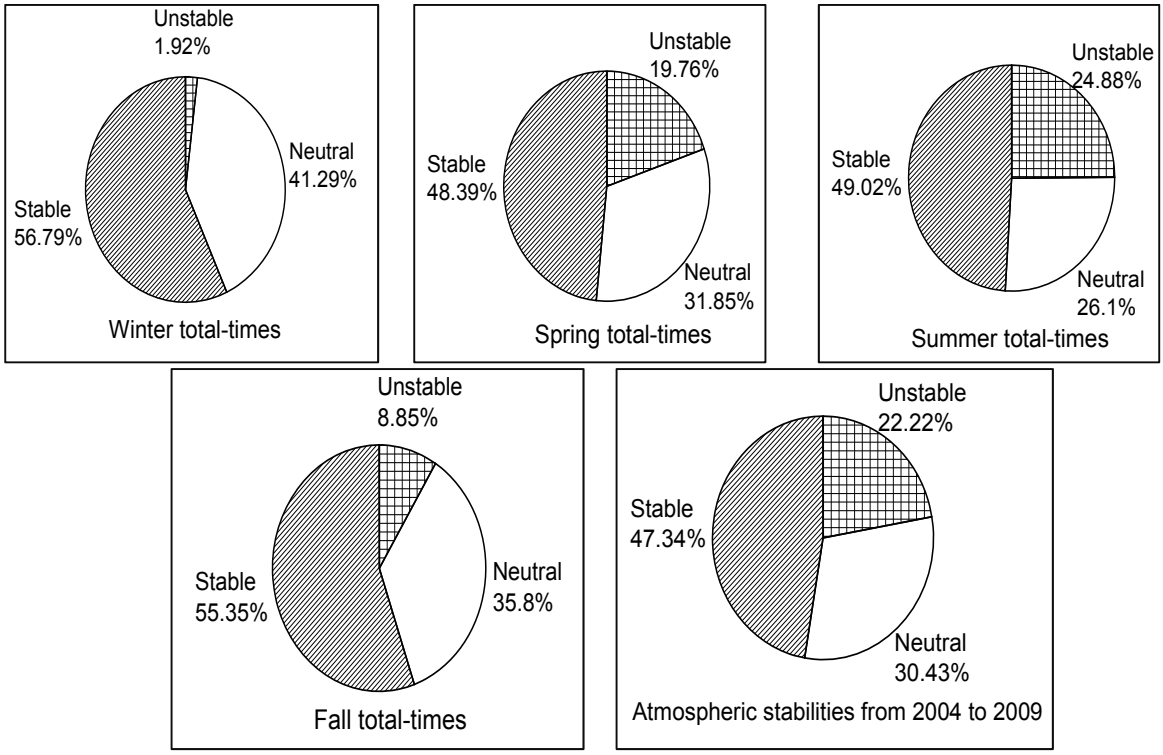

Figure (5-4), Total occurrence of Pasquill- Gifford stability categories

5.3 Estimated Values of Mixing Height

Hourly mixing height is estimated by the Auxiliary Meteorological Model based on atmospheric stability categories. Also the model estimates friction velocity, Monin-Obhkouv length, convective velocity, and deposition velocity. During the day-hours, turbulent mixing is formed by convective methods from strong surface heating, whereas during the night-times, primarily the mechanical turbulent by wind dominates the height mixing layer. Diurnal variations of prevailing wind speed, temperature, incoming solar radiation, friction velocity, convective velocity, and mixing height for all seasons were developed as presented in Figure (5-5). From the figure we can see that, there is a strong relationship between mixing height and wind speed values during the night-times. Also the relation between measured solar incoming radiations is pronounced with the calculated mixing height and convective

velocity during day-hours. The average wind speed in the winter and fall night-hours is higher than that of summer and spring. As a result, the calculated friction velocity and mixing height in winter and fall night-hours are also higher than the estimated values during summer and spring seasons. During day-hours, solar radiation during spring and summer is higher than that in the winter and fall. Average solar radiation is 340 W/m^2, 280 W/m^2, 180 W/m^2, and 100 W/m^2 in summer, spring, fall, and winter, respectively. The estimated average heights of mixing layer are 1000 m, 800 m, and 750 m, 620 m, for summer, spring, fall, and winter, respectively. Also we can conclude from Figure (5-5) that, convective velocity values in spring and summer are high than that of winter and fall at day or night times. The reason is that, convective velocity depends only on the solar radiation.

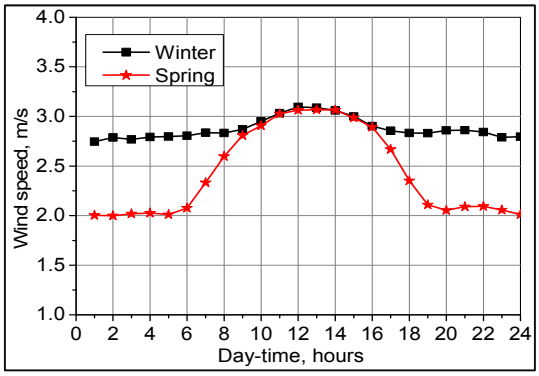

Figure (5-5, a1) Diurnal variation of wind speed in winter and spring

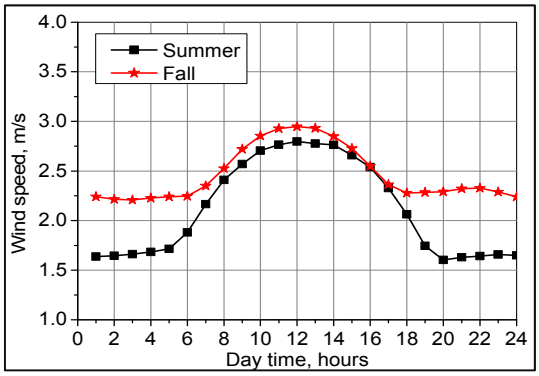

Figure (5-5, a2) Diurnal variation of wind speed in summer and fall

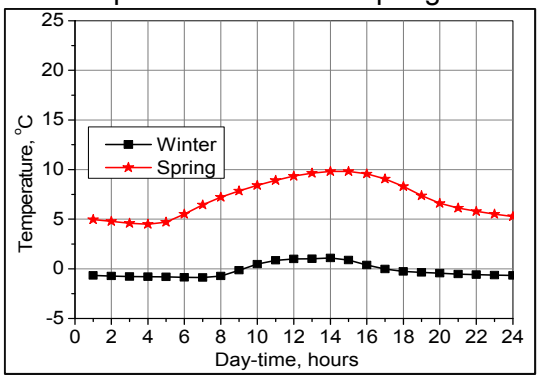

Figure (5-5, b1) Diurnal variation of temperature in winter and spring

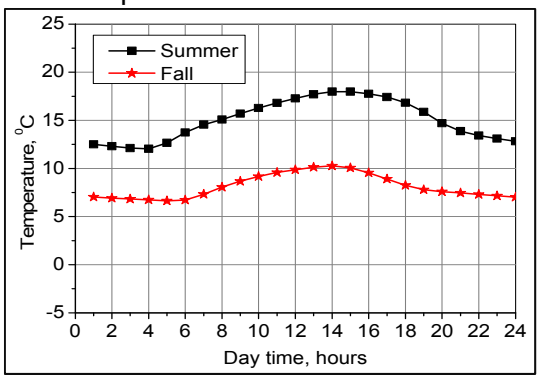

Figure (5-5, b2) Diurnal variation of temperature in summer and fall

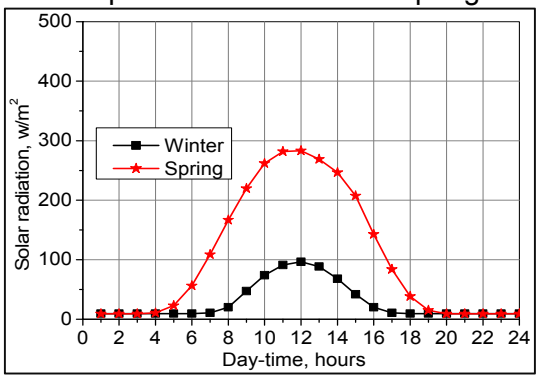

Figure (5-5, c1) Diurnal variation of solar radiation in winter and spring

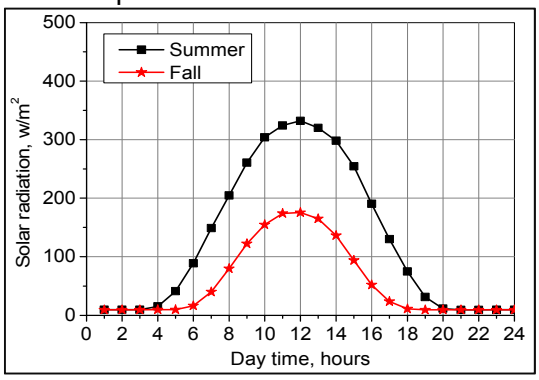

Figure (5-5, c2) Diurnal variation of solar radiation in summer and fall

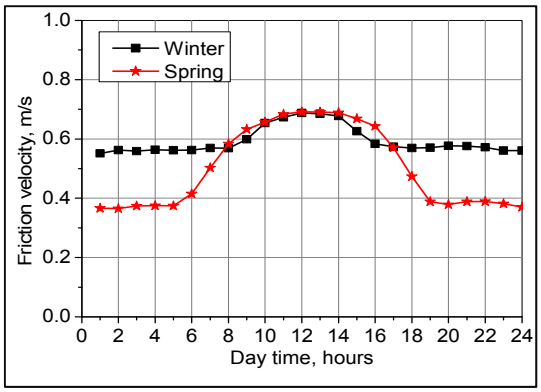

Figure (5-5, d1) Diurnal variation of friction velocity in winter and spring

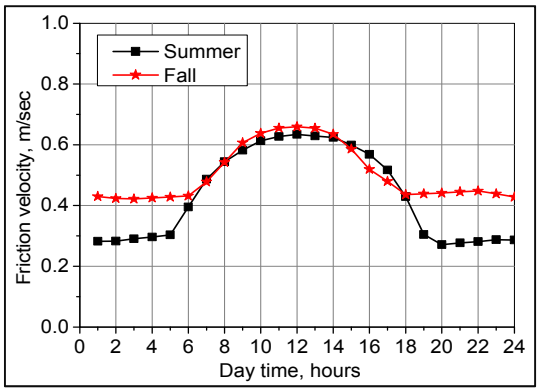

Figure (5-5, d2) Diurnal variation of friction velocity in summer and fall

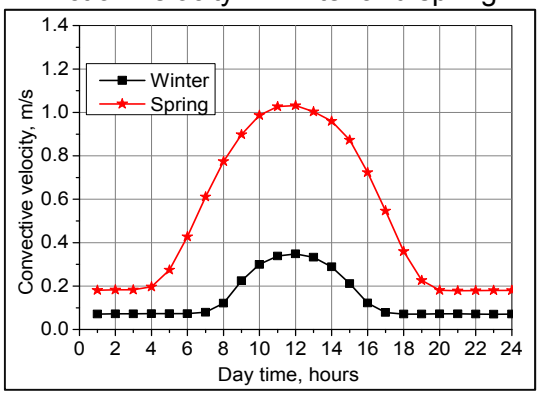

Figure (5-5, e1) Diurnal variation of convective velocity in winter and spring

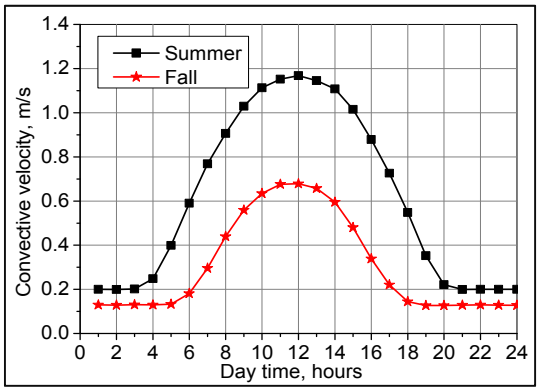

Figure (5-5, e2) Diurnal variation of convective velocity in summer and fall

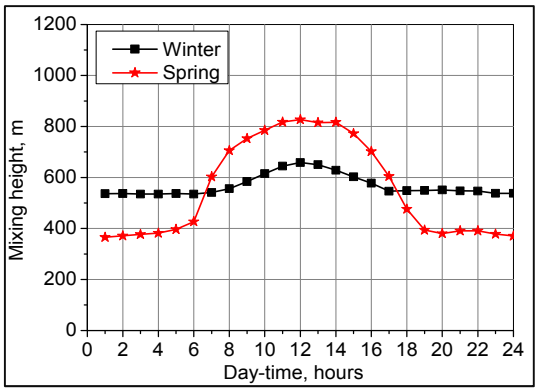

Figure (5-5, f1) Diurnal variation of mixing height in winter and spring

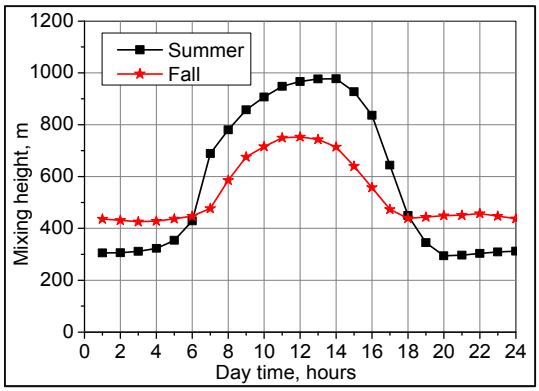

Figure (5-5, f2) Diurnal variation of mixing height in summer and fall

Figure (5-5) Diurnal variations of measured and estimated meteorological parameters

In order to examine the variation of mixing height with atmospheric stability categories, mixing height values were processed according to the stability classes from very unstable to stable conditions. The mixing height values were arranged in bands of 100 m class intervals versus the frequency distributions of mixing height bands as illustrated in Figure (5-6). The most significant feature of the distribution is the increase in frequency from lower to higher mixing heights with the change from unstable to stable atmospheric conditions. For example, during summer 2% of estimated mixing heights are below 800 m for stability class A, while at atmospheric

stability F all the estimated mixing heights are lower than 300 m. For stability A, mixing height ranges from 700 m to 1500 m for winter, spring and fall seasons, while there is 17% increase than 1500 m in summer. During all seasons, the main values of mixing layer at unstable C condition range from 600 m to 1000 m. There are gradual distributions of the maximum mixing heights for the three unstable category conditions (Pasquill–Gifford stabilities A, B and C). In summer season the frequency of mixing heights greater than 1500 m are 17%, for stability A, 5% for stability B, and 0% for stability C. For category D (neutral atmospheric conditions), the main range of estimated mixing heights locate from 100 m to 1200 m for all seasons. The heavy cloud-sky conditions in the winter cause prevailing of neutral stability D, in comparison with other seasons conditions. For stability class E, the frequency distributions of mixing height are very similar during all seasons; with most frequently of mixing heights occurring between 300 m to 1200 m. The Lower values of mixing height associate with F conditions are related mainly to ground-based stable layer (i.e. inversion layer). Existing of inversion layers hinder the dispersion pollutants vertically that increases the concentration of contaminations on the surface ground (Schnelle & Dey 2000).

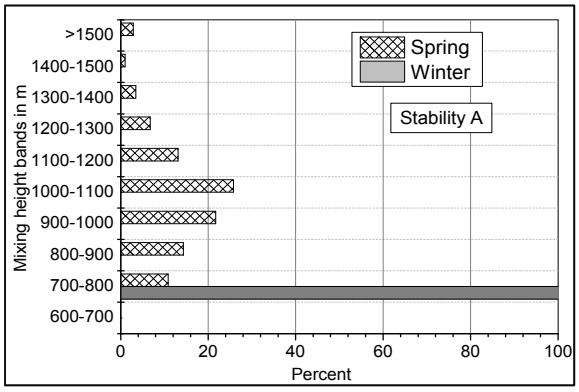

Figure (5-6, a1) Frequency distribution of mixing height at atmospheric stability A for winter and spring

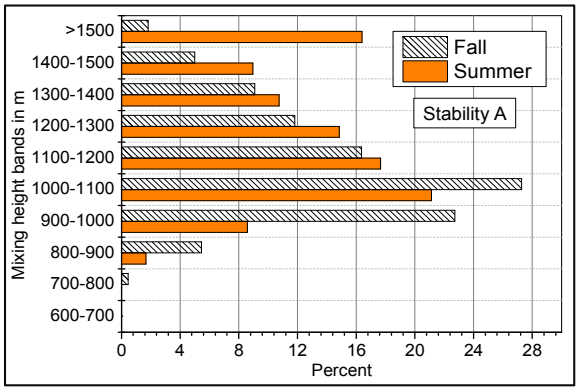

Figure (5-6, a2) Frequency distribution of mixing height at atmospheric stability A for summer and fall

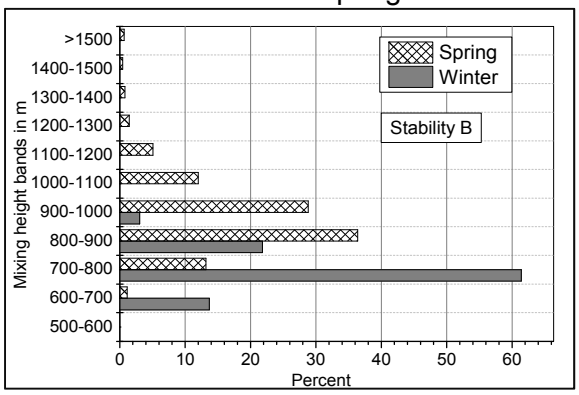

Figure (5-6, b1) Frequency distribution of mixing height at atmospheric stability B for winter and spring

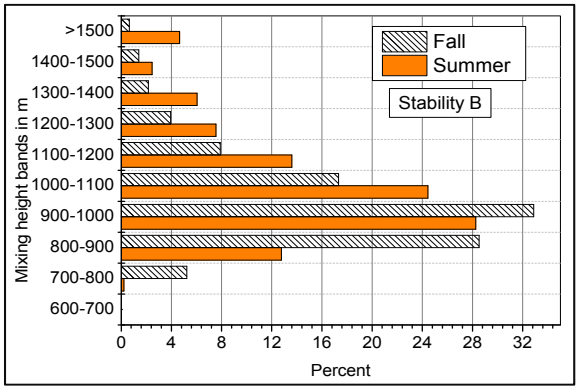

Figure (5-6, b2) Frequency distribution of mixing height at atmospheric stability B for summer and fall

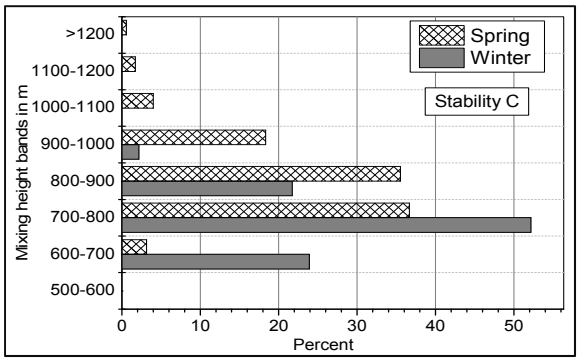

Figure (5-6, c1) Frequency distribution of mixing height at atmospheric stability C for winter and spring

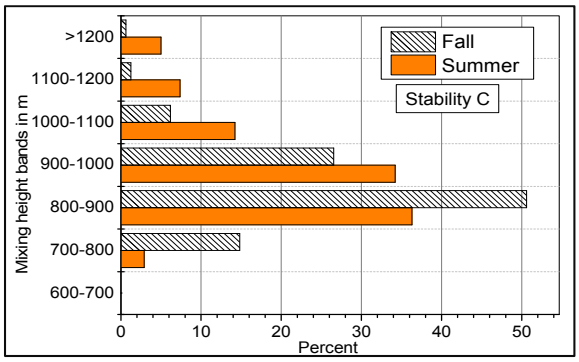

Figure (5-6, c2) Frequency distribution of mixing height at atmospheric stability C for summer and fall

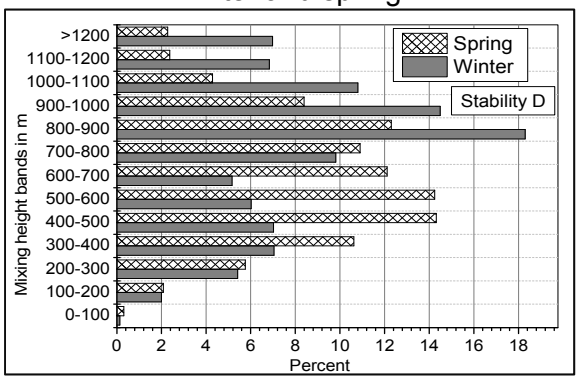

Figure (5-6, d1) Frequency distribution of mixing height at atmospheric stability D for winter and spring

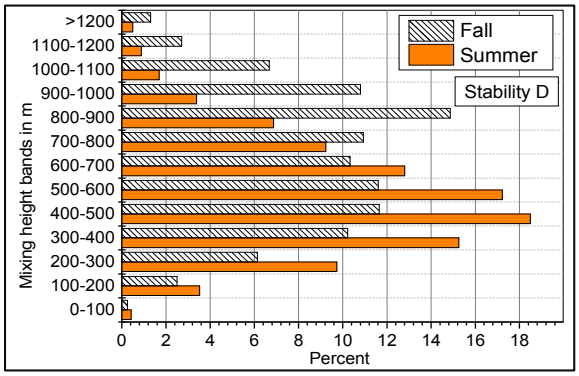

Figure (5-6, d2) Frequency distribution of mixing height at atmospheric stability D for summer and fall

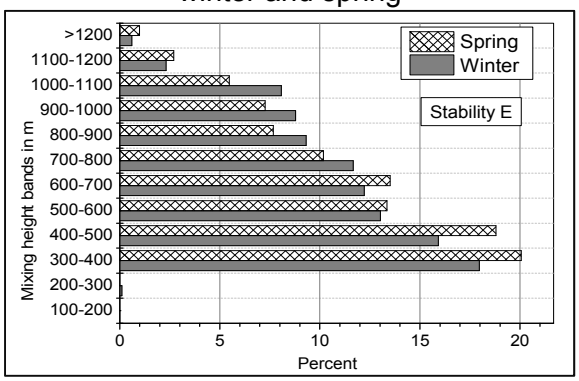

Figure (5-6, e1) Frequency distribution of mixing height at atmospheric stability E for winter and spring

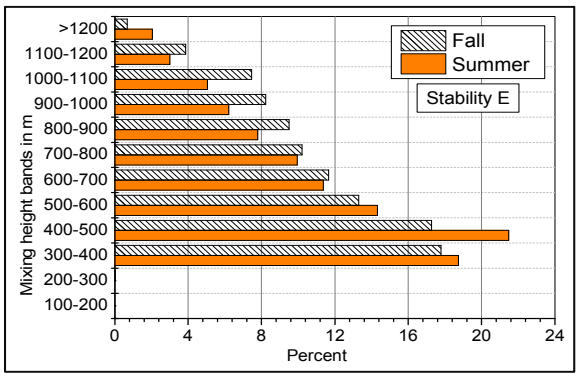

Figure (5-6, e2) Frequency distribution of mixing height at atmospheric stability E for summer and fall

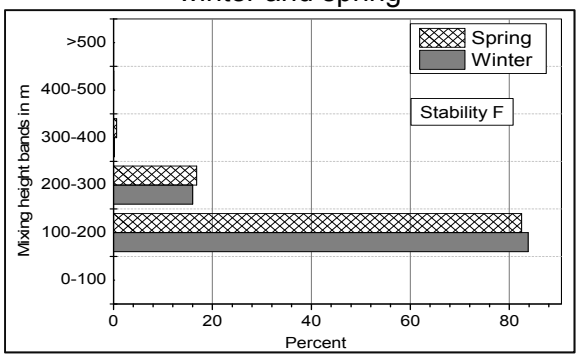

Figure (5-6, f1) Frequency distribution of mixing height at atmospheric stability F for winter and spring

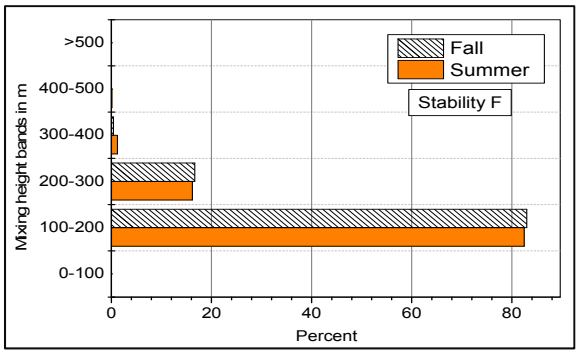

Figure (5-6, f2) Frequency distribution of mixing height at atmospheric stability F for summer and fall

Figure (5-6) Frequency distribution of mixing height as a function of atmospheric stabilities

The predicted mixing heights in Clausthal-Zellerfeld were also analyzed as a function of solar radiation and wind speed on the basis of day and night hours respectively as indicated in Figures (5-7) & (5-8). Solar radiation and wind speed are classified to five categories as given in Table (5-4). From Figure (5-7) we find that, the mixing height decreases with the decrease of solar radiation during the day hours. For the solar class A-R, 100% of the estimated mixing heights locate in the range from 800 m to 1500 m. There are 15%, 5%, 3%, 1%, and 0% of the mixing heights which are greater than 1500 m for the classes A-R, B-R, C-R, D-R, and E-R respectively. For solar radiation less than 200 W/m^2 (category E-R) the frequency of mixing height is 90% in the range from 100 m to 1000 m. It is obvious that the height of mixing layer is decreased with the decrease of the amount of radiation which reaches to the surface ground. To see the effect of wind speed values on the mechanical turbulent, mixing heights were analyzed based on wind speed categories only during night-hours. For wind speed category A-W (wind speed > 5 m/s) mixing height is usually greater than 900 m. While for category B-W (wind speed range is from 4 m/s to 5 m/s) mixing height values are in the range of 700 m to 1000 m. The frequency distributions of mixing height revealed that when wind speed is less than 2 m/s (category E-W), mixing height is mostly less than 400 m. Also, we can note that, heights of mixing layer are decreasing with the decrease of the value of wind speed.

Table (5-4) solar radiation and wind speed categories

solar radiation range W/m^2	Radiation Class code	Wind speed range, m/s	Wind Class code
>500	A-R	>5	A-W
400-500	B-R	4-5	B-W
300-400	C-R	3-4	C-W
200-300	D-R	2-3	D-W
<200	E-R	<2	E-W

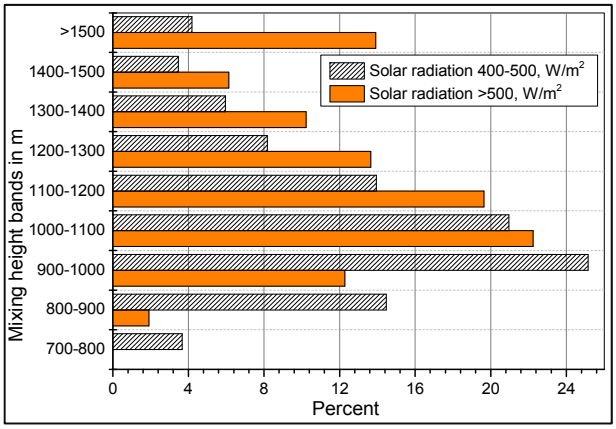

Figure (5-7, a) Mixing height bands at solar > 500 W/m^2 and (400 W/m2-500 W/m^2)

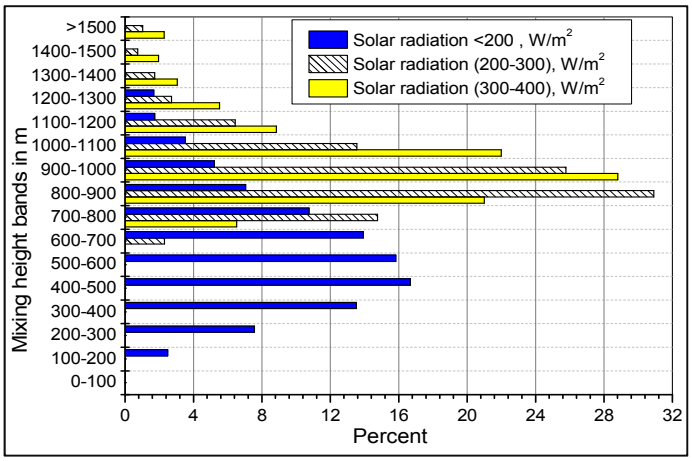

Figure (5-7, b) Mixing height bands at solar (300W/m^2-400 W/m^2), (200 W/m^2-300 W/m^2), and >200 W/m^2

Figure (5-7) Mixing height analyzed as a function of solar radiation during day-hours

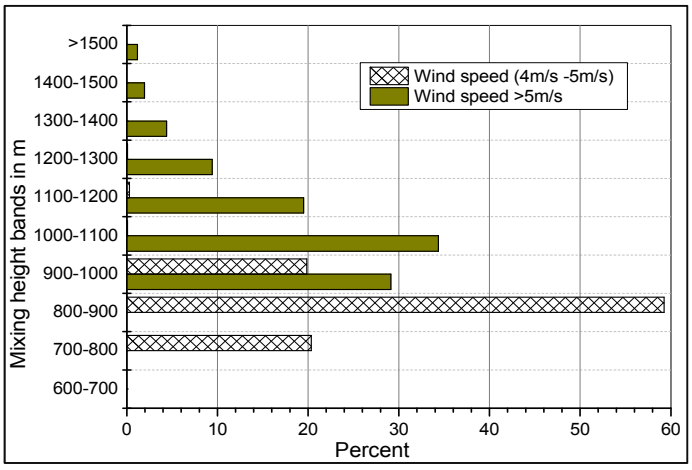

Figure (5-8, a) Mixing height bands at wind speed classes (4 m/s to 5 m/s) and V> 5 m/s

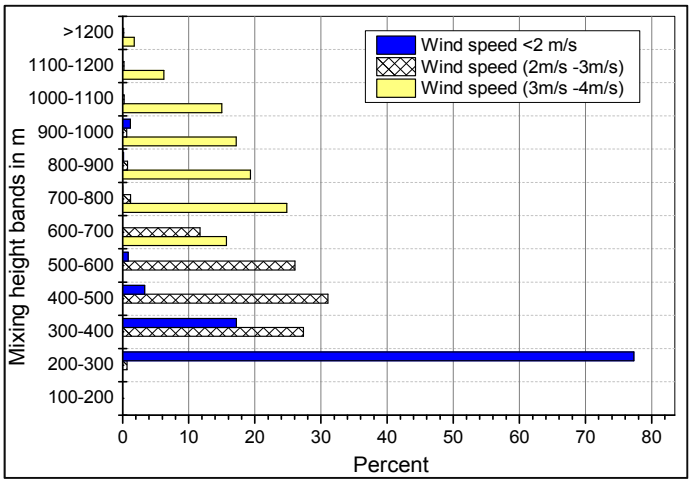

Figure (5-8, b) Mixing height bands at wind speed classes (3 m/s-4 m/s), (2 m/s-3 m/s), and >2 m/s

Figure (5-8) Mixing height analyzed as a function of wind speed during night-hours

5.4 Estimation of Deposition Velocity

The Auxiliary Meteorological Model designed to estimate hourly deposition velocity which is used in the air dispersion model. Deposition velocity estimated for Lead with particle diameter range from 0.01 μm to 5 μm, and the diurnal relation for winter and summer seasons is presented in Figure (5-9). A strong relationship is observed between deposition velocity and wind speed. During the day-hours, wind speed in winter (Figure (5-5, a)) is almost equal to that in summer. While wind speed values during nighttimes in winter is greater than that of summer. As a result, the estimated average deposition velocity during the day-hours in summer and winter seasons is equal at particle diameter 5 μm. While during the night-time, deposition velocity values in the winter are greater than that in the summer. Also a relationship between deposition velocity and particle diameter is given in Table (5-5). From the Table we note that, deposition velocities for particles range (0.1-0.7 μm) have lowest values. Deposition velocity for particle diameter 0.01 μm is 0.87 cm/s, while for diameter 0.3 μm, the deposition velocity is 0.02 cm/s. The deposition velocities obtained by this model are in the range of values determined by others (EPA, 1994).

Walcek et al., (1986) predicted deposition velocity fields for SO_2, sulfate and HNO_3 over eastern United States and southeastern Canada. For a 3-day springtime simulation, domain-averaged mid-day SO_2, sulfate and HNO_3 deposition velocities at a height of approximately 40 m were found to be 0.8 cm/s, 0.2 cm/s and 2.5 cm/s, respectively. At night, the deposition velocities were approximately 50%, 45% and 70% of the corresponding daytime values for SO_2, sulfate and HNO_3. Xu and Carmichael (1998) developed a dry deposition model to estimate SO2 and sulfate dry deposition velocities over nine land use types in Asia. Model results showed that the dry deposition velocity of SO_2 demonstrated strong seasonal and diurnal variability in summer, fall, and spring. In summer, the daytime velocity (in centimeters per second) for SO_2 in forests is 0.4, over cultivation is 0.2, on grassland is 0.5, and over ocean is 0.8. Nighttime values of SO_2 are two or three times less than daytime values. Generally, the averaged deposition velocities of sulfate were less than 0.1 over land, and were smaller than those of SO_2 in summer. The deposition velocity over ocean for sulfur dioxide was much larger than those over land, ranging from 0.3 cm/s to 1.2 cm/s. For sulfate, the model estimation was about 0.05 cm/s. Kumar et al., (2008) parameterized method based on local meteorological parameters to calculate dry deposition for S and N compounds on natural surfaces. The theoretical methods for calculation of dry deposition compounds had been outlined by which all the resistances responsible for deposition of gases and particles on vegetations could be determined. The

deposition velocity of SO_2, HNO_3, SO_4 and NO_3 obtained by this model was 0.32 cm/s, 0.74 cm/s, 1.16 cm/s, and 1.07 cm/s, respectively.

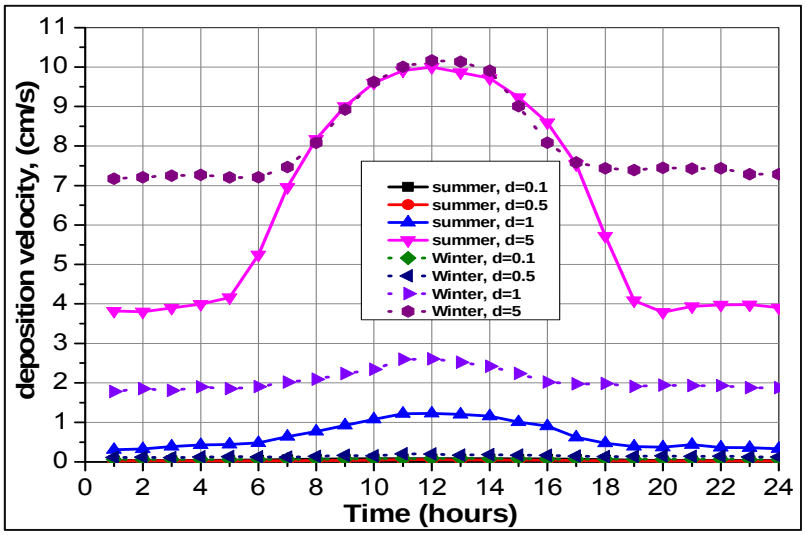

Figure (5-9) diurnal variation of deposition velocity at different particle diameter

Table (5-5) deposition velocity versus particle diameter

Diameter, (μm)	Deposition velocity, (cm/s)		Settling velocity cm/s
	Summer	Winter	
0.01	0.87	1.09	0.001
0.05	0.12	0.16	0.004
0.1	0.06	0.07	0.01
0.3	0.02	0.03	0.05
0.5	0.03	0.15	0.11
0.7	0.15	0.69	0.20
1	0.66	2.08	0.39
3	4.93	6.87	3.21
5	6.37	8.12	8.73

5.5 Evaluation of Auxiliary Meteorological Model

Model evaluation is possible when the observed mixing height is available. Observation of mixing height can be processed using wind and temperature profiles measurements. Methods of measuring wind profiles and potential temperature are not available within the study area. Therefore, the estimated mixing heights by other studies are compared with the results of Auxiliary Meteorological Model. Lena and Desiato (1999) evaluated nocturnal mixing heights derived from wind (SODAR) and temperature (RASS) profiles in the Milan urban area during spring and summer of year 1996. Average value determined by SODAR method was 302 m, while nocturnal mixing heights observed by RASS method was 299 m. Also mixing height was observed by Fatogoma and Jacko (2005) in urban airshed of Indianapolis,

USA, using upper air sounding data (radiosonde) in July, 1991. Maximum average mixing heights observed were from 1200 m to 2000 m during the day-hours, while the observed mixing height during the nights was less than 300 m. Delobbe et al., 2001 observed the mixing height at Bilthoven, Netherlands using LIDAR measurements. They found that, average mixing height during day-hours found to be 1100 m on August, 1994, and the nocturnal mixing height located between 200 m to 400 m. Also they estimated mixing height at 16:00 UT (Universal time) on July, 1990, by EUROS model over all Europe as shown in Figure (5-10). From the Figure we can see that, the general value of mixing height locates between 750 m to 1000 m over Germany. The average nocturnal mixing heights estimated by Auxiliary Meteorological Model is 300 m in summer and 500 m in winter as indicated in Figure (5-5, f1&f2). During day-times average estimated values is 1000 m in the summer and 800 m in the winter. These results match the estimated values of mixing heights by Delobbe et al., (2001). Despite of difference of the atmospheric conditions between Lena and Desiato, 1999 and Clausthal-Zellerfeld airshed, the estimated nocturnal mixing heights in summer are equal in both studies. The estimated mixing height is this study matches also the estimated values by Fatogoma and Jacko (2002). As illustrated in Figure (5-6), 95 % at stability A, 75% at stability B and 50% at stability C of the mixing height located between 1000 m to 1500 m during summer. From this discussion, we can say that, the mixing heights estimated by Auxiliary Meteorological Model are acceptable.

Ashrafi and Hoshyaripour (2010) developed a model to determine the atmospheric stability conditions using Pasquill–Gifford stability classification. They used the solar altitude, cloud cover and wind speed to determine the stability categories. As a case study, meteorological data of Mehrabad station in Tehran from 2000 to 2005 was applied to this model. Here, three different categories were considered to deduce the pattern of stability conditions. First, the total pattern of stability classification was obtained and results showed that atmosphere is 38.77%, 27.26%, 33.97%, at stable, neutral and unstable condition, respectively. It is also observed that days are mostly unstable (66.50%) while nights are mostly stable (72.55%). Khan and Simpson (1997) developed a one-dimensional model for the estimation of hourly mixing height values from routinely measured upper air and surface meteorological data on Brisbane airshed, Australia. In summer they found that, only 3% of the mixing height was below 400 m in stability class A, while for F, stability was 87%. The frequency distributions of mixing height revealed that, when wind speed is less than 1.5 m/s, about 75% of the mixing height values are less than 400 m.

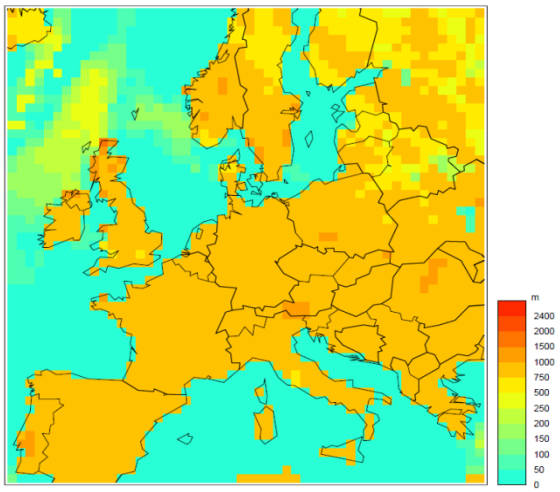

Figure (5-10) Height of mixing layer at 16 UT for July 30, 1990 (Delobbe et al., 2001)

5.6 Adjusted Wind Speed and Stack Tip Downwash

Wind speed at stack tip affects the plume rise and the dispersion of pollutants on the atmosphere. Therefore wind speed at the stack top has to be calculated from the values measured at the reference height (10 m from the base) using Equation (3-10). Figure (5-11) describes the adjusted wind speed at source tip for each stability class and season. The maximum wind speed calculated from the wind speed surface at the stack tip is given in Table (5-6). From the table we see that, some values of the wind speed at the top of stack exceed than the speed at which the plume release (9.95 m/s). If the ratio between stack emission velocities to the estimated wind speed at the stack top is less than 1.5, downwash effect occurs. The effect of wind downwash on the physical stack height (h_s) is calculated using Equation (3-11) and the result is presented in Table (5-6). From the table we see that, the stack height decreased sometimes to 67 m instead of the physical height 70 m in the neutral winter season. For extreme unstable and extreme stable conditions there is no effect of the downwash on the stack height. The effect of stack height is mostly in the neutral conditions.

Table (5-6) Effect of adjusted wind speed at the stack tip on the physical stack height (h_s)

Stability	Winter			Spring			Summer			Fall		
	Min.-hs	Av.-hs	Max.-us	Min.-hs	Av.-hs	Max.-us	Min.-hs	Av.-hs	Max.-us	Min.-hs	Av.-hs	Max.-us
A	70.0	70.0	2.0	70.0	70.0	3.4	70.0	70.0	3.4	70.0	70.0	2.5
B	70.0	70.0	5.7	69.9	70.0	6.8	70.0	70.0	6.6	70.0	70.0	6.1
C	70.0	70.0	6.0	69.7	70.0	7.0	68.6	70.0	8.7	69.8	70.0	6.9
D	66.6	69.7	15.1	67.2	69.9	12.6	68.2	70.0	9.5	67.6	69.9	10.9
E	69.0	69.9	7.9	69.0	69.9	11.1	69.0	69.9	7.8	69.0	69.9	7.9
F	70.0	70.0	5.8	70.0	70.0	5.8	70.0	70.0	5.8	70.0	70.0	5.8

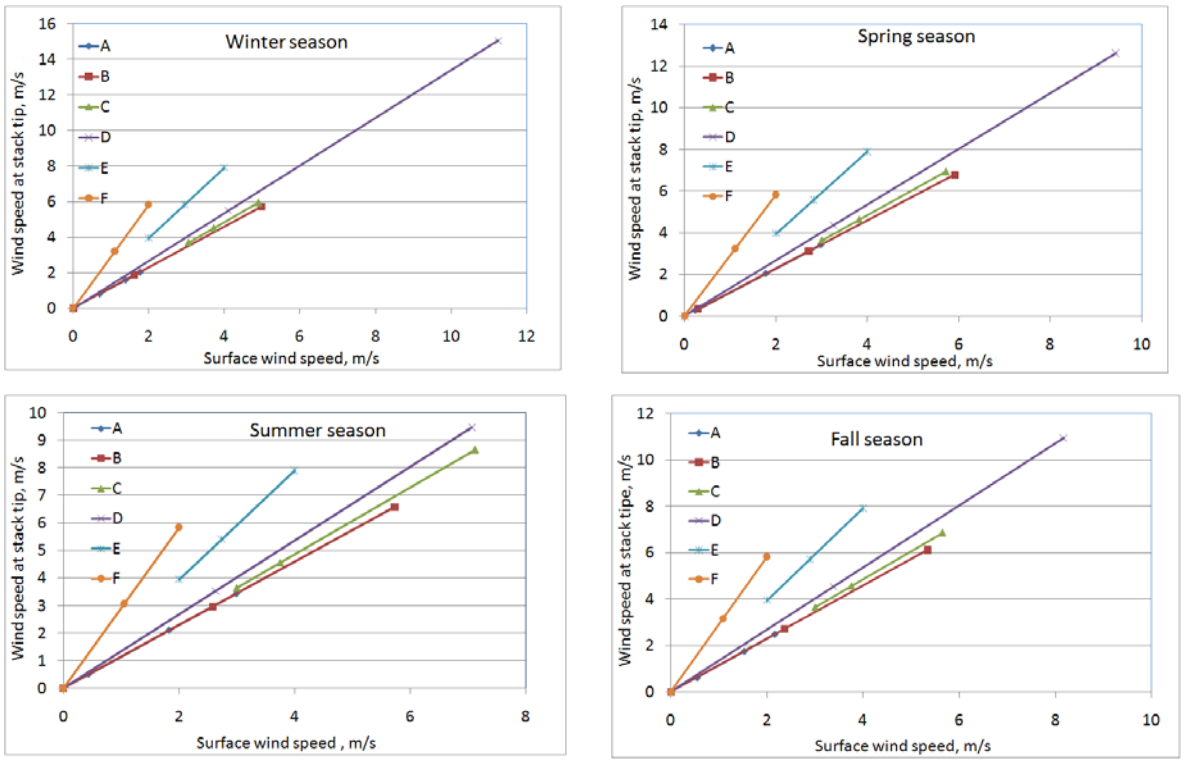

Figure (5-11) Adjusted wind speed at stack tip using measured surface wind speed

5.7 Estimation of Plume Rise

Estimation of plume rise is a critical parameter in studying the dispersion of pollutants from elevated sources. Briggs equations are used to calculate the plume rise in the generated Dispersion Plume Model as explained in section 3.3.4. Examination of these equations is discussed by calculating the plume height at different meteorological and atmospheric conditions. In Figure (5-12) the plume height is calculated at different temperature from -20 ^{o}C to +15 ^{o}C and wind speed from 0.5 m/s to 5 m/s. Briggs formulas give unique results at unstable and neutral conditions (from A to D classes) and same values at atmospheric stabilities E and F. From Figure (5-12,a) we note that, maximum plume height reaches to 516m at temperature -20 ^{o}C and wind speed of 0.5 m/s. While minimum plume rise (80 m) is existed at temperature 15 ^{o}C and wind speed 5m/s as indicated in Figure (5-12, e). According to the ambient temperature and stack exit temperature (32 ^{o}C), buoyancy rise or momentum rise is determined. When surface temperature exceeds than 15 ^{0}C the plume height is dominated by momentum force. The distance (x_f) at which the plume reaches to maximum height is calculated at different surface temperatures and presented in Figure (5-13). The figure indicates that, when the surface temperature is -20 ^{o}C the maximum distance x_f is 520 m, while at temperature +30 ^{o}C the maximum distance x_f is only 130 m. Also the plume rise is estimated at stable atmospheric conditions and presented in Figure (5-14). The calculation is applied at different surface temperatures and constant wind speed of

2.5 m/s. Also at stable condition buoyancy force is dominated when surface temperature is less than 15 ^{o}C. The distance x_f at which the plume reaches to the maximum height is depending on ambient temperature. At temperature -20 ^{o}C the distance x_f is 440 m, with plume height of 122 m, while at temperature +20 ^{o}C the distance x_f is 180 m, and the plume rise is 90 m.

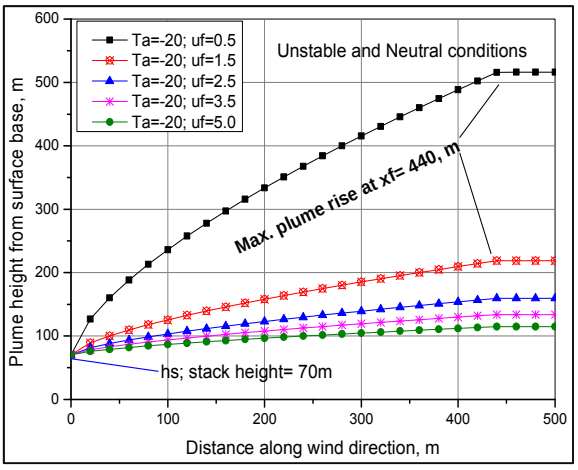

Figure (5-12, a) Plume rise calculated at different surface wind speeds and at temperature of -20 ^{o}C for unstable and neutral conditions

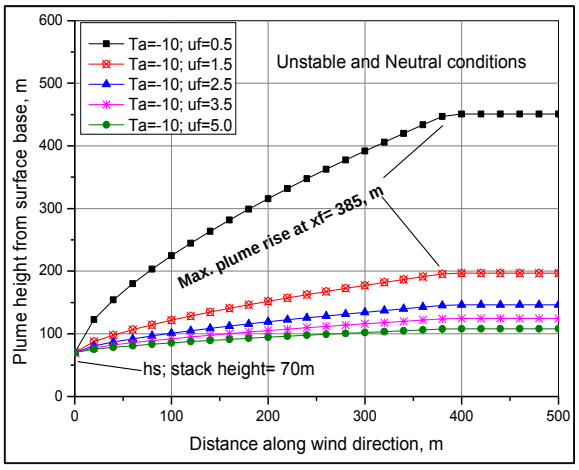

Figure (5-12, b) Plume rise calculated at different surface wind speeds and at temperature of -10 ^{o}C for unstable and neutral conditions

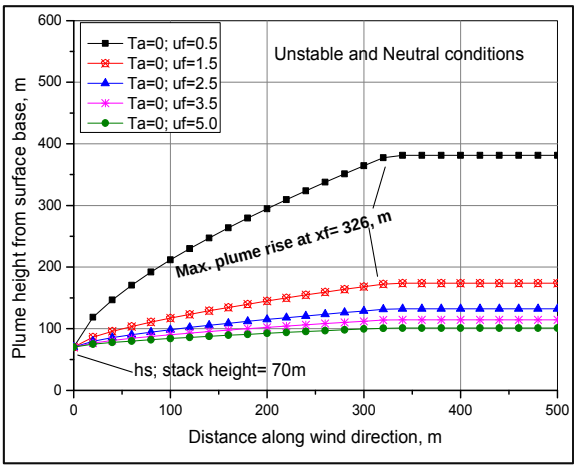

Figure (5-12, c) Plume rise calculated at different surface wind speeds and at temperature of 0 ^{o}C for unstable and neutral conditions

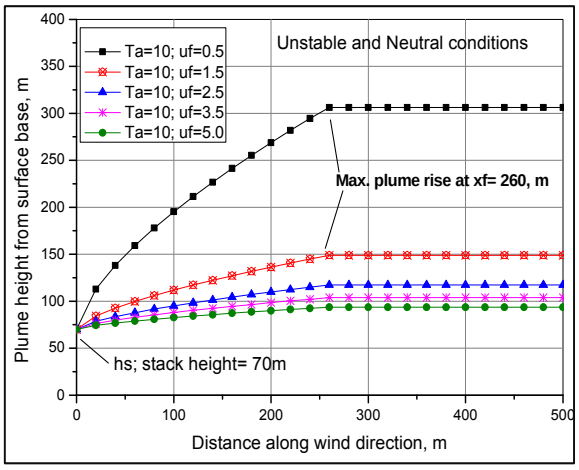

Figure (5-12, d) Plume rise calculated at different surface wind speeds and at temperature of 10 ^{o}C for unstable and neutral conditions

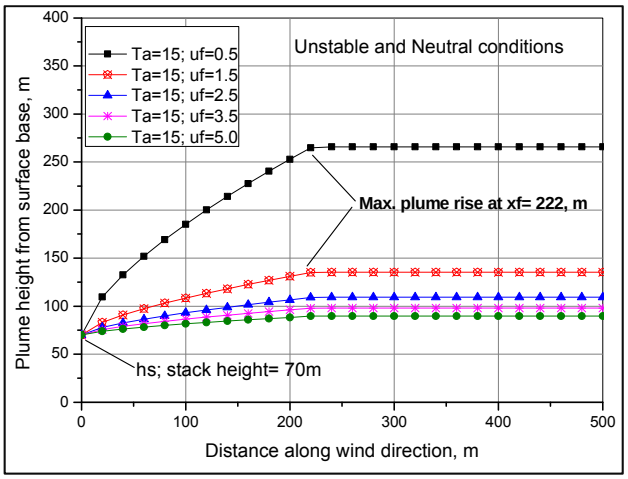

Figure (5-12, e) Plume rise calculated at different surface wind speeds and at temperature of 15 ^{o}C for unstable and neutral conditions

Figure (5-12) Plume rise calculated at different wind speeds and ambient temperatures and for unstable and neutral conditions

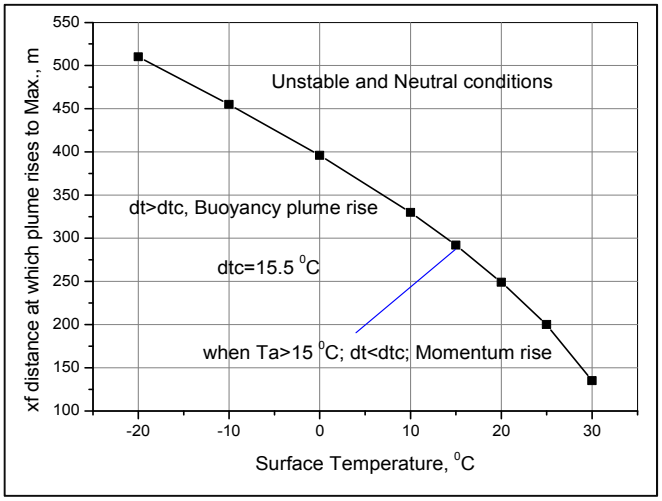

Figure (5-13) Relation between distances x_f at which Plume rise reach to maximum height and surface temperature

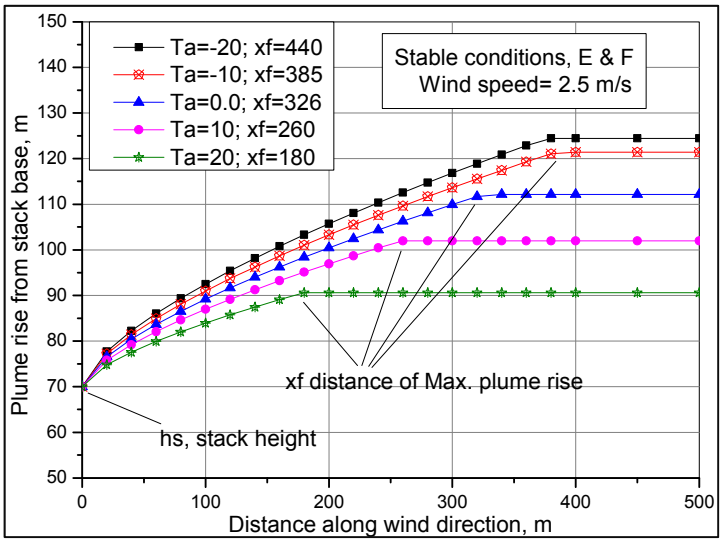

Figure (5-14) Plume rise at stable atmosphere estimated at different surface temperature

5.8 Modeling the Terrain Effect

Within a level terrain, the plume centerline travels horizontally in the atmosphere. While existence of complex terrain at the receptor locations effects the plume path. Many models (explained in Ch.3 section 3.3.5) are examined by the Dispersion Plume Model to adjust plume centerline height due to the terrain effect. Figure (5-15) presented source elevation, receptor elevations, plume rise at level terrain and the adjusted plume height due to terrain effect. The straight line without any marks denotes the plume height for the horizontal level. Model (1) and model (2) give adjusted plume height less than that of level terrain which is not logical. Also they give implausible values in some locations. Model (3) gives good results for locations having elevation greater than the source elevation. But it presents implausible values at receptors less than source elevation. This model is suitable only for receptors which greater elevation than the source elevation. Model (4) estimates plume rise similar to horizontal terrain. Model (5) produces best adjusted plume heights. It gives the most logical calculations than any other model; therefore this model will be used in all the next calculations. Different adjusted plumes which are generated using model number (5) at unstable, neutral and stable atmospheric conditions are presented in Figure (5-16). The estimations are applied at constant wind speed of 2.5 m/s and constant surface temperature of -5 ^{o}C. For the horizontal terrain, unstable conditions give plume rise of 640 m above sea level, while stable condition give the lowest value with plume height of 615 m above sea level.

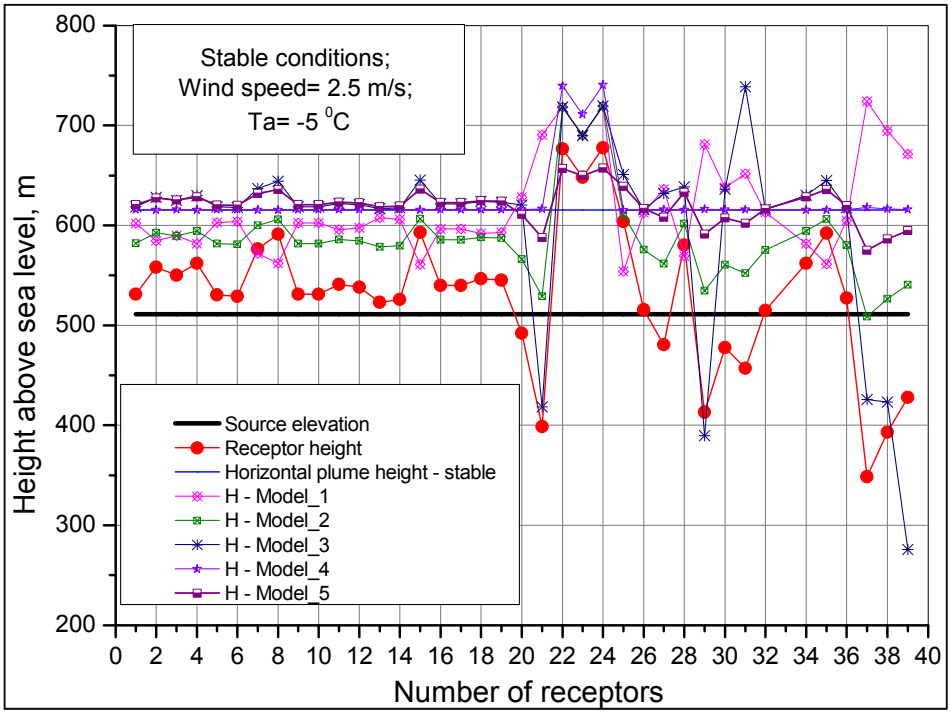

Figure (5-15) many models used to adjusted plume height due to the terrain effect

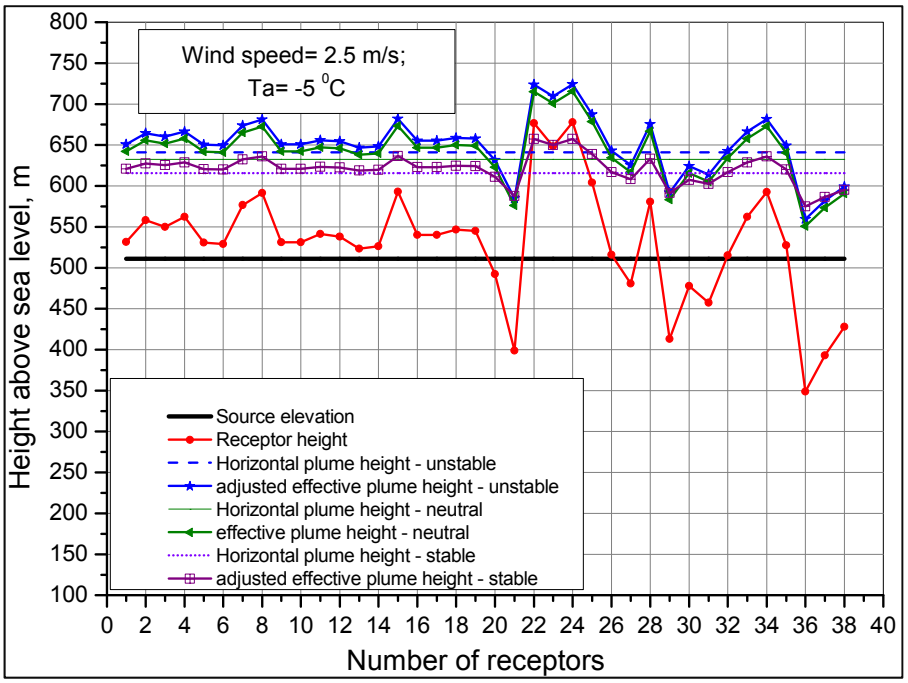

Figure (5-16) Adjusted plume height due to the terrain effect using Model No. 5

5.9 Concentrations at Different Meteorological Conditions

Meteorological parameters affect the estimated concentration of pollutants at a receptor location. Relations between concentration and atmospheric stability, ambient temperature, wind speed, and mixing height are examined by the Dispersion Plume Model. Figure (5-17) represents the relationship between pollutant concentrations at different ambient temperatures. The estimation is applied at C atmospheric conditions and at constant wind speed of 2.5 m/s with surface temperatures range from -15 °C to 25 °C. From the figure, we note that, the concentration increases with increase of the temperature. This is the effect of the temperature on the plume height as indicated in Figures (5-12 & 5-14). As the temperature increases; the height of plume decreases which in turn increases the concentrations of the pollutants on the surface earth. Peak concentration of 70 $\mu g/m^3$ is calculated when the temperature is 25 °C at a distance of 2 km from the source. While lowest concentration is obtained when surface temperature is -20 °C with a peak value of 45 $\mu g/m^3$. The concentration decreases with the increase of the distance from pollutant source. For all surface temperatures, the concentration reaches to 10 $\mu g/m^3$at distance 10 km from the source. Also the relationship between pollutant concentration with wind speed and mixing height is examined at different distances from the source. Figure (5-18) illustrates the relationship between the estimated values of pollutant concentrations and the measured surface wind speed. There is a direct proportion between the wind speed and the modeled concentrations of contaminations. At calm atmosphere the plume has chance to rise vertically more distances than windy conditions, which decreases the settled

pollutants on the ground. For windy atmosphere the mechanical turbulence is increased hence the plume disperses vigorously which increases the concentration at the receptor. In Figure (5-18), when wind speed is 0.5 m/s, the estimated concentration is very small. While at wind speed 5.5 m/s and 4.5 m/s the concentration reaches to peak value of 85 $\mu g/m^3$. At wind speed 2.5 m/s, the model computes pollutant concentration of 60 $\mu g/m^3$ at 2.5 km from the source.

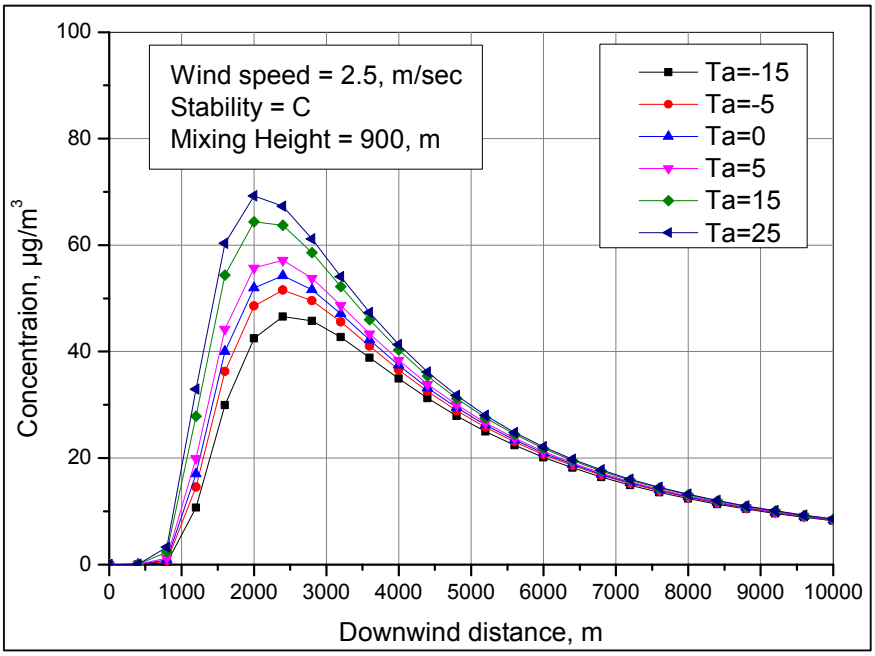

Figure (5-17) pollutant concentrations estimated at different ambient temperatures

Mixing height resembles the depth in which the pollutants disperse vertically. At small values of mixing height, the plume has small volume to disperse on it which increases the pollution on the ground, especially when the inversion layer exists near the ground (extreme stable atmosphere). The relation between mixing height and concentration of pollutants is indicated in Figure (5-19). The estimation is applied using different mixing heights from 1200 m to 200 m and constant meteorological conditions (B atmospheric stability, surface temperature 10 ^oC and wind speed 2.5 m/s). Mixing height of 200 m gives the greatest concentration value of 360 $\mu g/m^3$at a distance of 1.5 km from the source. The effect of mixing heights on the concentration decreases after H_m increased than 500 m. Therefore we see that the concentration at mixing heights from 600 m to 1200 m is almost same at all distances from the source.

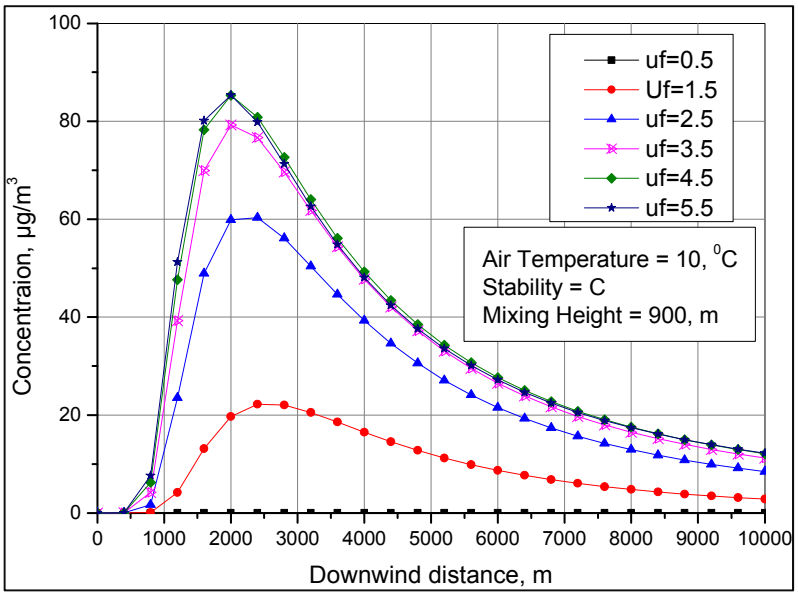

Figure (5-18) Relation between wind speed and concentrations along wind direction

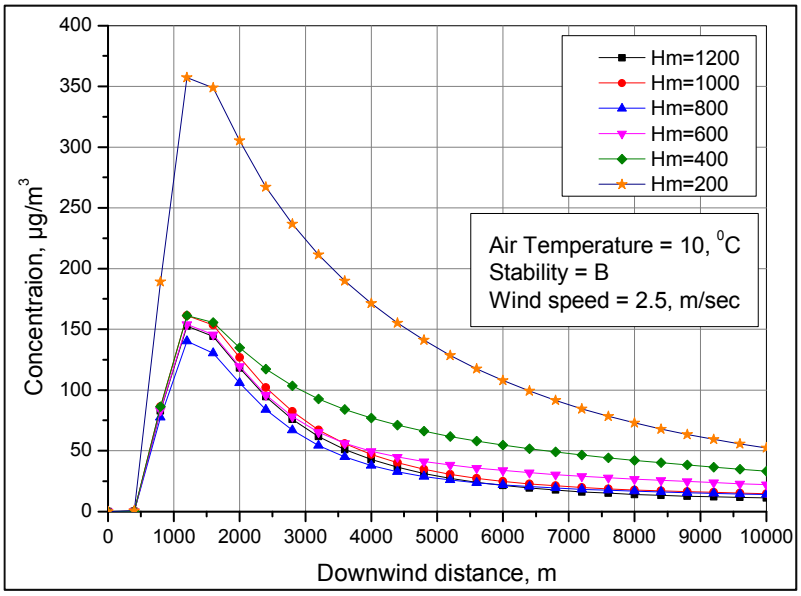

Figure (5-19) Pollutant concentrations at different mixing heights

5.10 Results of the Generated Dispersion Plume Model

Spatial distribution of Pb in forest soil is generated by geostatistical analysis as discussed in Ch. (4). Sites of known soil samples are chosen also to estimate the Pb concentrations via the generated Gaussian Dispersion Plume Model and considered as receptors. The estimated values of Pb by the model are compared with the values of soil samples. The available meteorological parameters are hourly measured data for six years (from 2004 to 2009) taken in Clausthal-Zellerfeld airshed. Therefore the created Dispersion Plume Model can calculate the Pb concentrations emitted from Clausthal-Zellerfeld smelter, at each selected location for the mentioned period. Emission characteristics of Clausthal-Zellerfeld smelter are indicated in Table (1-1). The feeding hourly meteorological data include

atmospheric stability, wind direction, wind speed, mixing height, ambient temperature, deposition velocity and atmospheric pressure. The distance between a source and a receptor is function of the time. As the time changes the wind direction changes too which affects the calculated distances between the source and the receptor. Also the wind speed varies with the time which affects the calculated concentration at any receptor. Wind speed and its direction perhaps change every minute. Therefore, the generated Gaussian plume model assumes the averaging time to be one hour, during this time the model assumes the wind direction and wind speed constant. The model transfers from the original coordinates of the receptor locations to the wind direction based on Equations (5-1) and (5-2) as indicated in Figure (5-20).

$$x_w = (x_r - x_s)\sin(W_d) + (y_r - y_s)\cos(W_d) \quad (5\text{-}1)$$

$$y_w = (y_r - y_s)\sin(W_d) - (x_r - x_s)\cos(W_d) \quad (5\text{-}2)$$

Where x_w is number of meters from the source to the receptor along wind direction, y_w is number of meters perpendicular to the wind direction, x_r and y_r are coordinate point of the receptor, x_s and y_s are the coordinates of the source, and W_d is the wind direction. If the calculated distance along wind direction x_w is less than 10 m the model puts the concentrations as zero value.

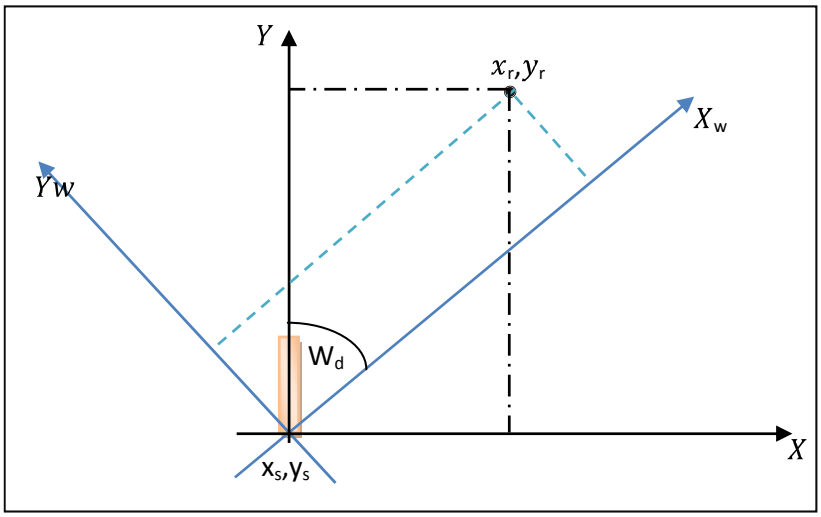

Figure (5-20) Transforming from original coordinates to wind direction

The Dispersion Plume Model estimates the concentrations of Pb particles emitted from Clausthal-Zellerfeld smelter on the atmosphere near to the surface ground in mg/m^3. The calculated values are generated for each season based on the hourly meteorological parameters for six years (from 2004 to 2009). The smelter had been working for all the times of year except in summer. It had been working only for one month in summer and the other time was spent for maintenance. The

model computes hourly concentrations of Pb during the available meteorological data. For example in summer, the model estimates 4464 Pb values at each location (24 hours multiplied with 31 days multiplied with 6 years). Results of calculations at each receptor for the other seasons are extreme values. Table (5-7) gives the values of calculations in each season at each selected receptor location. The modeled concentration of Pb is summed up to give the total Pb value for 6 years. To estimate concentration for longer time, the 6 years concentrations are multiplied by the required time period. The Pb concentrations are estimated at 115 locations around Clausthal-Zellerfeld smelter. The model calculates Pb in the air near to the surface and these Pb particles will settle down on the soil. Assuming the settled particles penetrate the soil to 20 cm depth. Also it is assumed that 3 m air height of the calculated concentrations will deposit on the soil as illustrated in Figure (5-21). If the estimated concentration at a receptor is 1000 mg/m^3, then the total concentration for 3 m^3 is 3000 mg Pb. The average value of bulk soil density is 1.3 g/cm^3 (i.e. 1300 kg/m^3). According to this density, the weight of 0.2 m3 of soil equals to 260 kg. Then 3000 mg of Pb will mix with 260 kg of soil. Assuming the deposited particles of Pb distributes homogenously within the soil particles. The weight of settled particles is very small relative to the soil weight and can be neglected. Then the concentration of deposited Pb into the soil is 3000 mg (Pb)/260 kg (soil) which is equal to 11.54 mg/kg. According to the previous procedures, the estimated concentrations are converted from mg/m^3 in the atmosphere to mg/kg in soil. Table (5-8) gives some statistics of the estimated concentrations in mg/kg for all seasons of different years. From Table (5-8) we find that, average value of Pb concentrations, predicted by the model is 305.89 mg/kg for 400 years, while mean value of measured soil samples is 1878.12 mg/kg. Most of the Pb concentrations are obtained during fall season. At the selected 115 locations around Clausthal-Zellerfeld smelter, the Pb concentrations are modeled at different period of years. Comparison between the modeled Pb values and the measured concentrations were examined by geostatistical methods. Spatial distribution of the estimated concentration by the model is generated using Ordinary Kriging. These predicted surfaces are developed for the results of 400 years and the results are presented in Figures (5-23) to (5-27).

Table (5-7) Number of model calculation at each location

season	working days along 6 y	number of model calculations
Summer	186	4464
Winter	542	13008
Spring	552	13248
Fall	546	13104
Total	1826	43824

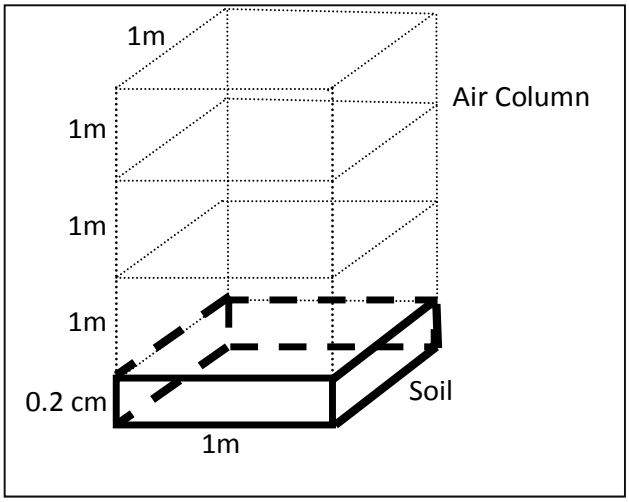

Figure (5-21) Diagram of settling particles from the air into the soil

Table (5-8) Statistics of the Pb concentrations estimated by air dispersion modeling

No. of Years	Season	Min.	Average	Max.	std
6	Summer	0.0000	0.11	1.15	0.20
	Winter	0.0001	0.15	2.12	0.39
	Spring	0.0005	1.49	29.33	4.17
	Fall	0.0004	2.96	70.70	8.83
	Total	0.0010	4.71	70.84	9.34
60	Summer	0.0001	1.06	11.46	2.01
	Winter	0.0012	1.54	21.22	3.89
	Spring	0.0051	14.90	293.34	41.69
	Fall	0.0035	29.56	706.96	88.27
	Total	0.0100	47.06	708.40	93.40
120	Summer	0.0003	2.11	22.93	4.03
	Winter	0.0025	3.09	42.45	7.79
	Spring	0.0103	29.81	586.67	83.37
	Fall	0.0071	59.12	1413.92	176.54
	Total	0.0201	94.12	1416.80	186.80
400	Summer	0.001	6.86	74.51	13.09
	Winter	0.0008	10.03	137.95	25.31
	Spring	0.033	96.87	1906.69	270.96
	Fall	0.023	192.13	4595.24	573.76
	Total	0.065	305.89	4604.61	607.10
Measured soil values of Pb by sampling		155.00	1878.12	16000	2199.32

Also the spatial distribution of the same area is generated using the values of soil samples as given in Figure (5-28). A significant concentration is observed towards the north direction at summer and winter seasons. The smelter had been working only for one month during the summer, therefore the concentrations in the summer is very small relative the other seasons as illustrated in Table (5-8). For spring, Pb estimated values take the direction of North-West while for fall season; it takes the direction of North-East. Figure (5-22) presents the histogram of the wind

direction for all seasons, for the modeled hours. From this histogram we find that, 35% of the wind direction at spring is orientated between 270^{o} and 360^{o}. While there is 49 % of wind direction, in fall, located between 0^{o} and 60^{o}. The predicted Pb values of pollutants, at fall, are extreme in comparison with other seasons as indicated in Table (5-8). Therefore the fall calculation has strong weight on the total modeled concentrations as presented in Figure (5-27). From Figure (5-28) we note that, high concentrations of sampled Pb are located in the front of Clausthal-Zellerfeld smelter. Significant digit is observed towards the North-West direction in this figure, which is the same direction of fall modeled results. From this discussion, we can conclude that, the modeled concentrations are not the same as today values, but it can give an indication about its sources. In general we can say that, the modeled concentrations from Clausthal smelter are small relative to the values of today soil samples. Difference between modeled and measured Pb contaminations is due to many reasons. The first one is the assumption of Clausthal-Zellerfeld smelter data. The smelter data (Table (1-1)) used into the dispersion model is valid only for the period from 1950 to 1976. While the working time of Clausthal-Zellerfeld smelter is from 1554 to 1976. We have no accurate data about the smelter dust emissions before 1920. During old years the smelter had no filters; therefore the expected emission was huge during these periods. Also the stack height perhaps was not more than 10 m above the ground, which created extreme local pollutions. Moreover the emissions from roasting and smelting processes were separated, which means that many contaminations sources in the same place had been existed.

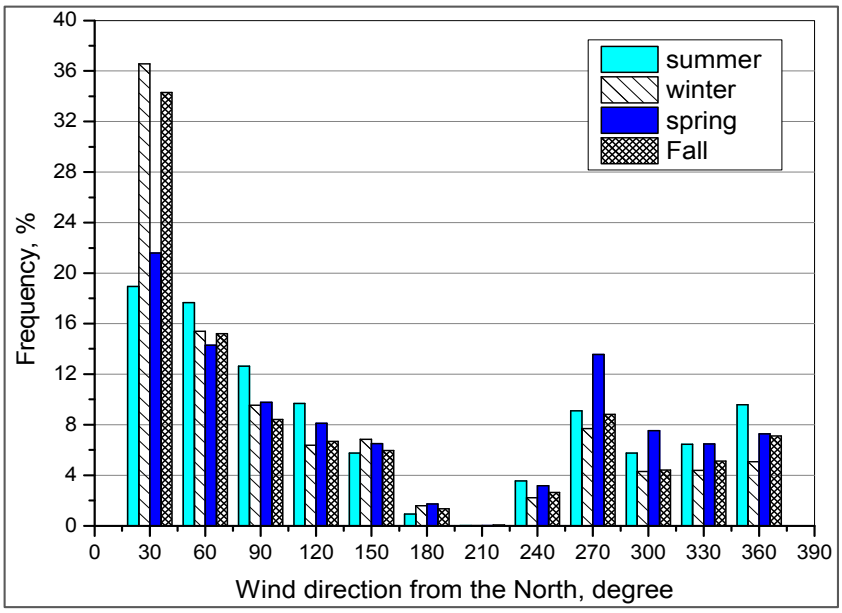

Figure (5-22) Histogram of wind direction at each season of the modeled data

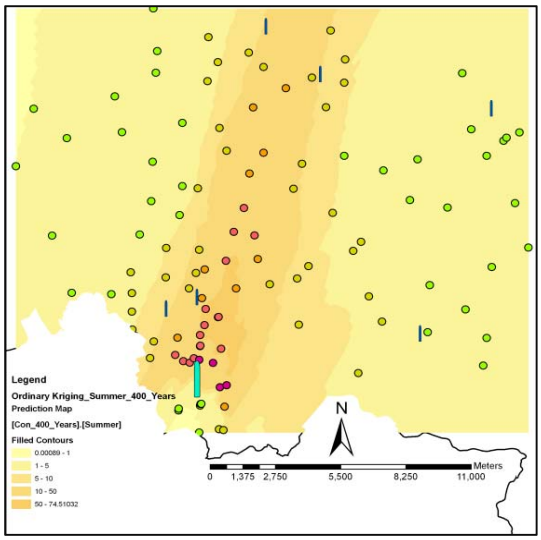

Figure (5-23) Modeled of Pb values by air dispersion modeling in summer

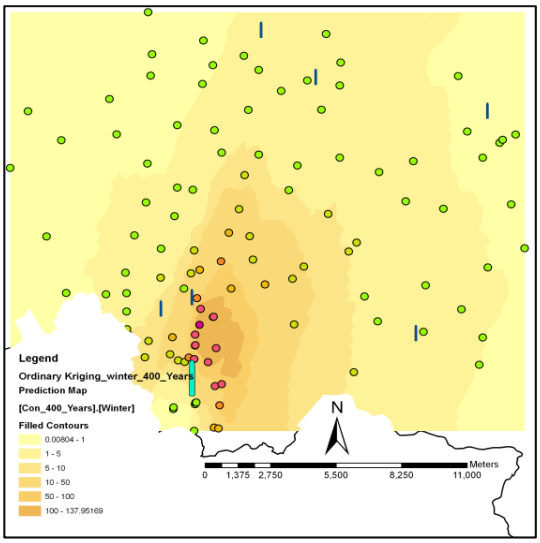

Figure (5-24) Modeled of Pb values by air dispersion modeling in winter

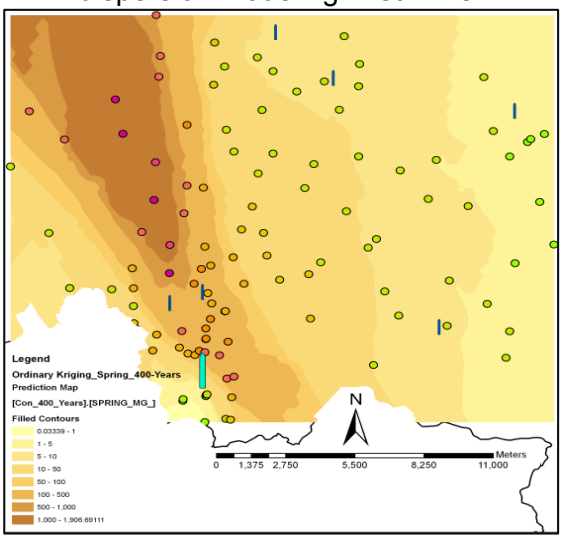

Figure (5-25) Modeled of Pb values by air dispersion modeling in spring

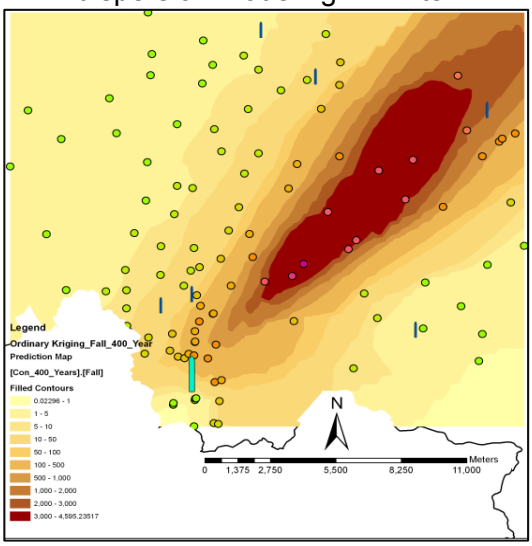

Figure (5-26) Modeled of Pb values by air dispersion modeling in fall

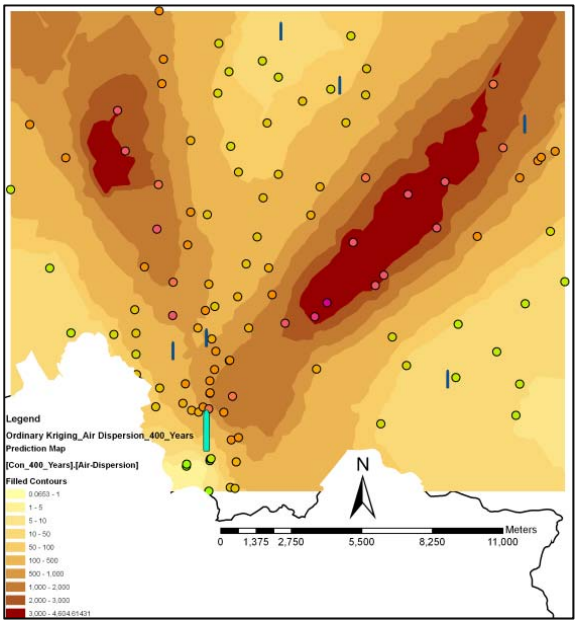

Figure (5-27) Total air dispersion model

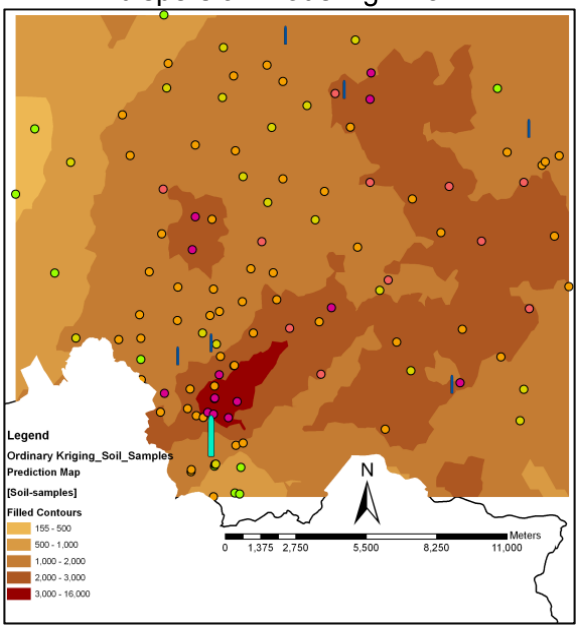

Figure (5-28) Spatial distribution of measured soil sample

Another reason for the difference between modeled and sampled Pb values is the transportations of minerals from mining sites to the smelter locations. Also many smelters had been built around the investigated area. The most important smelters were at Lautenthal, Altenau, and Wildemann smelters. The passive effect of these smelters was extreme also on the neighborhood (Peucker, 1958; Segers-Glocke & Witthöft, 2000; Ernst et al., 2004). Large areas of vegetations had been destroyed due to the effect of emissions especially by SO_2 contaminations. Schroeder and Reuss (1883) concluded the amount of emitted SO_2 to the air from Clausthal-Zellerfeld, Lautenthal, and Altenau smelters. Some of these values are given in Table (5-9). We can see that the amount of SO_2 increases from old time to new time because the increase of processed minerals. Also, we can conclude that, the dust emissions from theses smelters were enormous. The table demonstrates the intensively negative effect of the Upper-Harz smelters on the study area. Also we can say that, Clausthal-Zellerfeld smelter contributes partly and not totally on the studied soil contaminations.

Table (5-9) Sulfur amount emitted into air from Upper-Harz smelters in *Ctr.

Year	Clausthal-Zellerfeld Smelter	Lautenthal Smelter	Altenau Smelter
1851/52	9436	5432	6774
1854/55	9852	5402	7381
1855/56	9114	4989	7309
1859/60	10250	5044	7803
1860/61	9766	4616	7507
1865/66	11356	5742	8455
1870	18040	7652	8468
1873	23882	7182	3293
1875	26964	5498	7023
1877/78	26250	6066	8434
1878/79	24125	5904	8425

Ctr.: an old Germany weight unit which equal to 500 pound-mass (nearly 45.4 kg)

5.11 Evaluation of Dispersion Plume Model

The generated Dispersion Plume Model is evaluated by a published model known as Industrial Source Complex Model (ISC3) Dispersion Model as illustrated in Figure (5-28). The model is attached in the book of *"Atmospheric Dispersion Modeling Compliance Guide"* (Schnelle & Dey 2000). The model was designed to estimate the concentrations of gases emitted from a single source. The same parameters and same data are fed into both ISC3 model and the developed Dispersion Plume Model. The concentrations estimated by Dispersion Plume Model were done for gases and particulate matters as illustrated in Figures (5-29) and (5-30) respectively. The parameters of Clausthal-Zellerfeld parameters were used as feeding data. For both models we note that the estimated concentrations are zero at

distances less than 500 m from the source. Maximum values estimated from both models are existed at distances from 1 to 1.5 km from the source. The estimated values decrease with increase the ambient temperatures. In case of particulate matters the estimated values from the generated model are less than that estimated by ISC3 model as illustrated in Figure (5-30). While the concentrations estimated by both models along downwind distances are similar for gases as indicated in Figures (5-28) and (5-29).

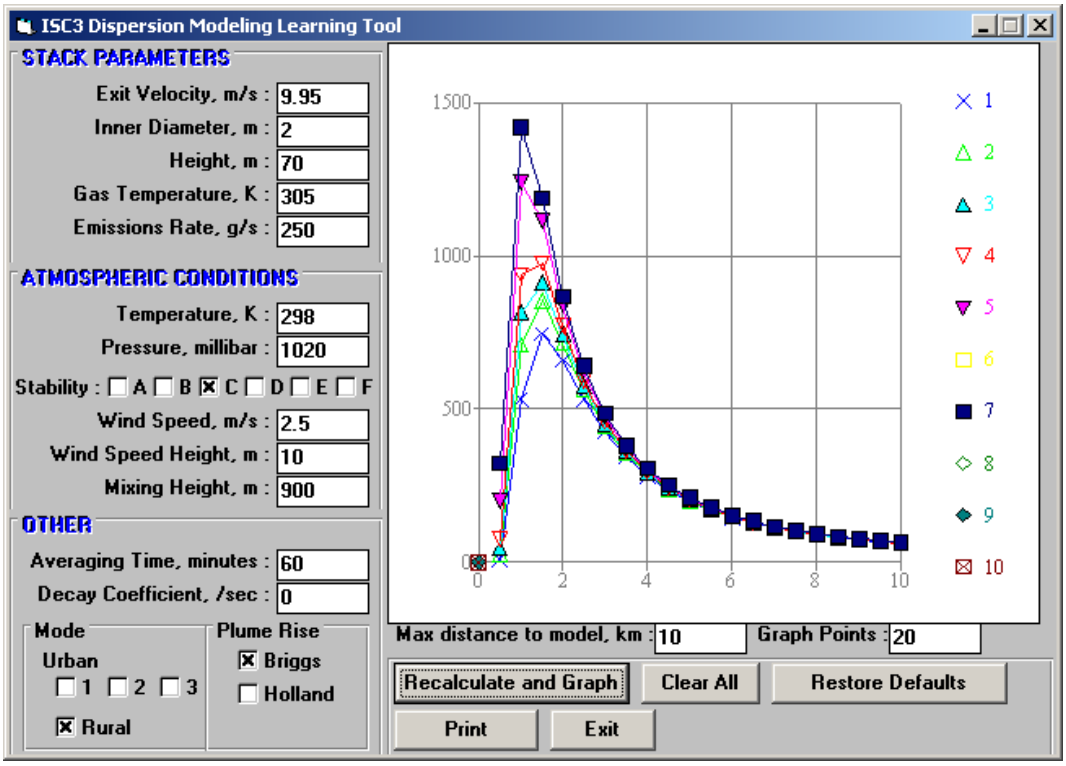

Figure (5-28) results of ISC3 Dispersion Model

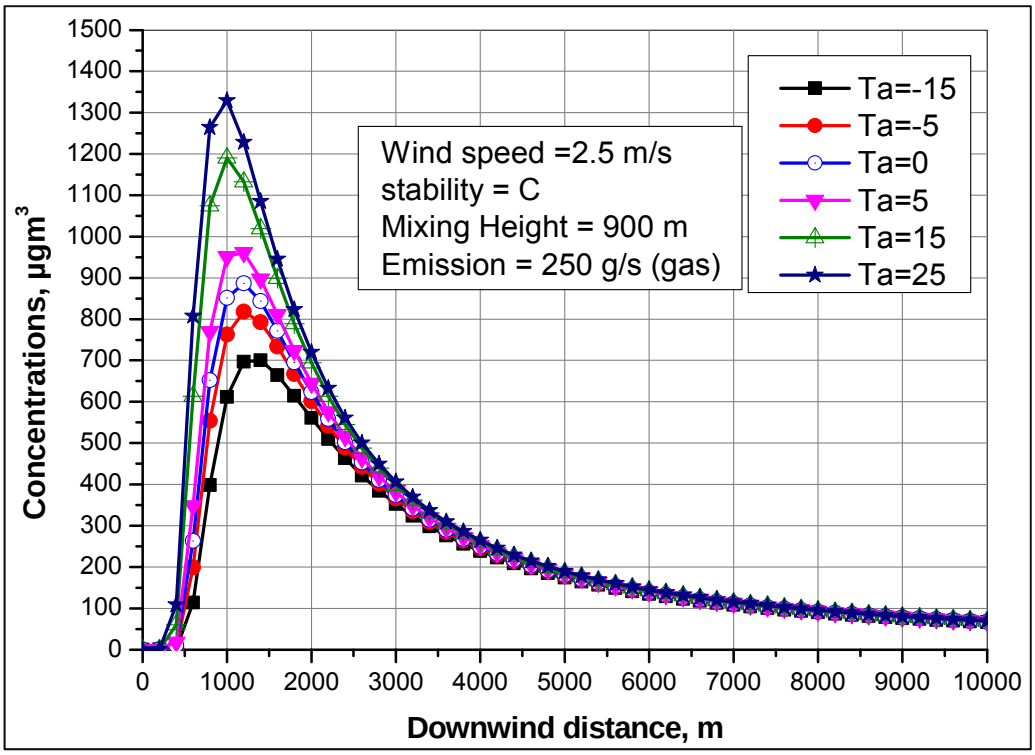

Figure (5-29) concentrations of gases estimated at different ambient temperatures

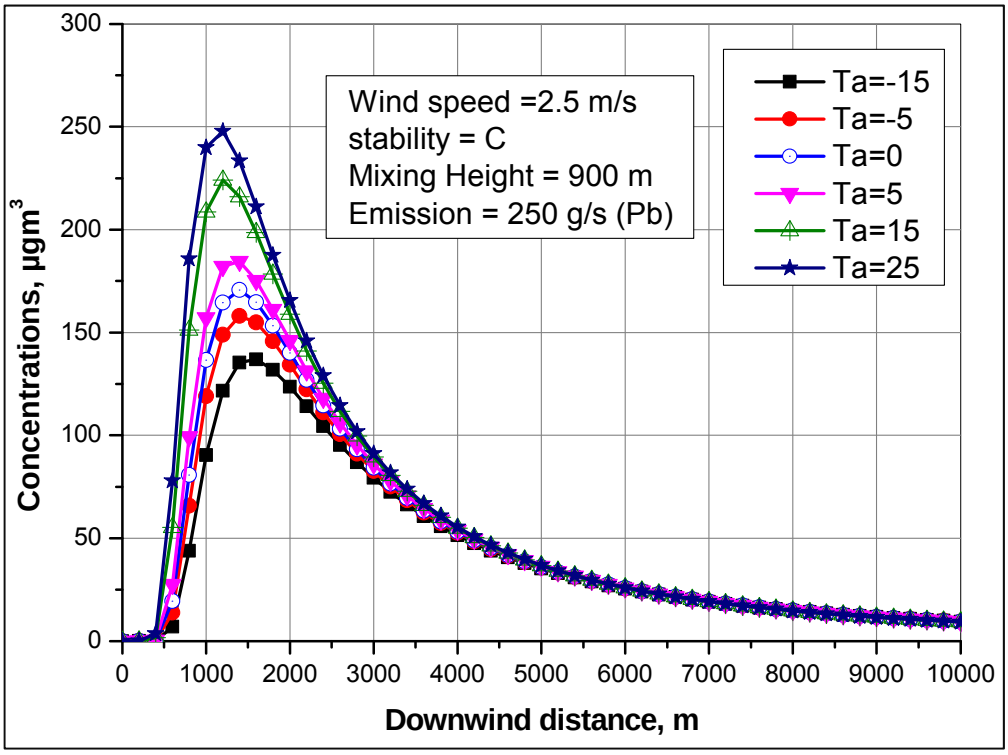

Figure (5-30) Particulate matters estimated at different ambient temperatures

Chapter (6) Conclusion

- The ancient mining and smelting activities in Goslar County have strong effects on the forest soil pollution by heavy metals. Good semivariogram structures of the studied soil heavy metals Pb, Zn, As, Hg, Cd, Sb and Cu are observed after transforming the raw data to lognormal or to Box-Cox transformation.

- The Kriging Standard Prediction Error can be used to decide where the best locations for new soil samples are. Selection of more soil samples in the areas which have few samples improves the spatial distribution of these anomalies.

- From the analysis of nugget variance, we can conclude that, reducing the measurement errors will reduce the nugget value; hence the spatial dependency of the studied variables will be increased which improves the predicted surfaces.

- The predicted concentrations of heavy metals on forest soil give a good estimation for low values of soil heavy metals and present underestimation for the high anomalies of these pollutants.

- Investigation of intensively polluted sites of forest soils is important to understand the amount of pollution in these locations. Merging these hotspot areas into the global map of the same variable is a technique to represent all the hotspot locations in one predicted map. Combining hotspot locations of Pb created by different geostatistical properties with its global map increased the accuracy of the estimated values in Lautenthal, Altenau and Clausthal-Zellerfeld cities.

- Geostatistical estimations were done by applied horizontal and inclined distances among samples. In this study, there was no clear difference between inclined and horizontal distances in geostatistical estimations. But the difference came from using log-transformation of the data rather than raw data sets based on horizontal or inclined distances.

- The results were useful for Goslar authority to describe the most contaminated areas and helped them in the decision making for remediation of some areas or exclude some activities from specific locations.

In this study a Dispersion Plume Model is developed based on Gaussian approach to estimate particulate matters emitted from a single point source. The generated model requires many meteorological variables as a feeding data such as mixing height, atmospheric stability, and deposition velocity of the particles. Therefore an Auxiliary Meteorological Model is created to compute the mentioned parameters. Some conclusions from this study are summarized as follow.

- The measured incoming solar radiation is more reliable than using altitude and cloud cover to detect the insolation strength of a day. The insolation strength is used to determine atmospheric stability during day-times.

- Results of Auxiliary Meteorological Model show that, the atmosphere is mostly stable conditions with frequency of 52 % for all times. Based on hourly stability pattern, nights of the winter have the most risk for pollution accumulation with 74.45 % stable atmospheric conditions. This risk came from the existing of inversion layer at very stable conditions which hinders the plume dispersion.

- High frequency of existing stable conditions is caused by the high frequency of wind speed that is less than 2 m/sec in the study area.

- The estimated mixing height during day times at summer and fall season is greater than the calculated values at winter and fall. While the nocturnal mixing height at winter and fall is more than that at summer and spring. The reason is that, solar radiation at summer and spring days are larger than the measured values at winter and fall season. During nighttime wind speed in winter and fall is greater.

- The estimated mixing heights at F stability are 80% less than 200 m at all the measured data, which refer to the existing of the inversion layer.

- The effect of stack tip downwash is observed at neutral atmospheric conditions. The physical stack height decreased on some conditions to 67 m instead of actual height of 70 m in the neutral winter season. For extreme unstable and extreme stable conditions there is no effect of the downwash on the stack height.

- For the estimated plume rise in the studied airshed, the momentum force is dominated when the ambient temperature is more than 15 ^{0}C unless buoyancy force is prevailing.

- The modeled contaminations in the summer traveled to long distances than the estimated values at winter. This result refers to the frequency of existing of atmospheric unstable conditions at the summer is greater than its occurrence in the winter.

- A significant frequency of wind direction towards North-West affected the estimated concentration at the fall. Also, the estimated concentrations at spring are affected by the direction of wind at this season.

- From the total Pb estimation by the dispersion modeling, Clausthal-Zellerfeld smelter contributed with an important part of soil pollution on the area around the smelter. Also the other smelters had a strong effect on the soil contamination within the investigated sites.

The generated models could be also used to cover other subjects. The Auxiliary Meteorological Model can be used in the aircraft industry to demonstrate the properties of atmosphere at the airports. Also it could be extended to use in the weather overcast. The generated Dispersion Plume Model is able to estimate the rate of emission gases from the industrial single sources. It can calculate the amount of SO_2, CO_2 among other gases in a specific volume at a specific period of time. The Dispersion Plume Model can be improved in the future to estimate the emissions from multiple sources.

References

Arya, S. P. S., 1981, “Parameterising the height of the stable atmospheric boundary layer”, Journal of Applied Metrology, Vol., 20, PP., 1192–1202.

Ashrafi, Kh. and Hoshyaripour, Gh. A. 2010 “A Model to Determine Atmospheric Stability and its Correlation with CO Concentration”, International Journal of Environmental Science and Engineering, Vol. 2, pp. 83-88

Atkinson DG, Bailey DT, Irwin JS, Touma JS., 1997, “Improvements to the EPA industrial source complex dispersion model”, Journal of Applied Meteorology, 1997, 36(8), PP., 1088-1095

Atteia,O., Dubois, J.-P., Webster, R., 1994, “Geostatistical Analysis of Soil Contamination in the Swiss Jura”, Environmental Pollution, Vol., 86, PP., 315-327

Awasthi, S., Khare, M., and Gargava, P., 2006, “General plume dispersion model (GPDM) for point source emission”, Environmental Modeling and Assessment, Vol. 11, PP., 267-276

Barratt, R., 2001, “Atmospheric Dispersion Modeling, An Introduction to Practical Applications” Sterling, Va., Earthscan Publications

Benkley C. W., and Schulman, L. L., 1979, “Estimating hourly mixing depths from historical meteorological data”, Journal of Applied Meteorology, Vol., 18, PP., 772-780

Beychok M.R, 2005, “Fundamentals of Stack Gas Dispersion” Newport Beach, CA, USA, Fourth Edition.

Brian E. Davies, B. E., 1987 “Consequences of environmental contamination by lead mining in Wales”, Hydrobiologia, Vol., 149, PP., 149-213-220

Bohling, G., 2005 “Introduction to Geostatistics and Variogram Analysis”, http://people.ku.edu/~gbohling/cpe940

Briggs, C. A., 1973, “Diffusion Estimation for Small Emissions. In Environ. Res. Lab., Air Resources Atmos. Turbulence and Diffusion laboratory, NOAA, Oak Ridge, Tennessee, Annual Rep., ATDL-106, USCOD-NOAA.

Briggs, G. A., 1969 “Optimum formulas for buoyant plume rise”, Philos. Trans. R. Soc. Lond., Vol., 265, PP., 197– 203

Burrough, 2001, “GIS and geostatistics: Essential partners for spatial analysis”, Environmental and Ecological Statistics, Vol., 8, PP., 361-377

Busch, W., 2007, “Basic-Geo-Information system”, Institute of Geotechnical Engineering and Mine Surveying, GIS Course

Chang, Y. H., Scrimshaw, M.D., Emmerson, R.H.C., and Lester, J.N., 1998 “Geostatistical analysis of sampling uncertainty at the Tollesbury Managed Retreat site in Backwater Estuary, Essex, UK: Kriging and Cokriging approach to minimize sampling density”, the Science of the Total Environment, Vol., 221, PP., 43-57

Coulter, R. L., 1979, “A comparison of Three Methods for Measuring Mixing-Layer Height”, Journal of Applied Meteorology, Vol. 18, pp. 1495-1499

David, M., 1977, “Geostatistical Ore Reserve Estimation” Elsevier Scientific Publ. Co., Amsterdam

Delobbe, L., Matthijsen, J., and Sauter, F. J., 2001, “Evaluation of Mixing Height representations in the EUROS model”, National Institute of Public Health and the Environment, RIVM report 711002 001.

Duffus, J. H., 2002, “Heavy Metals-A Meaningless Term (IUPAC Tenchnical Report)”, Pure and Applied Chemistry Vol., 74 No.5, pp., 793-807.

Einax, J., and Soldt, U., 1995, “Geostatistical Investigation of Polluted Soils”, Fresenius’ Journal of Analytical Chemistry, Vol., 351, PP., 48-53

EPA 1985, “Summary of Complex Terrain Model Evaluation”, Publication No., EPA-600/3-85-060, Office of Research & Development, Research Triangle Park, NC, (NTIS No., PB 85-236891)

EPA, 1977, “User’s Manual for Single Source (CRSTER) Model”, U.S. Environmental Protection Agency, EPA-450/2- 77-013, OAQPS Research, Triangle Park, NC, (NTIS PB 271360)

EPA, 1992, “User’s Guide for the Industrial Source Complex (ISC2) Dispersion Models, Volume I – User Instructions, II – Description of Model Algorithms, and III – Guide to Programmers, EPA450/ 492008a, 008b, and 008c, USEPA, RTP, NC.

EPA, 1994, “Development and testing of dry deposition algorithms (revised)”, EPA-454/R-94-015, U.S. Environmental Protection Agency

EPA, 1995, “User’s Guide for the Industrial Source Complex (ISC3) Dispersion Models”, EPA-450/B-95-003a, U.S. Environmental Protection Agency

Ermak, D. L., 1977, “An Analytical Model for Air Pollutant Transport and Deposition from a Point Source”, Atmospheric Environment, Vol. 11, PP., 231-237

Ernst, W. H. O., Knolle, F., Kratz, S., Schung, E., 2004, “Aspects of ecotoxicology of heavy metals in the Harz region – a guided excursion”, Landbauforschung Voelkenrode, Vol., 2(54), PP., 53-71

ESRI, 2001, “ArcGIS Geostatistical Analyst: Statistical Tools for data exploration, Modeling, and Advanced Surface Generation”, ESRI white papers, August, PP. 19

ESRI, 2001, “Using ArcGIS Geostatistical Analyst”, PP., 316

Fatogoma, O., and Robert, B. J., 2002, “A model to estimate mixing height and its effects on ozone modeling,” Atmospheric Environment, Vol. 36, pp. 3699-3708

Fraczek, W., and Byttnerowicz, A., 2007,”Automating the Use of Geostatistical Tools for Lake Tahoe Area study”, ArcUser, July-September, PP. 42-48.

Gäbler, H.-E., and Schneider, J., 2000, “Assessment of heavy-metal contamination of floodplain soils due to mining and mineral processing in the Harz Mountains, Germany” , Environmental Geology, Vol., 39(7), PP., 774-782

Gäbler, H.-E.; 1997; “Mobility of heavy metals as a function of pH of samples from an overbank sediment profile contaminated by mining activities”, Journal of Geochemical Exploration, Vol., 58, pp., 185- 194

Giovannoni, J. M., 1993, “Modeling of SO2, Pb and Cd Atmospheric Deposition over a one-year Period”, Atmos. Environ. Vol., 27A, PP., 1793-1808.

Golder, D., 1972, “Relations among Stability Parameters in the Surface Layer”, Boundary-Layer Meteorology, Vol., 3, PP., 47-58.

Goovaerts, P., 1999, “Geostatistics in soil science: state-of-the-art and perspectives” Geoderma, Vol., 89, pp., 1-45.

Goovaerts, P., 2001, “Geostatistical modelling of uncertainty in soil science”, Geoderma, Vol., 103, PP., 3-26

Hanna S. R., and Chang J.C., 1992, “Boundary-layer parameterizations for applied dispersion modeling over urban areas”, Boundary-Layer Meteorology, Vol., 58, PP., 229-259

Hanna S.R.; Chang J.C., 1993, “Hybrid plume dispersion model improvements and testing at three field sites”, Atmospheric Environment, Vol., 27 (A9), pp., 1491–1508

Hanna, S. R., Briggs, G. A., and Hosker, R. P., 1982, “Handbook on Atmospheric Dispersion, U. S. Department of Energy, Springfield, Virginia

Hanusch, K., 2005, “Die Unterharzer Metallhütten im 19. und 20.Jahrhundert - Chronik eines Wandels“, Weltkulturerbe Rammelsberg, Goslar

Hennighausen R., and Höfert,A., 2005 “Hinweise und Empfehlungen zur Bearbeitung und Nutzung schwermetallkontaminierter Gartenböden Anbau- und Verzehrempfehlungen“, Landkreis Goslar, Gesundheitsamt

Holtslag A. M., and van Ulden, A. P., 1983, “A simple scheme for daytime estimates of the surface fluxes from routine weather data”, J. Climate Applied Meteorology 22 (1983) 517–529

Hoppe, O., 1883, “Die Bergwerke, Aufbereitungs-Anstalten und Hütten sowie die technisch-wissenschaftlichen Anstalten, Wohlfahrts-Einrichtungen pp. im Ober- und Unter-Harz : dazu mehrere Tafeln ; nebst einem Anhang für geognost. Excursione “, Clausthal, Grosse

Horst, T. W., 1977, “A surface depletion model for deposition from a Gaussian plume”, Atmospheric Environment, Vol., 11, pp., 41-46.

Horst, T., W., 1984, “The Modification of Plume Models to Account for Dry Deposition”, Boundary-Layer Meteorology, Vol., 30, PP., 413-430

Ismael, A., Vaz, F., and Ferreira, E. C., 2009, “Air pollution control with semi-infinite programming”, Applied Mathematical Modeling, Vol. 33, No. 4, pp. 1957–1969

Järup, L, 2003, “Hazards of heavy metal contamination”, British Medical Bulletin, Vol., 68, PP., 167–182

Jonušaitė, A., Štrimaitytė, V., and Denafas, G., 2004 “Heavy Metals Mobilization from Ash of Biofuel and Burnable Waste” Environmental research, engineering and management, Vol., 3 (29), PP., 29-36

Journel A. G., and Huijbregts C. J., 1978, “Mining Geostatistics”, Academic Press

Kaufhold, K. H., 1992, “Bergbau und Hüttenwesen im und am Harz“ Hahnsche Buchhandlung, Hannover

Khan, S.M., and Simpson, R.W., 1997, “Modelling mixing height from routinely measured surface and upper air meteorological data”, Environmental Modeling and Assessment, Vol., 2, PP., 191–200

Kiikkilä, O. 2003 “Heavy-metal pollution and remediation of forest soil around the Harjavalta Cu-Ni smelter, in SW Finland”, Silva Fennica, Vol., 37(3), PP 399–415

Korre, A., Durucan, S., and Koutroumani, A., 2002, “Quantitative-spatial assessment of the risks associated with high Pb loads in soils around Lavrio, Greece” Applied Geochemistry, Vol., 17, PP., 1029–1045

Krivoruchko, K., and Gotway, C. A., 2002 “Expanding the “S” in GIS: Incorporating Spatial Statistics in GIS”, presented at the CSISS Specialist Meeting on Spatial Data Analysis Software Tools in Santa Barbara in May 2002.

Kumar, A., Maroju, S., and Bhat, B., 2007, “Application of ArcGIS Geostatistical Analyst for Interpolating Environmental Data from Observations”, Environmental Progress, Vol., 26, No.3, PP., 220-225

Kumar, R., Srivastava, S. S., Kumar, K. K., 2008, “Modeling dry deposition of S and N compounds to vegetation”, Indian Journal of Radio and Space Physics, Vol., 37, PP., 272-278.

Large D., Walcher, E., 1999, “The Rammelsberg massive sulphide Cu–Zn–Pb–Ba-deposit, Germany: an example of sediment-hosted, massive sulphide mineralization”, Mineralium Deposita, Vol., 34, PP., 522–538

Lena F., and Desiato F., 1999, “Inter-comparison of nocturnal mixing height estimate methods for urban air pollution modeling”, Atmospheric Environment, Vol., 33, pp., 2385-2394

Lide, D.R. (ed.), 1992, “Handbook of chemistry and physics”, CRC Press, Cleveland, OH

Liu, X., Wu, J., and Xu, J., 2006 “Characterizing the risk assessment of heavy metals and sampling uncertainty analysis in paddy field by Geostatistics and GIS”, Environmental pollution, Vol., 141, PP., 257-264.

Longley, P.A., Goodchild, M.F., Maguire, D.J. and Rhind, D.W., 2005 “Geographic Information Systems and Science” Chichester, England, Wiley, 2nd edition

Lott R.A., 1984, “Case Study of Plume Dispersion over Elevated Terrain”, Atmospheric Environment, Vol., 18(1), PP., 125-134

Lott R.A., 1986, “Model performance-plume dispersion over elevated terrain”, Atmospheric Environment, Vol., 20(8), PP., 1547-1554

Markus, J., and McBratney, A. B., 2001, “A review of the contamination of soil with lead II-Spatial distribution and risk assessment of soil lead”, Environment International, Vol., 27, PP., 399–411

Matschullat, J., Ellminger, F., Agdemir, N., Cramer, S., Liessmann, W., and Niehoff, N., 1997, “Overbank sediment profiles-evidence of early mining and smelting activities in the Harz Mountains, Germany”, Applied Geochemistry, Vol., 12, PP., 105–114

McGrath, D., Zhangb, C., and Cartona, O. T., 2004 “Geostatistical Analyses and Hazard Assessment on Soil Lead in Silvermines Area, Ireland”, Environmental Pollution, Vol., 127, PP., 239–248

Mertz, D. F., Lippolt, H. J., and Schnorrer-Koehler, G., 1989 ”Early Cretaceous mineralizing activity in the St. Andreasberg ore district (Southwest Harz, Federal Republic of Germany)” Mineralium Deposita, Vol., 24, PP., 9-13

Meshalkina, Yu. L., 2007, “A Brief Review of Geostatistical Methods Applied in Modern Soil Science“, Moscow University Soil Science Bulletin, Vol. 62, No. 2, pp. 93–95

Monna, F., Hamer, K., Leveque, J., and Sauer, M., 2000, “Pb isotopes as a reliable marker of early mining and smelting in the Northern Harz province (Lower Saxony, Germany)” Journal of Geochemical Exploration, Vol., 68, PP., 201–210

Muchez, P., and Stassen, P., 2006 “Multiple origin of the ‘Kniest feeder zone’ of the stratiform Zn–Pb–Cu ore deposit of Rammelsberg, Germany”, Mineralium Deposita, Vol., 41, PP., 46–51

Navas, A., and Machin, J., 2002, “Spatial distribution of heavy metals and arsenic in soils of Aragon (northeast Spain): controlling factors and environmental implications”, Applied Geochemistry, Vol., 17, PP., 961–973

Peucker, H., 1958, Rauchschäden der Bleihütte Clausthal ihre Entstehung und Bekämpfung, Diplomarbeit, Institute für Landesflege, Landschafts und Gartengestaltung der Technischen Hochschule Hannover, Niedersachsenes Bergarchiv Hann. 184, preußisches Oberbergamt Acc., 14 Nr., 1161

Rabeiy, R., Busch, W., Knospe, St., Schmotz, W., 2010, “Geostatistical Investigation of Forest Soil Contamination from Mining and Smelting Activities in Goslar District (Middle Germany)”, presented at 5th Annual International Symposium on Environment, 20-23 May 2010, Athens, Greece

Rendu, J-M., 1978, “An Introduction to Geostatistical Methods of Mineral Evaluation” Monograph of the South African Inst. Min. Metall

Sabienë, N., Brazauskienë, D., and Rimmer, D., 2004, “Determination of heavy metal mobile forms by different extraction methods”, EKOLOGIJA, Vol., 1, PP., 36–41

Schnelle, K. B. and Dey, P. R., 2000, “Atmospheric Dispersion Modeling Compliance Guide”, McGraw-Hill

Schroeder, J.and Reuss, C., 1883, “Die Beschädigung der Vegetation durch Rauch und die Oberharzer Hüttenrauchschäden“, P. Parey, Berlin.

Schulze, O., Roth, R., and Pieper, O., 1994, “Probable maximum precipitation in Upper Harz”, Flow Regimes from International Experimental and Network Data (Proceedings of the Braunschweig, Conference, October 1993). IAHS Publ., No., 221. pp., 315-321

Segers-Glocke, C., and Witthöft, H., (editors) 2000, “Aspects of mining and smelting in Upper Harz Moutains (up 13th / 14th Century)- in the Early Times of a Developing European Culture and Economy”, Scripta Mercature Verlag, St. Katharinen

Sehmel, G. A., 1980 “Particle and gas dry deposition: a review”, Atmospheric Environment, Vol., 14, PP., 983-1011

Shi, J., Wang, H., Xu, J., Wu, J., Liu, X., Zhu, H., and Yu, C., 2007,”Spatial distribution of heavy metals in soils: a case study of Changxing, China”, Environmental Geology, Vol., 52, PP., 1–10

Steiger, B., Webster, R., Schulin, R., and Lehmann, R., 1996, “Mapping heavy metals in polluted soil by disjunctive kriging”, Environ. Pollut., Vol., 94, PP:, 205-215

van Alphen, M., 1999, “Atmospheric heavy metal deposition plumes adjacent to a primary lead-zinc smelter”, The Science of the Total Environment, Vol. 236, PP., 119-134

Venkatram, A., 1978, “Estimating convective velocity scale for diffusion application”, Boundary-layer Meteorology, Vol., 15, PP., 447–452

Venkatram, A., 1986, ‘An Examination of Methods to Estimate the Height of the Coastal Internal Boundary Layer’, Boundary-Layer Meteorology, Vol., 36, PP., 149-156

Vesovic,V., Auziere,A., Calviac, G., Dauriat, G., 2001, “ Modelling of the dispersion and deposition of coarse particulate matter under neutral atmospheric conditions”, Atmospheric Environment, Vol., 35, No., 1, PP., 99-105

Voldner E. C., Barrie L. A. and Sirois A., 1986, “A literature review of dry deposition of oxides of sulphur and nitrogen with emphasis on long range transport modelling in north America”, Atmospheric Environment, Vol., 20, PP., 2101-2123

Walcek, C. J., Brost, R. A., Chang, J. S. and Wesely, M. L., 1986, "SO, sulfate and HNO_3 deposition velocities computed using regional landuse and meteorological data", Atmospheric Environment, Vol., 20, PP., 949-964

Webster R., and Oliver M., 2007, "Geostatistics for Environmental Scientists", John Wiley & Sons, Second Edition

Weil J.C., and Brower, R.P. 1983, "Estimating convective boundary layer parameters for diffusion applications", Report PPSP-MP-48, Environmental Centre, Martin Marietta Corporation for Maryland Department of Natural Resources, Annapolis, MD

Williamson, B. J., Udachin, V., Purvis, O. W., Spiro, B. , Cressey, G. , and Jones, G. C., 2004 "Characterization of Airborne particulate pollution in the Cu Smelter and Former Mining Town of Karabash, South Ural Mountains of Russia", Environmental Monitoring and Assessment, Vol., 98, PP., 235–259

www.landkreis-goslar.de

www.lef.org/

www.weblakes.com/

Xu, Y., and Carmichael, G. R., 1998, "Modeling the Dry Deposition Velocity of Sulfur Dioxide and Sulfate in Asia", Journal of applied Meteorology, Vol., 37, PP., 1084-1099

Yu, T.-W., 1978,"Determining Height of Nocturnal Boundary Layer", journal of applied Meteorology, Vol., 17, PP., 28-33

Zhang, C., and Selinus, O., 1997 "Spatial Analyses for Copper, Lead and Zinc Contents in Sediments of the Yangtze River Basin", The Science of the Total Environment, Vol., 204, PP., 251-262

Appendix A: *Auxiliary Meteorological Model*

```
clc
clear
count=1;
Rohp=11.36;          % Pb particle density
z=10;                % considered height
zo=0.9;              % Roughness length (=wind reference height)
d=5*zo;              % displacement length
v=0.15;              % air viscosity (cm^2/s)

% Data for Dry Deposition
k=0.4;               % Von-Karman constant
x2=6.5*10^(-6);      % Constant
ad1=1.257; ad2=0.4;  ad3=0.55*10^(-4);  cg2=1*10^-8;
g= 9.81;             % Acceleration velocity (m/s^2)
Miu=1.83*10^-4;      % Miu- the absolute air viscosity (g/cm.s)
dp=5;                % particles diameter (micro m)

% data for sensible heat flux
as1= 990; as2=-30;  bs1=-0.75;  bs2=3.4;        % empirical constant
cs1= 5.31*10^-13; cs2=60; cs3=0.12;             % empirical constant
poltz=5.67*10^-8;    % Stefan-Poltzmann constant
r=0.17;              % Albedo describes the effects of the surface on the net incoming solar
G=0.1;               % the ratio between soil heat flux and net radiation
as=0.85; Bs=20;      % empirical constant
S= 1.366;            % is the solar constant (1367.7 W/m²)
A= 0.25;             % is a function of ground cover, and it varies from 0.25 for a
                     crop canopy to 0.55 for a dry surface
cp=1005.7;           % air specific capacity under constant pressure
roha=1.245;          % air density

%% Read Meteorological data
Mdata=xlsread('Spring_3_','data');  %Read Meteorological data
hou=Mdata(:,4); Wdir=Mdata(:,5); Wspeed=Mdata(:,6); Temp=Mdata(:,8); pressure=Mdata(:,9);
humidity=Mdata(:,10); solar=Mdata(:,11);
sunr=Mdata(:,12); suns=Mdata(:,13); solMax=Mdata(:,14);
Mn=size(Wdir,1),          %Mn-Number of Meteorological data
for j=1:Mn;
 hour=hou(j,:); Wd=Wdir(j,:); uf=Wspeed(j,:); Ta=Temp(j,:)+273; P=pressure(j,:); Hu=humidity(j,:);
Ks=solar(j,:);
  sunrise=sunr(j,:); sunset=suns(j,:); ksMax=solMax(j,:);
   if uf<0.0001; uf=0.01; end;
  %Determination of the atmospheric stability
   % a- day with strong solar
   if hour>sunrise+1 && hour<sunset-1;
```

```
   if Ks>=500, N=1/8; if uf <= 3; stab='A'; end, if 5>uf&&uf>3, stab='B'; end, if uf >= 5, stab='C';  end,
end,
   % b day-Moderate
  if Ks<500&&Ks>=300, N=3/8; if uf <= 2, stab='A'; end, if 5>uf&&uf>2, stab='B'; end,if 5>uf&&uf>6,
stab='C'; end, if uf >= 6, stab='D';  end; end;
   % c day-slight or weak
   if Ks<300&&Ks>200, N=5/8; if uf <= 3, stab='B'; end, if 5>uf&&uf>3, stab='C';end, if uf >= 5,
stab='D'; end; end;
   if Ks<=200, N=7/8; stab='D'; end
   % stability in the night hours
   else
   if Ks>115; N=7/8; stab='D';else if uf<=2; N=3/8; stab='F';end; if 4>uf&&uf>2, N= 5/8; stab='E';
end,if uf>4; N= 7/8; stab='D';end;end;
   end

%% Estimation of sensible heat, friction velocity, Mixing Height and deposition velocity
gama=0.003350414+0.046613554*Ta+-0.000151974*Ta^2;
 Q=((1-r)*Ks+cs1* Ta^6-poltz*Ta^4+cs2*N)/(1+cs3);              % the net radiation.
Hs= (((1-as)+(gama))/(1+gama))*(Q-G*Q)-Bs;                    % is the sensible heat flux
 QMax=((1-r)*ksMax+cs1*Ta^6-poltz*Ta^4+cs2*N)/(1+cs3);        % the net radiation.
HsMax= (((1-as)+(gama))/(1+gama))*(QMax-G*QMax)-Bs;           % is the sensible heat flux

KHs=Hs/(roha*cp);
 HMax=HsMax/(roha*cp);                 % kinematic heat flux in (m K/s)
 Qm=A*Ks/(roha*cp);                    % maximum heat surface flux (m K /s)
we= 4.74*Qm^0.5;                       % Convective velocity scale
if HMax<0, we=0; end;
 w= 2*pi/(24*60*60);                   % is the rate of earth rotation m/s,
beata=51.754*pi/180;                   % latitude of the study area
cf=2*w*sin(beata);                     % cf is the Coriolis factor
 f=log((z-d)/zo);
f1=log(zo/(z-d));
f2=zo/(z-d);
theata1=0.09*(1-0.5*N^2);
theata2=(0.4*Ta*uf^2)/(18.8*g*z*f);
 if theata1<theata2, theata=theata1; else theata=theata2; end
 stability= stab;
switch stability,
   case {'A','B','C'}
     if f2<=0.01, d1=0.128+0.005*f1; else d1=0.107; end
        d2=1.95+32.6*(f2^0.45);
        d3=(Hs/(roha*cp))*(0.4*g*(z-d)/Ta)*((f/(0.4*uf))^3);
      U_=(0.4*uf/f)*(1+d1*log(1+d2*d3));          % Friction velocity (m/s)
      L=-(roha*cp*Ta*U_^3)/(0.4*g*Hs);            % Monion-Pbukhv length (m)
      Hm=-0.4*L*((we/U_)^3);                      % Mixing Height (m)
        psiH =2*(log((1+sqrt(1-16*z/L))/2));
        Ra=((k*U_*100)^-1)*(log(z/zo)-psiH);                  % Ra-Aerodynamic resistance
        Scf=1+(2*x2*(ad1+ad2*exp(-ad3*dp/x2)))/(dp*10^(-4));  % Scf-correction factor
```

```
        Bd=8.09*(10^-10)*(Ta*Scf/dp);                          % Bd-Brownin diffusivity (cm^2/s)
        Sc=v/Bd;                                               % (Sc) Schmidt number
        vt=Scf*(Rohp*100*g*(dp^2)*cg2)/(18*Miu);               % settling(terminal) velocity (cm/s)
        St=(vt*(100*U_)^2)/(g*100*v);                          % Stocks number
        Rd= ((U_*100)^-1)*((Sc^(-2/3)+10^(-3/St))^-1);         % Rd-deposition layer resistance
        Vd= (((Ra+Rd+Ra*Rd*vt)^-1)+vt);                        % Vd-deposition velocity , (cm/s)
    case 'D'
       U_=(0.4*uf/f);
       L=-(roha*cp*Ta*U_^3)/(0.4*g*Hs);
       Hm=0.089*U_/cf+85.1;
        Ra=((k*U_*100)^-1)*(log(z/zo));                        % Ra-Aerodynamic resistance
        Scf=1+(2*x2*(ad1+ad2*exp(-ad3*dp/x2)))/(dp*10^(-4));   % Scf-correction factor
        Bd=8.09*(10^-10)*(Ta*Scf/dp);                          % Bd-Brownin diffusivity (cm^2/s)
        Sc=v/Bd;                                               % (Sc) Schmidt number
        vt=Scf*(Rohp*100*g*(dp^2)*cg2)/(18*Miu);               % settling(terminal) velocity (cm/s)
        St=(vt*(100*U_)^2)/(g*100*v);                          % Stock's number
        Rd= ((U_*100)^-1)*((Sc^(-2/3)+10^(-3/St))^-1);         % Rd-deposition layer resistance
        Vd=(((Ra+Rd+Ra*Rd*vt)^-1)+vt);                         % Vd-deposition velocity , (cm/s)
    case {'E','F'}
       t1=4*((4.7*g*z*theata*f)/(0.4*Ta*uf^2));
       t2=1-t1;
       if t2<0, t2=1e-25;end;
       U_=(0.2*uf/f)*(1+t2^0.5);
       L=-(roha*cp*Ta*U_^3)/(0.4*g*Hs);
       Hm=113+0.34*((L*U_/cf)^0.5);
       psiH=5*(z/L);
        Ra=((k*U_*100)^-1)*(log(z/zo)+psiH);                   % Ra-Aerodynamic resistance (Ra)
        Scf=1+(2*x2*(ad1+ad2*exp(-ad3*dp/x2)))/(dp*10^(-4));   % Scf-correction factor
        Bd=8.09*(10^-10)*(Ta*Scf/dp);                          % Bd-Brownin diffusivity (cm^2/s)
        Sc=v/Bd;                                               % (Sc) Schmidt number
        vt=Scf*(Rohp*100*g*(dp^2)*cg2)/(18*Miu);               % settling(terminal) velocity (cm/s)
        St=(vt*(100*U_)^2)/(g*100*v);                          % Stock's number
        Rd= ((U_*100)^-1)*((Sc^(-2/3)+10^(-3/St))^-1);         % Rd-deposition layer resistance
        Vd=(((Ra+Rd+Ra*Rd*vt)^-1)+vt);                         % Vd-deposition velocity , (cm/s)
end
MixH(count,:)=Hm;Mo_Ob(count,:)=L; DeposVel(count,:)=Vd; stabilityCase(count,:)=stab;
fricVel(count,:)=U_; conv(count,:)=we; conv_(count,:)=we;
sett_veloc(count,:)=vt/100;
Res(count,:)=[MixH(count,:);DeposVel(count,:);Mo_Ob(count,:);fricVel(count,:);conv_(count,:);sett_ve
loc(count,:)];
count=count+1;
end
```

Appendix B: *Dispersion Plume Model*

```
clc
clear
close all
ind=1;
D=2;              %diameter of stack
vs=9.95;          % stack exist velocity
Ts=32+273;        % emission temperature
hf=10;            % reference height
z=10;             % considered height
zo=0.9;           % Roughness length (=wind reference height)
d=5*zo;           % displacement length
g=9.81;
vt=0.133656;              % settling velocity ; m/s
hs=70;                    % physical stack height
Terrmodel='5';            % models used to correct H according to the Terrain effect.

%% Coordinates for points
xs=3589800; ys=5741200; zs=511.05;  % source coordinates
m=xlsread('data', 'data','a1:c1');          %Read receptor coordinates from excel file
xo=m(:,1); yo=m(:,2); zo=m(:,3);
nr=size(xo,1),                              %number of receptors
 for i=1:nr;
xr=xo(i,:);
yr=yo(i,:);
zr=zo(i,:);
ht= zr-zs;

% read Data
[Mdata,text]=xlsread('Model_data','Winter','a1:i13008');  %Read Meteorological data from excel sheet
[file, text1]= xlsread('Model_data','Empty2','e1:e13008'); % read stability data from excel quantity =
Mdata(:,1); hou=Mdata(:,2); Wspeed=Mdata(:,3); Wdir=Mdata(:,4); Temp=Mdata(:,5);
MexH=Mdata(:,7); DiposVel=Mdata(:,8);
pressure=Mdata(:,9);
Mn=size(Wdir,1),                    %Mn-Number of Meteorological data
for j=1:Mn;
Q= quantity (j,:); hour=hou(j,:);uf=Wspeed(j,:); wd1=Wdir(j,:);  Ta=Temp(j,:)+273;
Hm=MexH(j,:); Vd=DiposVel(j,:); stab=char(text1(j,:)); p=pressure(j,:);

wd=wd1*pi/180;                      % wd angle of wind direction from the north
x=(xr-xs)*sin(wd)+(yr-ys)*cos(wd);
y=(yr-ys)*sin(wd)-(xr-xs)*cos(wd);
if x<0, x=0;y=0; end
dx=x*sin(wd)-y*cos(wd);
dy=x*cos(wd)+y*sin(wd);
X=dx+xs; Y=dy+ys;
x_diff=xr-X; y_diff=yr-Y;

%% Wind correction to the stack height at different Stabilities
stability=stab;
    switch stability
        case 'A';  us=uf*(hs/hf)^0.07;
        case 'B';  us=uf*(hs/hf)^0.075;
        case 'C';  us=uf*(hs/hf)^0.10;
        case 'D';  us=uf*(hs/hf)^0.15;
        case 'E';  us=uf*(hs/hf)^0.35;
        case 'F',  us=uf*(hs/hf)^0.55;
    end
      if vs<1.5*us, hs1=hs+2*D*((vs/us)-1.5); else hs1=hs; end  % stack tip downwash
```

```
 %% Plume Rise Model
F=g*vs*D^2*(Ts-Ta)/(4*Ts);            % Buoyancy flux parameter
Fm=vs^2*D^2*Ta/(4*Ts);                % Momentum flux parameter
dt=(Ts-Ta);

if F>= 55, xf=119*F.^0.4; dtc = 0.00575*Ts*vs^(2/3)/D^(1/3);  else
           xf=49*F.^0.625;   dtc = 0.0297*Ts*vs^(1/3)/D^(2/3);
end

stability =stab;
  switch stability,

    case {'A','B','C','D'},

       if dt<dtc,  hr = 3*D*vs/us; else

         if F>=55; if x<xf; hr=1.6*F^(1/3)*x^(2/3)*us^(-1); else hr=38.7*f^0.6*us^-1; end;
         else

        if x<xf; hr=1.6*F^(1/3)*x^(2/3)*us^(-1); else  hr=21.4*F^(0.75)*us^(-1); end
         end
       end

    case 'E', s= 0.015*(g/Ta); tst=1.84*us*s^-0.5;  dtc= 0.019582*Ts*vs*s^0.5;
       if dt<dtc, hr= 1.5*(Fm/us)^(1/3)*s^(-1/6); else

       if tst>= xf,
          if x< xf; hr=1.6*F^(1/3)*x^(2/3)*us^(-1); else
             if F>=55; hr=38.7*F^(0.6)*us^(-1); else hr=21.4*(F^0.75)*us^(-1);end
       end;

       else if x<tst; hr=1.6*F^(1/3)*x^(2/3)*us^(-1); else hr=2.4*(F/us*s)^(1/3); end
       end;
       end

    case 'F', s= 0.025*(g/Ta); tst =1.84*us*s^-0.5; dtc= 0.019582*Ts*vs*s^0.5;

       if dt<dtc, hr= 1.5*(Fm/us)^(1/3)*s^(-1/6); else

       if tst>= xf, if x< xf; hr=1.6*F^(1/3)*x^(2/3)*us^(-1); else hr=21.4*(F^0.75)*us^(-1);end

       else if x<tst; hr=1.6*F^(1/3)*x^(2/3)*us^(-1); else hr=2.4*(F/us*s)^(1/3); end
       end;
       end;
  end
  He=hs1+hr;

%% Adjusted Wind speed at plume height
 stability=stab;
    switch stability
         case 'A';  us=uf*(He/hf)^0.07;
         case 'B';  us=uf*(He/hf)^0.075;
         case 'C';  us=uf*(He/hf)^0.10;
         case 'D';  us=uf*(He/hf)^0.15;
         case 'E';  us=uf*(He/hf)^0.35;
         case 'F',  us=uf*(He/hf)^0.55;
    end
```

```
%% Terrain Effect
stability = stab;
switch stability,
case 'A'
    R=0.8; C=0.4; Ft=0.5;
    model = Terrmodel;
  switch model,
      case '1'
          if He>ht, H=He-(ht/(1-R));          else H=He*R;     end
      case '2'
         if He>ht, H=He*((1-(ht/He))*(1-R));     else H=He*R;     end
      case '3'
          if He>ht, H=He*(1-(ht/He)*(1-R/(1+ R*(He/ht-1))));    else H=He*R;     end
      case '4'
          if He>ht, H= He-ht-(ht/He)^3*(1-C);  else H=He*(1-C); end
      case '5'
          H=He-(1-Ft)*ht;
      case '6'
          H=He+ht;
  end
case 'B'
    R=0.7; C=0.4; Ft=0.5;
    model = Terrmodel;
  switch model,
      case '1'
          if He>ht, H=He-(ht/(1-R));          else H=He*R;     end
      case '2'
         if He>ht, H=He*((1-(ht/He))*(1-R));     else H=He*R;     end
      case '3'
          if He>ht, H=He*(1-(ht/He)*(1-R/(1+ R*(He/ht-1))));    else H=He*R;     end
      case '4'
          if He>ht, H= He-ht-(ht/He)^3*(1-C);  else H=He*(1-C); end
      case '5'
          H=He-(1-Ft)*ht;
      case '6'
          H=He+ht;
  end
case 'C'
    R=0.6; C=0.4; Ft=0.5;
    model = Terrmodel;
  switch model,
      case '1'
          if He>ht, H=He-(ht/(1-R));          else H=He*R;     end
      case '2'
         if He>ht, H=He*((1-(ht/He))*(1-R));     else H=He*R;     end
      case '3'
          if He>ht, H=He*(1-(ht/He)*(1-R/(1+ R*(He/ht-1))));    else H=He*R;     end
      case '4'
          if He>ht, H= He-ht-(ht/He)^3*(1-C);  else H=He*(1-C); end
      case '5'
          H=He-(1-Ft)*ht;
      case '6'
          H=He+ht;
  end
case 'D'
    R=0.5; C=0.4; Ft=0.5;
    model = Terrmodel;
  switch model,
      case '1'
          if He>ht, H=He-(ht/(1-R));          else H=He*R;     end
      case '2'
         if He>ht, H=He*((1-(ht/He))*(1-R));     else H=He*R;     end
```

```
      case '3'
         if He>ht, H=He*(1-(ht/He)*(1-R/(1+ R*(He/ht-1))));    else H=He*R;     end
      case '4'
         if He>ht, H= He-ht-(ht/He)^3*(1-C);  else H=He*(1-C); end
      case '5'
         H=He-(1-Ft)*ht;
      case '6'
         H=He+ht;
   end

case 'E'
    R=0.4; C=0.4; Ft=0.25;
   model = Terrmodel;
   switch model,
       case '1'
         if He>ht, H=He-(ht/(1-R));          else H=He*R;     end
      case '2'
        if He>ht, H=He*((1-(ht/He))*(1-R));    else H=He*R;     end
      case '3'
         if He>ht, H=He*(1-(ht/He)*(1-R/(1+ R*(He/ht-1))));    else H=He*R;     end
      case '4'
         if He>ht, H= He-ht-(ht/He)^3*(1-C);  else H=He*(1-C); end
      case '5'
         H=He-(1-Ft)*ht;
      case '6'
         H=He+ht;
   end

case 'F'
    R=0.3; C=0.7; Ft=0.25;
   model = Terrmodel;
    switch model,
       case '1'
         if He>ht, H=He-(ht/(1-R));          else H=He*R;     end
      case '2'
        if He>ht, H=He*((1-(ht/He))*(1-R));    else H=He*R;     end
      case '3'
         if He>ht, H=He*(1-(ht/He)*(1-R/(1+ R*(He/ht-1))));    else H=He*R;     end
      case '4'
         if He>ht, H= He-ht-(ht/He)^3*(1-C);  else H=He*(1-C); end
      case '5'
         H=He-(1-Ft)*ht;
      case '6'
         H=He+ht;
    end
end

%% Standard Deviation in vertical and horizontal distances at each atmospheric stability
  stability = stab;
    switch stability
          case 'A'
            a= 0.22; b= 0.0001; sigma_y=a*x*(1+b*x).^(-0.5); sigma_z=0.20*x;
          case 'B'
             a= 0.16; b= 0.0001; sigma_y=a*x*(1+b*x).^(-0.5); sigma_z=0.12*x;
          case 'C'
             a= 0.11; b= 0.0001; sigma_y=a*x*(1+b*x).^(-0.5); sigma_z=0.08*x*((1+0.0002*x)^-0.5);
          case 'D'
             a= 0.08; b= 0.0001; sigma_y=a*x*(1+b*x).^(-0.5); sigma_z=0.06*x*((1+0.0015*x)^-0.5);
          case 'E'
             a= 0.06; b= 0.0001; sigma_y=a*x*(1+b*x).^(-0.5); sigma_z=0.03*x*((1+0.0003*x)^-1);
          case 'F'
            a= 0.04; b= 0.0001; sigma_y=a*x*(1+b*x).^(-0.5); sigma_z=0.022*x*((1+0.0003*x)^-1);
```

```
    end

%% Concentration at each point
 V=Vd-0.5*vt;
ita=H/(sigma_z*sqrt(2))+sqrt(2)*(V*x/(us*sigma_z));

Ver0=(exp(-0.5*(H/sigma_z )^2));
Ver1=(exp(-0.5*((2*Hm-H)/sigma_z )^2)+exp(-0.5*((2*Hm+H)/sigma_z )^2));
Ver2=(exp(-0.5*((4*Hm-H)/sigma_z )^2)+exp(-0.5*((4*Hm+H)/sigma_z )^2));

VF=Ver0+Ver1+Ver2;              %vertical term without profile modification

    part_1=((10^3*Q/(us*pi*sigma_y*sigma_z))*exp(-0.5*(y/sigma_y)^2));

    DF1= exp((-vt*H*x/(us*sigma_z^2))-(vt^2*x^2/(2*us^2*sigma_z^2)));
    DF2=1-sqrt(2*pi)*(V*x/(us*sigma_z))*exp(ita^2)*erfc(ita);

    DF=DF1*DF2;

    Con=part_1*VF*DF;           % in case of particulate matter
    %Con=part_1*VF;             % in case of gases

 if x<2 , Con=0;  end

Res(ind,:) =[xr Con];
stab_Index(ind,:)=stab;
Con_1=Con+Con;
plot(x,Con,'--bs'); grid on; hold on ;

ind=ind+1;
end
end
```